January 2016

Three Dimensional Unsteady Flow and Active Morphing Effect in Flapping Wings

Yun Liu
Purdue University

Graduate School Form
30 Updated 12/26/2015

PURDUE UNIVERSITY
GRADUATE SCHOOL
Thesis/Dissertation Acceptance

This is to certify that the thesis/dissertation prepared

By Yun Liu

Entitled
Three Dimensional Unsteady Flow and Active Morphing Effect in Flapping Wings

For the degree of Doctor of Philosophy

Is approved by the final examining committee:

Xinyan Deng
Chair

Pavlos P. Vlachos

Steven T. Wereley

Alina Alexeenko

To the best of my knowledge and as understood by the student in the Thesis/Dissertation Agreement, Publication Delay, and Certification Disclaimer (Graduate School Form 32), this thesis/dissertation adheres to the provisions of Purdue University's "Policy of Integrity in Research" and the use of copyright material.

Approved by Major Professor(s): Xinyang Deng

Approved by: Jay P. Gore 7/27/2016

Head of the Departmental Graduate Program Date

THREE DIMENSIONAL UNSTEADY FLOW

AND

ACTIVE MORPHING EFFECT

IN

FLAPPING WINGS

A Dissertation

Submitted to the Faculty

of

Purdue University

by

Yun Liu

In Partial Fulfillment of the

Requirements for the Degree

of

Doctor of Philosophy

August 2016

Purdue University

West Lafayette, Indiana

ACKNOWLEDGMENTS

First, I want to express my deep gratitude to Dr. Xinyan Deng for her constant and encouraging support and guidance which were essential to my research through all these five years.

Especially, I want to thank Dr. Bo Cheng, a close colleague and friend, for his critical input and comments on Chapters 2, 3, and 4. During the writing of Chapter 5, I was very much benefited from the comments and discussions with Mr Jesse Roll who was also very kind in helping me on experimental setups in different projects. I further want to thank Dr Haibo Dong from University of Virginia and Dr Sanjay.P Sane from National Center for Biological Sciences of India for their kind input and comments.

Lastly, I would like to thank my grandfather Shuren Liu for his inspiring words and spirits that motivated me to accomplish every goal during this journey of searching and exploring.

TABLE OF CONTENTS

LIST OF TABLES

LIST OF FIGURES

Figure Page

Figure Page

ABBREVIATIONS

AoA	Angle of Attack
LEV	Leading edge vortex
TEV	Trailing edge vortex
TV	Tip vortex
RV	Root vortex
SV	Starting vortex
ϕ	Stroke angle
ψ	Rotational angel
ω	vorticity
δ	flexion angle
Γ	Circlation
t_{delay}	time delay between wing translation and flexion
t_{span}	time required for wing flexion

ABSTRACT

Liu, Yun PhD, Purdue University, August 2016. Three Dimensional Unsteady Flow and Active Morphing Effect in Flapping Wings. Major Professor: Xinyan Deng, School of Mechanical Engineering.

Bumble bee cannot fly, if we ignore the significant differences between flapping wings and fixed wings, and falsely apply the conventional fixed wing aerodynamic principles to the bumble bee flight. The classic fixed wing aerodynamics originated from the two-dimensional attached flow analysis, where the three-dimensional and unsteady effects can be ignored without introducing too much error. Insects and hummingbirds, however, flap their low aspect ratio and highly deformable wings reciprocally, creating very complex flow structures, which are highly three-dimensional and unsteady. In the meanwhile, the flexibility and complex textures of the wings introduce even more complexities to the problem from the aspect of aero-elasticity. Therefore, to see the entire picture of flapping wing aerodynamics, the three factors: **unsteadiness**, **three-dimensional effect** and **wing morphing** have to be taken into account and this thesis aims to provide some understanding about those issues and the couplings related to them.

The state of art V3V system was used to study the coupling between **unsteadiness** and **three-dimensional effect** of the flow on a mechanical flapper with rigid wings, revealing a linked vortex ring structure in the near field with two layers of strong vortical flow in the far field. On the other hand, the coupling of **unsteadiness** and **wing morphing** was studied on a quasi-2-dimensional translating wing with an active trailing edge flap, suggesting both the flow and force characteristics were greatly affected by the flap deflection timing. Finally, to study the coupling of all the three factors: **unsteadiness**, **three-dimensional effect** and **wing morphing**, a new method of flow visualization was successfully developed and applied to freely

flying hawkmoth. For the first time, the entirety of the highly three-dimensional and unsteady vortex structure was observed and reported experimentally on a freely flying insect.

LIST OF PUBLICATIONS

Y Liu,J Roll, S.M. Van Kootan, S P. Sane, X Deng, Insect fly on ladders of vortices. *Submitted*

Y Liu,B Cheng, S P. Sane, X Deng, Aerodynamics of dynamic wing flexion in translating wings. *Exp.Fluids.* 56:131, 2015

B Cheng,J Roll,**Y Liu**, D R Troolin, X Deng, Three-dimensional vortex wake structure of flapping wing in hovering flight. *J.R.Soc.Interface.* 11(91), 2014

Y Liu,B Cheng,X Deng, An application of smoke-wire visualization on a hovering insect wing. *J.Vis.* 16(3),185-187, 2013

Y Liu,B Cheng,G Barbera, D RTrooling, X Deng,Volumetric Visualization of the near- and far- field wake in flapping wings. *Bioinspir.Biomom.* 8,2013

Y Liu,B Cheng, X Deng, An experimental study of dynamic trailing edge deflections on a two-dimensional translating wings. *31st AIAA Applied Aerodynamic Conference* AIAA 2013-2816

1. INTRODUCTION

1.1 Background Overview

Lifting-line and airfoil theories, developed in the early 20th century, opened a new era of fluid mechanics and paved the foundation of modern aerodynamics. Before the 1950s, without the modern computer technology, lifting-line and airfoil theories were the most fundamental guidelines in aircraft designing and optimization(Anderson 1999). In the light of advancements of the fixed wing aerodynamic theories, aircraft designing experienced booming and significant advancement in the early 20th century. The fixed wing aerodynamic theories were so successful that people intended to use these theories to study the aerodynamics of flying insects without considering the fundamental difference between fixed and flapping wings (Bomphrey et al 2009). The well-known "bumble bee cannot fly story" about the discussion between an aeronautic engineer and a biologist then became a major motivation behind the over a century research interests on insect flight (Bomphrey et al 2009, Sane 2003). Insect wings translate and rotate at quite a high angle of attack where the flow already separates from the fixed wings, resulting in a high drag but low lift force. Subsequently, the lift force is greatly underestimated, if using the aerodynamic force data derived from classic fixed wing aerodynamics, creating a false paradox that bumble bee cannot fly (Bomphrey et al 2009).

On a small chalcid wasp, Encarsia Formosa, Weis-Fogh found and proposed the "Clap-Fling" mechanism attributing to lift augmentation(Weis-Fogh 1973). By creating two bound vortices with opposite signs on the wings after pronation,"Clap-Fling" can prevent the formation of starting vortices to eliminate the Wagner effect which tends to weaken lift generation. However, this novel mechanism is only found in limited insect species such as butterflies with a great range of insects not having

"Clap-Fling" mechanisms captured in their flights. After Weis-Fogh, C.P. Ellingtion inherited his legacy and continued the research to determine the legitimate cause of high lift production in insect flight.

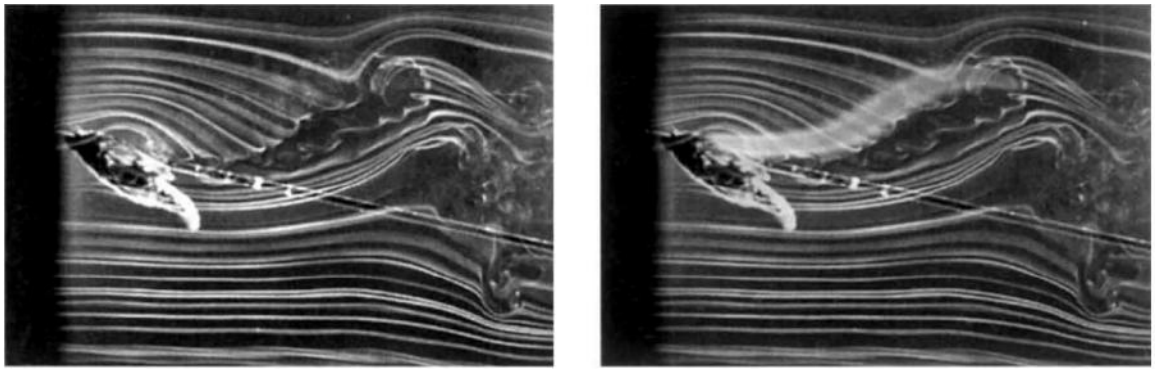

Figure 1.1: Smoke Visualization on tethered Hawkmoth(Ellington et al 1996)

Utilizing the smoke visualization on the tethered Hawkmoth, Manduca sexta, as well as a hawkmoth mimicking mechanical flapper (which not only can mimic the wing trajectory but also the flexibility of the hawkmoth wings), a cone shaped leading edge vortex (LEV) was captured and visualized (Ellington et al 1996,Van den berg and Ellington 1997). Most significantly, Ellington clearly linked this finding of stable LEV structure to the cause of high lift production which cannot be fully explained through classic fixed wing aerodynamics, thereby providing one explanation to the paradox that a bumble bee cannot fly. Through the discovery of LEV on the hawkmoth, Ellington may have provided the final answer to the unexpected high lift generation in insect flight while his work also brought more interesting aspects and questions about LEV which is currently believed to be the major cause of lift augmentation on animal flight. In addition, a great amount of research attention and interest was drawn into the mechanism about stabilizing the LEV on the wing (Birch and Dickinson 2001). Many theories and hypothesis were proposed, leading to an endless debate over this topic (Lentink and Dickinson 2009, Cheng et al 2013). Within these, a research group from Caltech, led by Prof. Dickinson, advanced the research on

insect flight to a higher level by studying the aerodynamics of fruit flies (Dickinson et al 1999).

Considering the wings of the fruit fly as rigid wings, Dickinson and his colleagues built a scaled up mechanical flapper-Robofly,that flapped at a much lower frequency in an oil tank to dynamically simulate the flying fruit fly in the air. By measuring the flow on the wing, Dickinson confirmed Ellington's finding about the existence of LEV, but found no relevance about the span-wise flow and LEV stability which is highlighted in Ellington's experimental results on the hawkmoth (Birch and Dickinson 2001). Furthermore, through systematic and detailed force and flow measurements on the Robofly, Dickinson and his colleagues built the first mature aerodynamics model that can estimate the aerodynamic force on flapping wings (Dickinson et al 1999). Although the quasi-steady model is empirical and experimental data dependent, it provides a sound and accurate force prediction.

In light of advancements in Computational Fluid Dynamics (CFD) and massive fast computation capacities, simulating flow and dynamics on flying insects became possible through solving the Navier-Stokes equation numerically. From simulations on flying hawkmoth to fruit flies, Liu (Liu et al 1998,Aono et al 2008) depicted very complex highly three-dimensional and unsteady flow structures on flying insects. Challenges in the simulation of insect flight stem from the complex nature of reciprocal flapping wing motion and wing geometries. Three-dimensional dynamic and adaptive mesh were used to cope with the complex wing motion that requred constructing new mesh for calculation at each time step (Liu et al 1998). Later, by introducing the immersed boundary method (IBM) to CFD simulations of insect flight, the mesh was greatly simplified without considering too many geometric complexities (Mittal et al 2006). Moreover, instead of solving the Navier-Stokes equation, the Lattice Boltzmann Method was implemented to study the low Reynolds number flow problems, like flapping wings (Li and Lu 2012). However, none of these simulations can perfectly simulate a flying insect by considering all the details from wing morphology to wing texture. Therefore, all these CFD simulations are still based on more or less

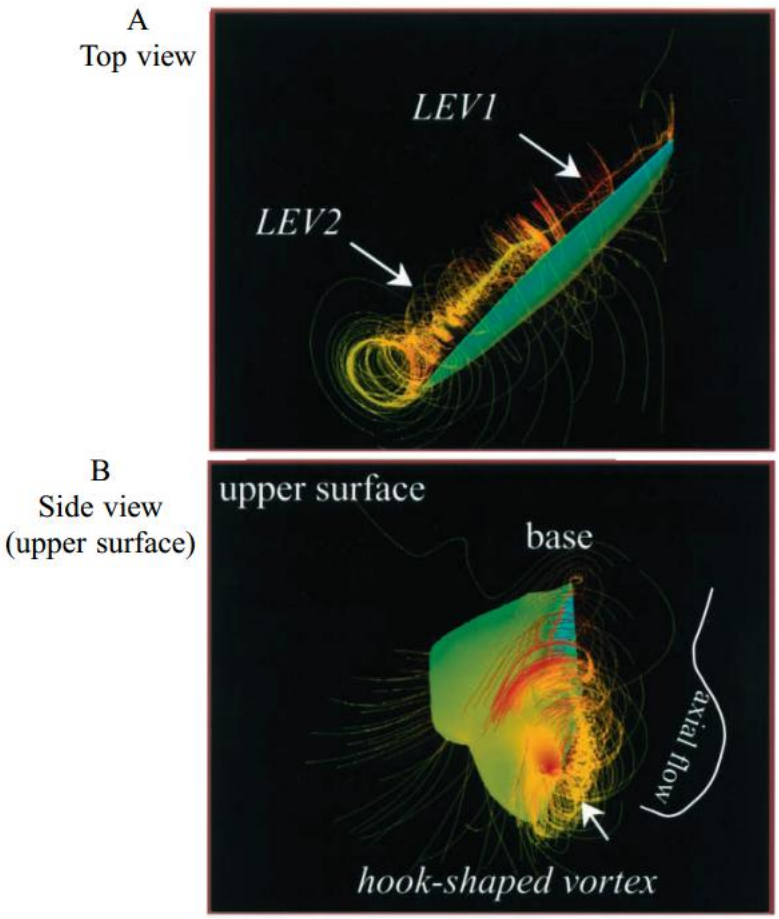

Figure 1.2: Top and side views of CFD-visualized flows with instantaneous streamlines and surface pressure contours during supination(Liu et al 1998)

simplified flying insect models which might neglect some important features on real flying insects (this issue will be addressed in Chapter 5).

In the recent decade, with the advancement of three-dimensional flow measurement/visualization methods, a much clearer picture about the flow in insect flight can be obtained not only on insect mimicking mechanical flappers but also on real flying insects (Liu et al 2013, Henningsson et al 2015). With knowing the highly unsteady and three-dimensional flow structure details, aerodynamic force and other metrics can be calculated and studied to gain a deeper understanding about the correlation between unsteady force generation and complex flow structure (Wu 1981). In the meanwhile, unlike quasi-steady model, several aerodynamic models have been proposed in

the hope of resolving the unsteady aerodynamic force on flapping wings without using empirical and experimental data (Ansari et al 2006,Nabawy and Crowther 2014). CFD simulation, on the other hand, is far ahead of experimental studies and capable of resolving many details about the complex flow and aerodynamic forces on flying insects based on extracted kinematics data (Wan et al 2015,Song et al 2014). However, no matter how advanced are these methods, either numerical simulations, experimental investigations or theoretical modelings, there are mainly three challenges and features inherent in the nature of flapping wings, have to be considered: **Unsteadiness**, **Three dimensional effect**, and **wing morphing**.

1.2 Three fundamental features on the aerodynamics of insect flight

Unsteadiness is one of the most inherent features in insect flight. An accelerating plate, started from rest, is one widely used approximation for flapping wing motion which is subjected to significant linear acceleration/deceleration. By measuring the instantaneous force on impulsively started translating plate under different angles of attack, Dickson found the lift force is significantly augmented in the first 2 chord lengths of travel compared with the one measured 5 chord lengths later(Fig.1.3). Through flow visualization, this lift augmentation was found related to the time dependent formation of attached leading edge vortex in the first 2 chord lengths of travel. However, this leading edge vortex is not stable and shed afterward (Dickinson and Gotz 1993). Pulling and Wang studied a quite similar problem analytically by modeling the leading edge vortex and the starting vortex as growing spiral vortex sheets and found the angle of attack for maximum vortex lift is about fifty degrees and independent of acceleration profile (Pulling and Wang 2004). Instead of linear accelerations, the angular acceleration is another significant factor found on insect wings which are subject to fast changes in angles of attack. Using two-dimensional potential flow theory and point vortex modeling, Xia (2013) simulated the flow on a dynamic pitching plate to study the effect of dynamic pitching and found the instan-

taneous force on the plate is highly dependent on the motion of vortices formed from the leading edge and trailing edge. Moreover, two-dimensional rigid plates undergoing complex flapping wing motions, have also been extensively studied and investigated through experiments to resolve the significance of unsteadiness on flapping wings. Through measuring the unsteady flow and forces on a rigid large aspect ratio flapping plate, Lua and his colleagues (2008,2010,2011) studied the unsteady effect of flapping wing due to pitching phase, flapping frequency and angular amplitude. The wake capture mechanism was also investigated in their study, indicating the wake capture mechanism will not always augment the lift force generation on a flapping wing.

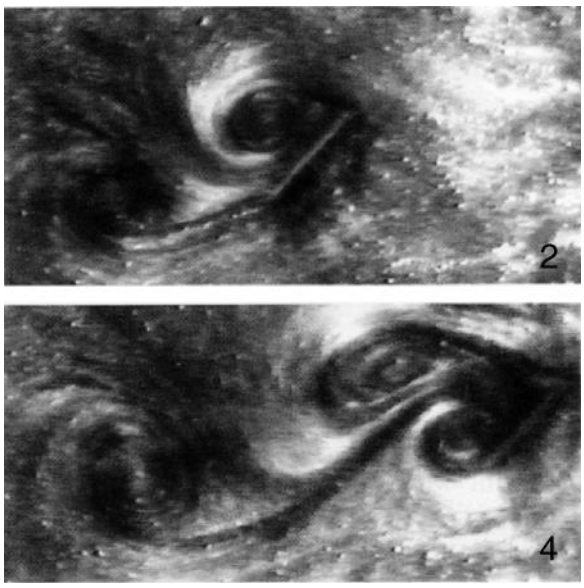

Figure 1.3: 2D flow visualization on translating plate(Dickinson and Gotz 1993)

Owing to the limitations and drawbacks of current flow diagnostics and measurement methods through the decades, one of the biggest difficulties in studying the aerodynamics of insect flight is the strong three-dimensional effect of the flow which is quite different from the flow on conventional fixed wings. The majority of current flow dialogistic methods are limited to the planar flow field measurement which can either measure the two dimensional flow velocity field on a plane or provide the three

dimensional flow velocity vector on the plane (Poelma et al 2006, Bomphrey et al 2006). With the early implementation of these traditional techniques on studying the flow of flying insects and mechanical flappers, many details about the flow have been observed and reported. Yet, without a completely clear depiction of the complex flow structure in three dimensions, the actual flow topology on flying insects can never be obtained and observed. Bomphrey (2006) applied a 2D-PIV on a tethered hawkmoth in the wind tunnel and found the leading edge vortex is continuing from the left to the right wing and crosses over the thorax, suggesting a likely single vortex ring wake topology on the flying hawkmoth in the down-stroke. However, the CFD simulations on the flying hawkmoth model didn't capture and confirm this feature of continuing leading edge vortex crossing over the thorax (Aono et al 2008,Zheng et al 2013); Instead, two horse-shoe shaped vortex loops were presented in the simulation with each wing generating a vortex loop. Dickinson and his colleagues used stereotype PIV to measure the flow around a mechanical flapper, mimicking a flying fruit fly. By proper alignment of all the stereo-PIV measurements on different planes around the wing, the final three-dimensional flow structure was finally reconstructed from the interpolated flow data (Poelma et al 2006). However, this method with stereotype PIV is not feasible and accurate as studying the evolution of the three dimensional flow structure on real flying insects whose wing trajectories are in a great variation from wing beat to wing beat, leaving the flow measurement of this kind unreliable. Recently, with advancements in volumetric flow measurement/visualization techniques, the instantaneous three-dimensional unsteady flow around flapping wings can be measured in a more accurate and efficient way. Defocusing DPIV was utilized to study the three-dimensional flow on translating and rotating plates in a water tank (Kim and Gharib 2010). The differences about the flow structure between translating and rotating wing were captured and studied in great detail with the complex vortex structures visualized in three-dimension. The same method was also used in studying mechanical flappers in an oil tank, simulating the flying insect flight in the air dynamically (Liu et al 2013, Cheng et al 2014). As expected, strong three dimensional

effects of the flow were clearly observed with the complex vortex structure being continuously under significant deformation and convection with the downwash flow. For the first time, the overall vortex structures and their evolution have been captured and observed on mechanical flappers volumetrically. However, it is still quite a challenging task to measure the three-dimensional flow on flying insects in the air. Most recently, a large volume tomo-graphic PIV measurement was conducted in the wake of a tethered locust in a wind tunnel (Henningsson et al 2015). Instantaneous three-dimensional vortex structures and their development were quantitatively visualized with some quite interesting and new structures observed(Fig.1.4).

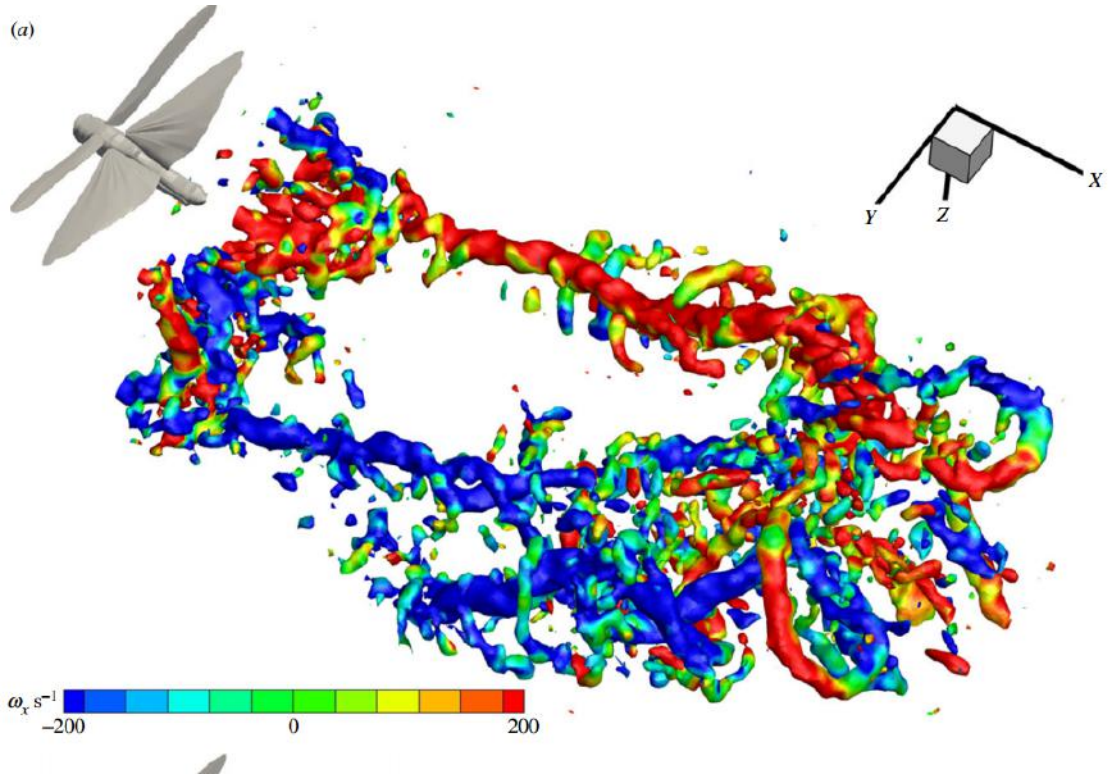

Figure 1.4: Instantaneous flow measurement on a tethered locust,using tomographic PIV(Henningsson et al 2015)

The flexible wing of flying animals plays another important role in defining the aerodynamics of insect flight and is frequently related to the consideration of efficiency. Through the CFD simulations on a locust with different types of wing stiffness and

flexibilities, researchers were able to demonstrate the advantages of real flexible wings on flying locusts in terms of high flight efficiency (Young et al 2009). Zhao(Zhao et al 2009) conducted a systematic experimental investigation on the topic of aero-elasticity in flapping wings, using mechanical flapping wings made of isotropic material with a broad spectrum of wing stiffness. The results show the force modulations by means of changing wing stiffness and suggest a strong correlation between wing stiffness and leading edge vortex strength. Relevant CFD simulations were carried out on rotating wings with different wing cambers (Harbig et al 2013). Very interestingly, positively cambered wings were found to have higher lift to drag ratio, comparing to negatively cambered and flat wings. Similarly, on fish, CFD simulations and experimental studies have already shown the flexible bodies cannot only produce significant thrust during maneuvers but also can harvest energy from the vortical flow to gain sufficient propulsive force to overcome body drag (Liao et al 2003,Beal et al 2006). Additionally, the soap film experiments on flexible filament demonstrate a great hydrodynamic influence on the wake as well as the morphology of the filament in the subject to the fluid-structure interaction (Zhang et al 2000).

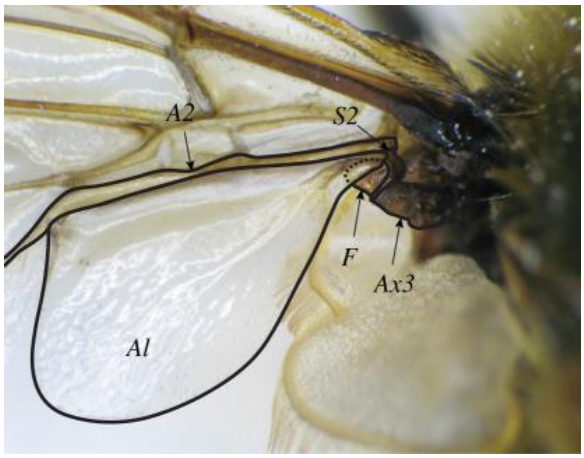

Figure 1.5: Left wing of Eristalis tenax, showing the attachment of the alula (Walker et al 2012)

Although the effect of wing flexibility under passive deformation has been studied and addressed in numerous literature, the aerodynamics effect of active wing morph-

ing on flapping wing is not well studied and understood. Especially, the active wing camber and trailing edge flap deflection are well observed in the flapping animals such as bats, birds and insects (Wolf et al 2010;Norberg 1976; Ennos 1987). Bats use their articulated fingers and arms to actively control the wing camber in order to adjust their aerodynamic performance under different flying speeds (Wolf et al 2010). Insect wings, on the other hand, are mainly passive structures and driven by sets of muscles in the thoraxes. However, alula, a unique "flap" like structure at the wing base of most hoverflies, can be actively driven via the third axillary sclerite to change the instantaneous flap angle (similar to the flap mechanism on the modern aircraft) at the wing base(Walker et al 2012)).

On real flying animals, **Unsteadiness**, **Three-dimensional effect** and **Wing morphing** are deeply interacted and coupled with each another, resulting a complex aerodynamic behavior(See Fig.1.6). Among those couplings, the coupling between three-dimensional effect and unsteadiness can best present the most important features of insect flight; The coupling between unsteadiness and wing morphing, on the other hand, is an appropriate approach to study the fundamental physics of wing morphing effect in flapping wings without considering complexities induced by **three-dimensional effect**. Finally, to have a comprehensive and accurate understanding about the aerodynamics of insect flight, it is imperative to consider the coupling among all the three factors. In this thesis, those types of couplings will be studied and addressed accordingly in the following chapters.

1.3 Outline of the thesis

To study the coupling between unsteadiness and three-dimensional effect, chapter 2 presents a volumetric flow measurement study on a pair of rigid mechanical flapping wings by using the volumetric 3-component velocimetry (V3V) in an oil tank. The complete three-dimensional wake structure and its evolution throughout a wing stroke were quantified and presented. It was found that the general vortex structure consists

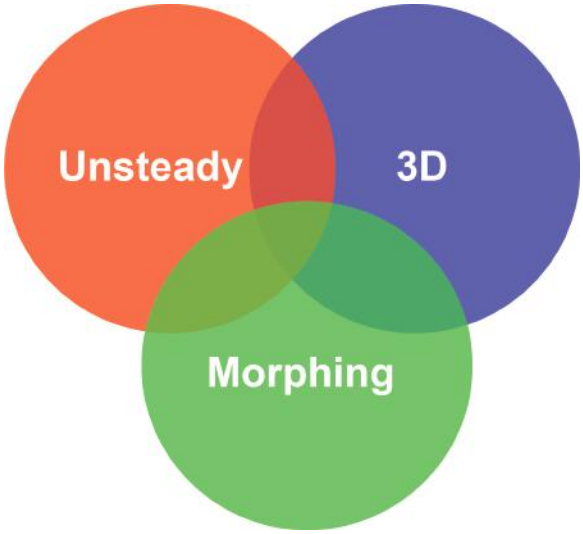

Figure 1.6: Three basic features in aerodynamics of insect flight

of linked vortex rings in the near field and two layers of strong vortical flow in the far field. The downwash flow, on the other hand, is directed passing through the center of the vortex rings in the near field and extends downward between the two-layer structure.

In Chapter 3, a quasi- 2 dimensional translating wing starting from rest is studied to simulate the unsteady motion of flapping wings with its trailing edge flap deflecting at different timings and speeds. In this sense, the coupling between unsteadiness and active wing morphing can be studied without introducing the complexities due to three-dimensional effect and its couplings with other factors. The results indicate the wing deflection timing plays a more important role in the force and flow modulation while the deflection speed can only weakly modify the force and flow characteristics.

In Chapter 4, conventional smoke and dye visualizations were applied and tested on mechanical flappers in the air and water. In Chapter 4 section 1, a new smoke visualization method was implemented on a four-bar mechanism flapper with zero free stream velocity to simulate the flow structure on a hovering wing. It was found that the downwash flow is confined by the tip and root vortices on the frontal plane but is diverging on the para-sagittal plane. However, this visualization technique can

only visualize the flow which passes the smoke wire and the flow structure otherwise cannot be visualized. Therefore, in chapter 4 section 2, dye visualization method was tested in the water. To visualize the entire vortical flow, fluorescent dye was applied to the surface of the flapping wing in a water tank. By using this method, the entire near wall flow feature as well as the flow features convected in near wake can be visualized. It was found that throughout the flapping cycle, the tip and root vortices dominant the wake flow.

In Chapter 5, an innovative flow visualization method is developed and applied on a freely flying hawkmoth to study the authentic vortical flow on flying insect which is subject to the coupling of unsteadiness, three-dimensional effect and wing morphing. By observing the trace of alcohol vapor from the wing surface through a high speed Schlieren system, all the major vortices and their evolution were successfully visualized in a three-dimensional space, presenting a sophisticated linked vortex structure on freely flying insects.

2. VOLUMETRIC VISUALIZATION OF THE NEAR- AND FAR-FIELD WAKE IN FLAPPING WINGS

Published in Bioinspiration and Biomimetics 2013 (First Author: Yun Liu)

2.1 Chapter Abstract

The flapping wings of flying animals create complex vortex wake structure; understanding its spatial and temporal distribution is fundamental to animal flight theory. In this study, we applied the volumetric 3-component velocimetry to capture both the near- and far-field flow generated by a pair of mechanical flapping wings. For the first time, the complete three-dimensional wake structure and its evolution throughout a wing stroke were quantified and presented experimentally. The general vortex wake structure maintains a quite consistent form: vortex rings in the near field and two shear layers in the far field. Vortex rings shed periodically from the wings and are linked to each other in successive strokes. In the far field, the shed vortex rings evolve into two parallel shear layers with dominant vorticity convected from tip and root vortices. The shear layers are nearly stationary in space compared to the periodic vortex rings shed in the near field. In addition, downwash passes through the centers of the vortex rings and extends downward between the two shear layers.

2.2 Introduction

Small flying animals, such as insects and hummingbirds, exhibit a ubiquitous ability of hovering (Ellington 1984,Dudley 2000, Fry et al 2005). They flap their wings back and forth at large angle of attack (AoA) while pushing airflow downwards with shed vortices (Warrick et al 2005). The aerodynamics of the flapping wings, which has been widely studied in the past decades, has strong unsteady and three-dimensional

properties (Sun and Tang 2002, Sane 2003, Lentink and Dickinson 2009,Sane 2011). Recently, progress on volumetric flow visualization (Pereira et al 2000) has allowed more detailed three-dimensional flow measurements that further decode these properties (Kim and Gharib 2010, Cheng et al 2013).

While the majority of these studies have focused on the characteristics of the near-field flow without considering the effect of the far-field wake, studies on helicopter aerodynamics (Leishman 2006) and flow past a cylinder (Wu et al 2007) have suggested that the far-field wake might play a role in the local field aerodynamics. Indeed, as shown by Birch and Dickinson (2001), induced flow due to far-wake vorticity significantly reduces the effective wing AoA of flapping wings and therefore affects lift production. Using conventional vortex theory, Ellington (1978, 1984), and Rayner (1979), have modeled the wake of a hovering animal as a chain of coaxial vortex rings, and successfully showed some far-field features and stroke-averaged parameters of flapping wings. A recent study based on vorticity moment theory further revealed more complex behavior of these vortex rings and their mutual interactions (Wang and Wu 2010). In comparison, numerical simulation results have suggested quite different wake structures than stacked vortex rings (Aono et al 2008,Yu and Sun 2009). For example, Yu and Sun found the tilted-and-linked vortex rings with large jet-like flow through the center of rings.

On the other hand, experimental studies on animal wake structures were mainly focused on forward flight (Johansson and Hedenstrm 2009, Muijres et al 2008, Spedding et al 2003, Bomphrey et al 2009). It was found that two wings can produce either a single vortex ring (Muijres et al 2008) or two separate vortex rings (Spedding et al 2003). In normal hovering, however, flapping wings are more likely to produce two separate rings because zero body circulation leads to shed wing root vortices (Pournazeri et al 2013).

Additionally, measurements of the far-field flow are important in studying the flight control and sensory-motor physiology. For instance, recent studies have suggested that hovering birds are able to utilize the downwash through active tail move-

ments (Altshuler et al 2009, Su et al 2012). It was found that a hovering passerine creates periodic tail movements, which were time-phased with wing motion to intercept the periodic downwash in the wake, thereby creating pitch torque that reduced the body oscillation (Su et al 2012). In addition, Sane (Sane 2006, Sane and Jacobson 2006) has suggested that in flapping insects, their airflow sensors, olfactory sensors, heat exchange and various mass exchange processes are all influenced by the induced flow.

Therefore, to advance the animal flight theory, it is desirable for both biologists and engineers to have a comprehensive understanding of the wake structure generated by flapping wings. In this study, we used the volumetric 3-component velocimetry (V3V) (Cheng et al 2013, Pereria et al 2000, Flammang et al 2011) technique to measure both the near- and far-field flow generated by a pair of mechanical flapping wings. For the first time, we provide experimental results for the three-dimensional wake structure of the flapping wings and describe its evolution throughout the wing stroke.

2.3 Materials and Methods

A dynamically scaled mechanical flapper (Fig.2.1(a)) was used to generate wing flapping motion. Pair of wings were driven by a single digital servo (Hitec Inc., Poway, CA, USA) to flap sinusoidally at 2 Hz. The wings were allowed to rotate passively and create varying angles of attack (AoA), which were limited by two stoppers mounted on the wing roots. The wing had a span of 55 mm (from wing tip to center of rotation) and an aspect ratio of 5.3. It was made from a transparent polymer sheet with a uniform thickness of 0.5 mm (Fig.2.1(b)). The mean Reynolds number was approximately 700 which is within the range of insect flight. It was estimated using the following equation:

$$Re = \frac{4\theta R^2 n}{\gamma AR} \tag{2.1}$$

where θ means the stroke amplitude (peak to peak in radians), R is the wing span-length, n is the flapping frequency, γ is the kinematic viscosity and AR is the aspect ratio. In this study, the three-dimensional velocity field in both the near and far field of the flapping wings was measured using volumetric 3-component velocimetry system (V3V; TSI Inc., Shore-view, MN, USA). Its principle is based on processing of defocusing images which is similar to how human eyes perceive depth; while a conventional camera with one aperture could only capture particles' location information on a plane, the V3V camera which has three off center apertures with identical focusing plane can record the spatial location of particles in a volume. By determining the dimension of three defocusing images of one identical particle, the third dimension of the particle location can be obtained (for details, refer to Pereira and Gharib (2002), Troolin and Longmire (2010)).

The uncertainty in the instantaneous velocity fields comes primarily from spatial uncertainty. Spatial uncertainty results from mean-bias and RMS errors and has been shown by Pereira and Gharib (2002) to be on the order of 1% for the X and Y velocity components (the width and height) and 4% for the Z component (depth). Temporal uncertainty is negligible in comparison since the jitter in the laser pulse timing is 10 ns, and the timing resolution of the synchronizer is 1 ns.

In the experiment, the oil tank ($61 \times 61 \times 305\, cm^3$), filled with mineral oil (Kinematic Viscosity = 8 cSt at 20^oC, density=$850\, kg/m^3$), was seeded with air bubbles (average size of 20-50 microns) which were illuminated by a dual-head Nd:YAG pulsed laser. The measurement volume ($14 \times 14 \times 10\, cm^3$, Fig.2.1(a)) was positioned in the center of the tank. Note that, the tank dimension was significantly larger than the wing length and the V3V measurement volume, and according to Sane (2001), the wall effect is negligible if the wing is two times the wing length away from the wall.

To capture the complete evolution of the flow structure around the flapping wing, measurements were conducted at 16 different time instants within one flapping cycle with a time interval of 31.25 ms. (In Fig.2.1(d), the number 015 indicates the 16 different wing stroke positions with a time interval of 31.25 ms in one flapping cycle.)

The final velocity data at each wing stroke position was obtained from an ensemble-average flow result of 20 consecutive wing beats after the first 5 wing beats, which ensured the flow was fully established. InsightV3V software (TSI Inc., Shoreview, MN, USA) was used to carry out the particle detection, particle tracking and velocity field interpolation. Three components of velocity on a $45 \times 45 \times 31$ mesh grid were obtained at each stroke position. Finally, the velocity fields were then post processed using MATLAB (The Mathworks, Natick, MA, USA).

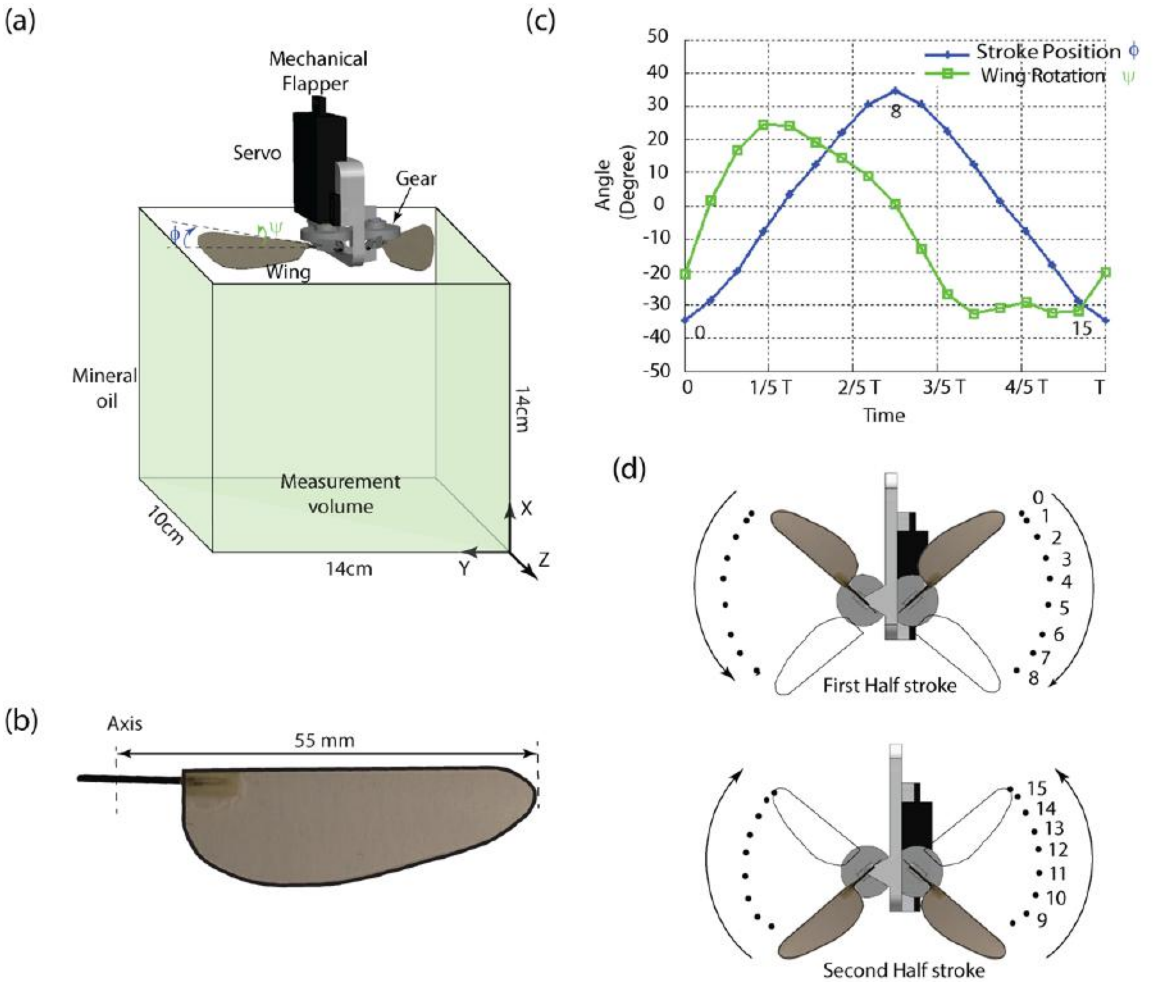

Figure 2.1: Experimental Setup (a) Schematics of the servo driven mechanical flapper and the measurement volume of the V3V system. (b) Wing profile. (c) Measured stroke and rotation angle (b) Wing stroke positions where the velocity field was measured.

The wing kinematics (Fig2.1(c)) was extracted from the raw images by reconstructing the spatial locations of the wing profile using the MATLAB program. Its repeatability was examined by ensemble-average of the raw images from 20 flapping cycles at each wing stroke position, which showed an almost perfect overlap for the wing profile at the same wing stroke position. Note that, in the experiment, a stopper with a $\pm 45^o$ range was used to limit the wing rotation. The wing plane was aligned with the central plane of the stopper. The purpose of using the stoppers was to guarantee the rotation angle never exceeding 45^o; and in fact, during the experiments, the rotation angle did not reach 45^O in any flapping cycle, which indicates that the stoppers were actually not touched.

2.4 Results

In the current experiment, because the left and right wings showed similar flow patterns, only the results of the left wing will be discussed. The basic vortical flow structure is visualized by plotting isosurfaces of vorticity magnitude. At the end of a stroke (wing stroke position 0, Fig.2.1(c)), two distinct vortex rings are observed (Fig.2.2(a) and (b)) which are tilted and connected to each other (similar to the vortex rings structure in Yu and Sun (2009)). In the far field, however, there are no distinct ring structures; instead, two parallel shear layers (Fig.2.2(a) and (c)) with relatively low vorticity magnitude are observed (but not discussed in Yu and Sun (2009)). As will be shown later, although the development of shear layers is a highly unsteady process with the periodically generated vortex rings in the near field, the shear layers remain relatively stationary in space with small variation. To further illustrate the distribution of vorticity, RGB colors were applied to represent the magnitude of the three orthogonal vorticity components ($\mid \omega_x \mid \mid \omega_y \mid \mid \omega_z \mid$, Fig.2.2(b) and Fig.2.2(c)); a similar method was used in Cheng et al (2013). From Fig.2.2(b), it can be seen that the Y vorticity (green) is mainly distributed along the wing span and in the conjunction region of the two vortex rings, which corresponds to the leading-edge

vortex (LEV) and shed vortices during stroke reversals (Birch and Dickinson 2003). On the other hand, the vorticity closest to the wing tip/root arcs are dominated by Z and X vorticity (blue and purple in figure 2(b)), corresponding to the wing tip and root vortices (TVs and RVs). These vortices travel downward into the wake and evolve into two parallel shear layers dominated by Z vorticity (blue, figure 2(c)). Conversely, the strength of Y vorticity significantly decreased in the far field. From contour slices of the plot in Fig.2.3(a), it can be seen that the two parallel shear layers have opposite signs of Z vorticity (corresponding to TVs and RVs); in addition, a downward jet passes through the centers of the linked vortex rings and extends downward between the two shear layers (red isosurface, Fig.2.3(b)). The velocity vector field on two perpendicular slices is shown in Fig.2.3(c). Note that in the near field, the jets induced by the two vortex rings are oriented in different directions but in the far field, the flow between the shear layers is approximately unidirectional (downward and to the right, Fig.2.3(c)).

In the next section, the evolution of the vortical structure throughout the flapping cycle is discussed. Fig.2.4 shows a time sequence of color-coded isosurfaces of vorticity magnitude, together with two perpendicular slices showing Z and Y vorticity contours and planar streamlines. The sequence starts at the onset of stroke reversal (stroke position 0, Fig.2.4) when the two vortex rings have been formed (described above), and the leading edge vortex (LEV) is clearly seen on the XZ slice. The wing then rotates and changes stroke direction, and new vorticity is created along the leading edge. As the wing continues to move, the LEV connects the vorticity shed at stroke reversal through the wing tip and root vortices (wing stroke positions: 46), and then a new vortex ring is formed as the half stroke is completed (stroke position 8). Notably, in this half stroke (stroke positions 08), as the new vortex ring forms, the previous vortex rings convect downward and begin to dissipate, especially for the Y vorticity (Fig.2.4, XZ slice, stroke position 48). However, the Z vorticity remains strong in the wake as the TV and RV merge into parallel shear layers in the far field (XY slices in Fig.2.4).

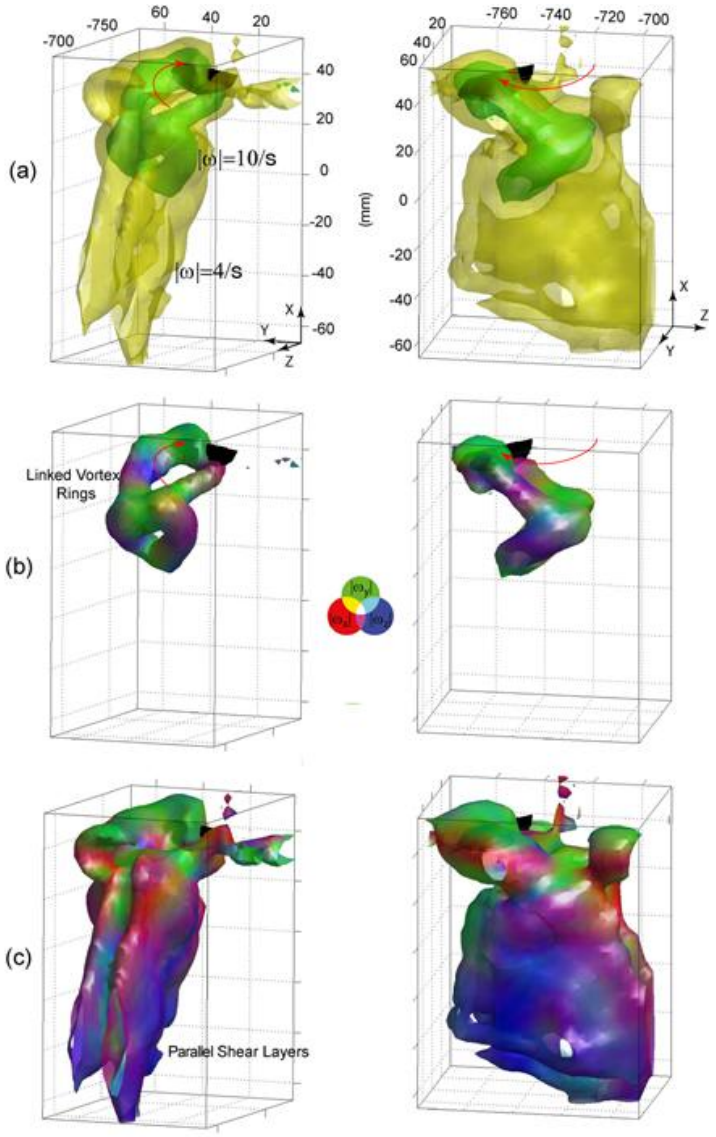

Figure 2.2: Isosurfaces of vorticity magnitude $|\omega|$ at wing stroke position #0. (a) Two isosurfaces with $|\omega|$= 4/s (yellow) and $|\omega|$= 10/s (green). (b) The RGB color-coded (red, ω_x; green, ω_y; blue ω_z) isosurface ($|\omega|$= 10/s) showing two linked vortex rings. (c) The RGB color-coded isosurface ($|\omega|$= 4/s) showing two parallel shear layers. Left and right columns show the same isosurfaces at two different views

The next wing half stroke starts at position 8, and a new vortex ring begins to form while the vortex ring from the previous stroke convects with the downwash. However, unlike the preceding half stroke, the shed vortex ring remains intact without significant dissipation; and the two distinct connected vortex ring structures described

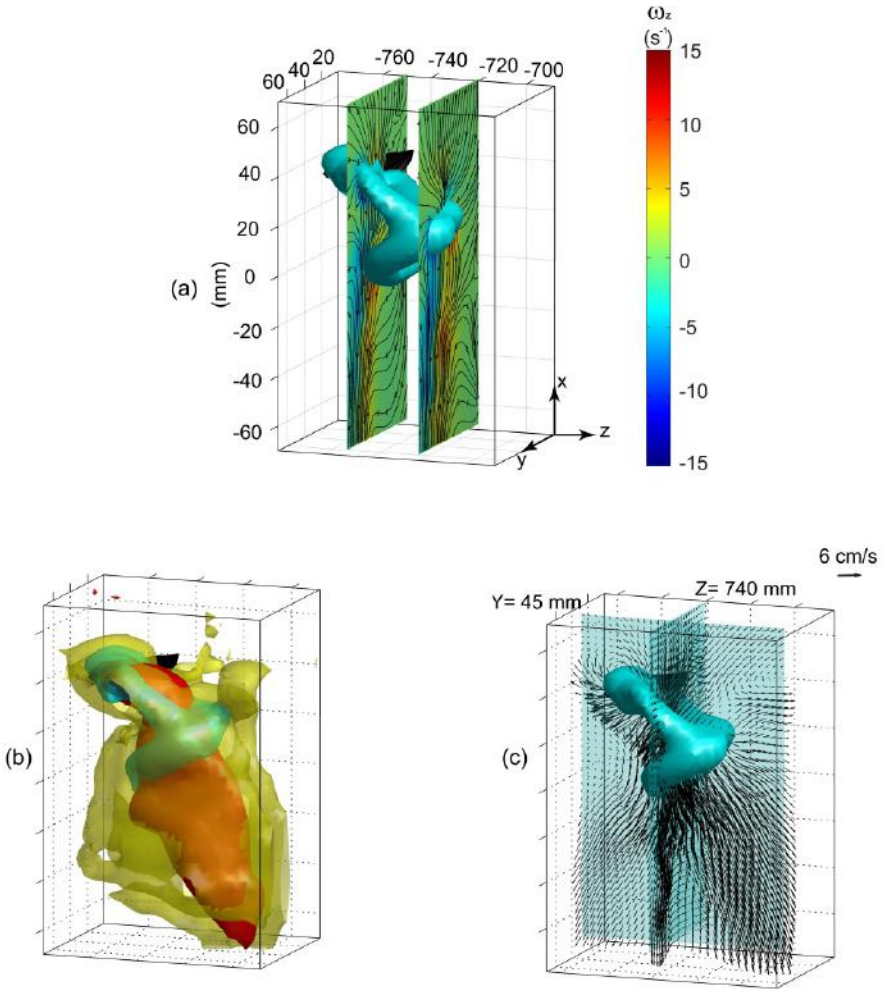

Figure 2.3: Vorticity and velocity distribution at wing stroke position 0. (a) 2D slices showing Z vorticity contour and streamlines at Z = -720 and -750 mm, and isosurface of vorticity magnitude at with $|\omega|$= 4/s. (b) Isosurface of velocity magnitude (red) at 8.5 cm/s, which is enclosed by the isosurfaces of vorticity magnitudes at $|\omega|$= 4/s (yellow) and $|\omega|$= 10/s (green). (c) Velocity vector field on the two perpendicular slices Z = -740mm and Y= 45mm

previously are observed. Again, the difference in vortex structures between these two half strokes is most likely due to the asymmetric AoA. The shed vortex ring destabilizes when the wing is traveling with a large AoA(about 65^o) and stays connected when the wing is traveling with a smaller AoA (about 55^o).

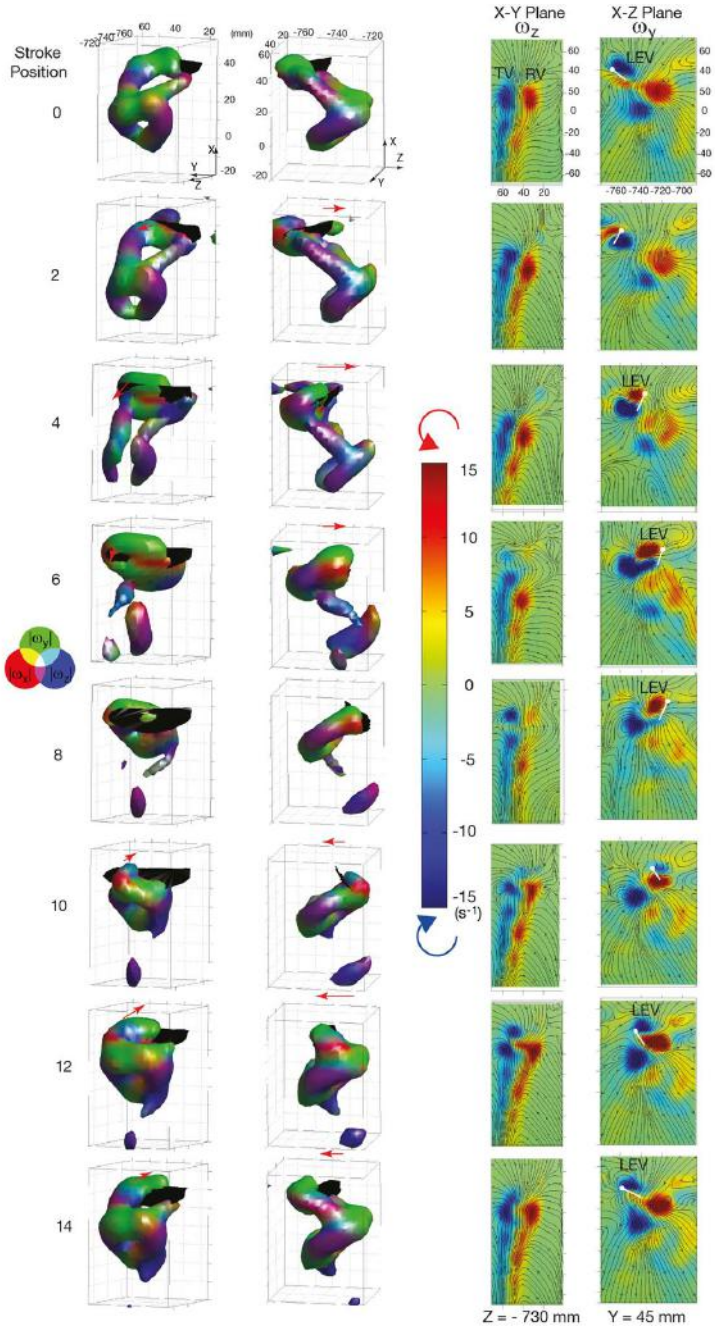

Figure 2.4: Isosurfaces of vorticity magnitude ($|\omega|$= 10/s) and vorticity contour plots at 8 different stroke positions, which demonstrate the evolution of the vortex wake structure. The contour plot of Z vorticity at X-Y plane (Z = -730 mm) shows the tip vortex (TV) and root vortex (RV) as well as two shear layers in the far field. The contour plot of Y vorticity at X-Z plane (Y= 45mm) shows the leading edge vortex (LEV) and other vortices shed at stroke reversals.

2.5 Conclusion and Discussion

By using the V3V technique, we presented here the first experimental results on the near- and far-field vortex wake structure of flapping wings, while previous studies were limited to the near field, using experimental visualization techniques (Birch and Dickinson 2003, David et al 2012). The three-dimensional flow field obtained from different stroke positions clearly elucidated the wake structure and its evolution throughout a flapping cycle.

At completion of each half stroke, the vortex ring shed was inclined with respect to the stroke plane. In the meanwhile, the inclined vortex rings tend to link to each other at the stroke reversals (Fig.2.2) for the wing half stroke with smaller AoA (915, figures 1(b) and (c)). For the wing half stroke with larger AoA (18, Fig.2.1(b) and (c)), the previously shed vortex rings appear to break with a loss of Y vorticity (Fig.2.4). However, despite the difference between the two successive strokes, the shed vortex rings eventually evolve into two separate shear layers with dominant vorticity convected from tip and root vortices (Fig.2.2). Therefore, the current result reveals a more complicated wake structure compared with the idealized model of coaxial vortex rings proposed in Ellington (Ellington 1978, 1984).

Collectively, the general vortex wake structure maintains a quite consistent form: vortex rings in the near field and two shear layers in the far field. The vortex rings are generated periodically from the wing while convecting downward into the far field and become relatively steady shear layers consisting primarily of Z vorticity from tip and root vortices. Concurrently, the jet downwash passes through the centers of the vortex rings and extends downward between the two shear layers.

Although the development of the shear layers, which is characterized by the rapid loss of Y vorticity and maintenance of Z vorticity in the wake, may need further investigation, it is apparent that Y vorticity is associated with more complex vortex shedding and interaction than Z vorticity which is continuously shed at the wing tip and root. As shown in the contour plot of Y vorticity (Fig.2.4) during the stroke

reversal, the LEV from the previous half stroke shed and merged with the starting vortex (SV) of the next half stroke; this phenomenon was also found in the previous 2D PIV results from Birch and Dickinson (2003). However, they also found a rotational starting vortex (RSV) due to active wing rotation at stroke reversals, which was not observed in the current study, possibly caused by the passive wing rotation.

While the current work revealed the three-dimensional wake structure of a flapping wing, it is important in future works to investigate how it varies with Reynolds number, wing morphological and kinematic parameters. For example, in a parallel study using V3V volumetric visualization (in preparation), we found a flapping wing with different wing shape, stroke amplitude (130), and the Reynolds number (2200) created similar shear layers' structure, suggesting it might be a common feature in the wake of flapping wings, at least within certain range of morphological and kinematic parameters. Nevertheless, systematic studies quantifying the effect of these parameters on both near and far field are still crucial and needed to the understanding of both dynamical (Altshuler et al 2009, Su et al 2012) and biological (Sane 2006, Sane and Jacobson 2006) processes of flying animals.

3. AERODYNAMICS OF DYNAMIC WING FLEXION IN TRANSLATING WINGS

Published on Exp in fluids 2015 (First Author: Yun Liu)

3.1 Chapter Abstract

We conducted a systematic experimental study to investigate the aerodynamic effects of active trailing-edge flexion on a high-aspect-ratio wing translating from rest at a high angle of attack. We varied the timing and speed of the trailing-edge flexion and measured the resulting aerodynamic effects using a combination of direct force measurements and two-dimensional PIV flow measurements. The results indicated that the force and flow characteristics depend strongly on the timing of flexion, but relatively weakly on its speed. This is because the force and vortical flow structure are more sensitive to the timing of flexion relative to the shedding of starting vortex and leading-edge vortex. When the trailing-edge flexion occurred slightly before the starting vortex was shed, the lift production was greatly improved with the instantaneous peak lift increased by 54% and averaged lift increasing by 21% compared with the pre-flexed case where the trailing-edge flexed before wing translation. However, when the trailing-edge flexed during or slightly after the leading-edge vortex shedding, the lift was significantly reduced by the disturbed development of leading-edge vortex. The force measurement results also imply that the trailing-edge flexion prior to wing translation does not augment lift but increases drag, thus resulting in a lower liftdrag ratio as compared to the case of flat wing.

3.2 Introduction

Flying animals in nature have greatly inspired the development of modern aviation technology over the past century. Originally inspired by soaring birds, the pioneers in aviation successfully invented gliders, thus making us capable of flight (Valasek 2012). Even to the early aviators, the significance of wing camber in aircraft flight control was evident. Indeed, wing camber was a crucial control element allowing the longitudinal, lateral and directional control on the Wright brothers glider over a century ago (Valasek 2012). Since then, the aerodynamic effect of wing camber has undergone extensive experimental and theoretical investigation (Batchelor 1967;Perry and Mueller 1987). Modern aircrafts require active control of wing camber by means of flap and slat deflection for a variety of maneuvers including landing and take-off. In recent decades, with the advancement of novel actuators and materials, the concept of morphing wings with smoothly varying camber was proposed, aiming to further improve the aerodynamic performance of modern aircrafts (Bilgen et al 2010; Santhanakrishnan et al. 2005; Gupta and Ippolito 2012).

Wing camber and trailing-edge flexion are also ubiquitous in the animals such as bats, birds and insects who use flapping wings for flight (Wolf et al 2010; Norberg 1976; Ennos 1987). In recent decades, flying animals have greatly inspired the development of flapping-wing micro-air vehicles (MAV) with superior flight maneuverability and hovering ability (Deng et al 2006; Ma et al 2013). In bats, active wing camber (produced by the articulated finger bones) is continually altered across the wingspan, during wing beat cycles, and at different flying speeds (Wolf et al 2010) which may lead to different flow features in the far wake of the forward flying bats (Johansson et al. 2008). Thus, bats may use their articulated fingers and arms to actively control the wing camber in order to adjust their aerodynamic performance at different flying speeds (Wolf et al 2010). In contrast to bats, insect wings are passive structures with no intrinsic muscles and are only driven by sets of muscles in the thoraxes from the wing roots. Previously, we showed that the dynamics of the passive trailing-edge

flexion is intimately connected to the strength of the leading-edge vorticity (Zhao et al.2009, 2011). In those experiments, the wing camber was passively obtained in wings of varying flexural stiffness. Therefore, unlike the bat wings, time-varying wing camber of the insect wings is mainly obtained from passive fluidstructure interactions coupled with the inertia effects (Valasek 2012; Walker et al 2010). One exception, however, is alula, a unique hinged flap structure found at the wing base of most hoverflies, as it can be actuated via the third axillary sclerite to actively change the wing camber (similar to the flap mechanism on the modern aircraft) at the wing base during the transient phase (Walker et al 2012).

Although we know much about the effect of active camber and flexion in fixed wings, there are many unsolved questions about their role in flapping wings, especially in context of the unsteady aerodynamics of the flapping wings. Wings flapping at high angles of attack are subject to highly unsteady and three-dimensional (3D) flows (Yu and Sun 2009) making it particularly difficult to delineate the effects of wing flexion. To simplify our study, we therefore used a high-aspect-ratio translating wing with trailing-edge flap to minimize the 3D flow effects observed in flapping or revolving wings and simulate the transient flexion in flapping wings. Many previous studies have used translating 2D wings as a first step toward understanding 3D flows. For example, Dickinson and Gotz (1993) studied the impulsively started translating wing with large aspect ratio in order to investigate the unsteady aerodynamics of flapping wing. A similar experimental setup was used in the studies of wingwake interactions (Lua et al. 2008,2011). Panah and Buchholz (2014) investigated a 2D plunging plate in a water tunnel by varying the plunging amplitude and frequency. Moreover, based on potential flow theory and NS equations, simulations of 2D accelerating wings were performed to study the basic effects of unsteady wing motion (Pulling and Wang 2004; Chen et al. 2010; Xia and Mohseni 2013).

Along these lines, we used a wing model with high aspect ratio which started impulsively from rest to partially simulate the unsteady wing motion of the flapping wing. The trailing edge of this wing was equipped with a hinged flap that could be

actuated independently from the wing movement. Using this apparatus, we investigated how different active flexion kinematics influenced the forces and flows around the translating wing, specifically focusing on the effects of flexion timing and speed.

3.3 Experimental setup and Procedure

The experiment was conducted in an oil tank ($61 \times 61 \times 305cm$, width height length) filled with mineral oil (Kinematic viscosity = 20 cSt at 20^oC, density = $840\, kg/m^3$). A transparent wing model made from plexiglass was installed vertically onto the linear stage through an aluminum frame. To minimize the spanwise flow and free surface effect, another plexiglass plate with a 20-mm-wide slot in the middle was used as an end wall to the wing tip on the top. The bottom wall of the tank was used as the end wall for the other wing tip. The gaps between the wing tips and end walls were between 2 and 4 mm (Fig.3. 1 a).

A six-component force/torque sensor (Nano 17, ATI Ind. Automation, NC, USA SI-25-0.25 calibration) was mounted on the aluminum frame above the end-wall plate and connected to the tip of the wing model. The instantaneous force acting on the wing was measured at a sampling rate of 1000 Hz. We used a planar 2D PIV system (TSI, Inc, Shoreview, MN) to measure the crosswise velocity field at the half-wingspan section. A pulsed Nd:YAG laser illuminated the measured plane which was seeded with air bubbles in mineral oil (average size of 20 to 50 microns; similar methods have been used in Birch and Dickinson 2001 and Cheng et al 2013). A 45^o slanted front reflective mirror was installed underneath the tank to reflect the particle images onto the camera, taking images at ten frames per second and 1024×1024 resolution. To ensure the wing is always in the view of the camera, the camera was attached onto the aluminum frame and allowed to move smoothly along with the wing model using four bearing wheels(Fig.3.1 a).

The wing model had a rectangular planform ($50mm \times 496mm$; aspect-ratio: 9.9) with a thickness of 4 mm (Fig.3.1b). It consisted of two wing sections of same chord

length and separated along the wingspan. The two wing sections were connected by two hinges at both wing tips (plastic tape was used to prevent the flow from going through the gap between the two wing sections). The wing model was bluntly rounded at leading edge and sharply tapered at the trailing edge. A micro digital servo HS-65 (Hitec, Poway, CA) was attached onto the wing section with the leading edge, while the section with trailing edge was driven by the output arm of the servo (the trailing-edge flexion angle is equal to the rotating angle of the servo; Fig.3.1c). We used an Arduino microcontroller to drive the servo which accurately controlled the trailing edge flexion timing and speed. The wing model and camera were controlled to translate along the linear stage using a step motor (Applied Motion Products Inc, CA) with a fine resolution of 1.8^o/Step. The velocity control and data acquisition were accomplished using Q8 Quanser DATA acquisition system (Quanser Consulting Inc, Markham, Canada) and MATLAB/Simulink with WinCon software.

t_{span}	0.2	0.3	0.5	0.7	0.9	1.1
U_{tr}	0.087	0.058	0.035	0.025	0.19	1.16

Table 3.1: Flexion duration versus trailing-edge velocity magnitude due to flexion

In this study, we investigated the effects of timing and speed of flexion with respect to a single wing translation kinematic profile. Specifically, the wing started translating at t = 0 s with the angle between the leading-edge section and translating direction fixed at 40 ± 1^o. After 0.4 s of constant acceleration phase, the wing reached its final velocity of 0.1 m/s corresponding to a Reynolds number of 250. Wing translation lasted for 4 s, and the total travel distance was 7.6 chords length. The repeatability of the wing translation kinematics was confirmed using a high-speed camera (Fastec Trouble Shooter, FASTEC IMAGING CORPORATION, CA), measuring the distance wing had traveled in multiple runs. Wing flexion angle was designed as a linear function of time and eventually reached a fixed value of 40^o (Fig.3.1c, d). The wing started deflecting at t= t_{delay} which represented the time delay between the onset of wing translation and flexion. The time duration required for flexion was denoted by

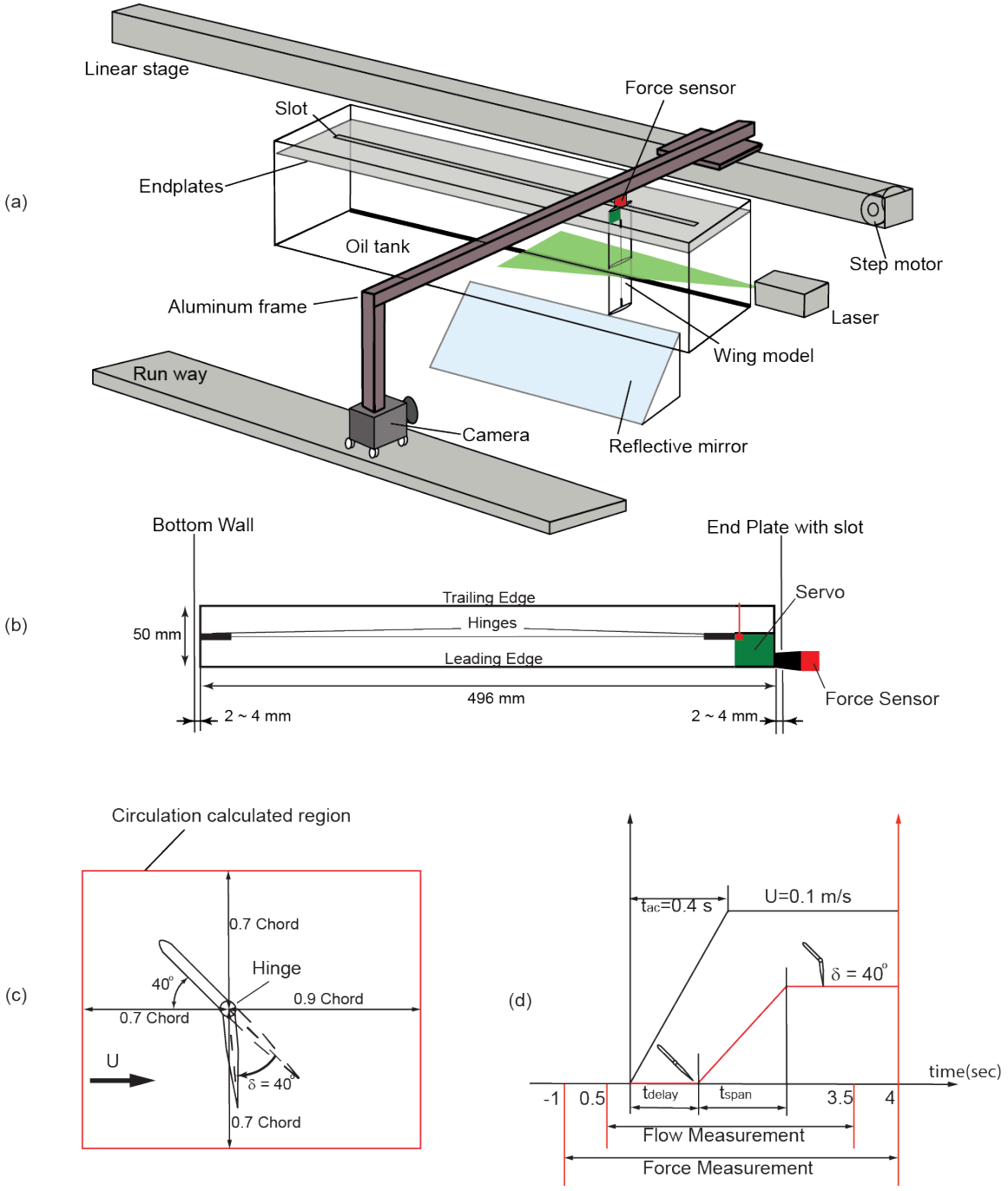

Figure 3.1: Schematics of the experimental setup and wing kinematics. (a) Experimental setup.(b) Wing model. Two wing sections of same chord length were connected by two hinges. (c) Wing cross section with bluntly rounded leading edge and sharply taped trailing edge. A red rectangular region was used to calculate the circulation around the wing. (d) Wing starts to translate at t = 0 s and accelerates to the final velocity of 0.1m/s within 0.4 s. Wing starts the flap deflection at $t = t_{delay}$ s and deflect to a fixed angle of 40^o within t_{span} s; t_{delay} controls the deflection timing and t_{span} controls the deflection speed.

t_{span}(Fig.3.1 d). Thus by simply varying t_{delay} and t_{span}, we could systematically vary both the timing and speed of the flexion. We explored a total of 105 study cases which included 15 sets of flexion timings combined with 7 sets of flexion speeds (t_{delay} varied from -0.4 s to 1.4 s and t_{span} varied from 0.2 s to 1.3 s. Since the flexion angle is fixed at 40^o, the flexion speed was inversely related to the t_{span} . The corresponding trailing edge velocities U_{tr} due to flexion are given by Table.3.1). We measured forces for all the study cases, but conducted PIV measurements on a selected group of 30 cases. Three runs of experiments were performed for each force and flow measurement to provide ensemble-averaged data. The force measurement started from t = 1 s to t = 4 s. The flow measurement started from t = 0.5 s to t = 3.5 s. Between two successive runs, there was 23-min waiting time which was verified by both flow and force measurements to be sufficiently long to avoid noticeable wake effect. In fact, an approximate 3-min waiting time was also used in a similar study (Lua et al 2011).

The measured force was low-pass-filtered with a cutoff frequency of 170 Hz. The inertia force due to the active trailing-edge flexion was measured in the air (without translation), and the inertia force due to wing translation was estimated based on the measured wing translating kinematics from the high-speed camera. Finally, the aerodynamic force was obtained by subtracting all the inertial force components from the total measured force. An interrogation window size of 32×32 pixels with a 50% overlap was utilized to process the particle images. With a calibration factor of 145.5 m per pixels, the spatial resolution then was $4.65mm \times 4.65mm$ (about 0.093 chord length). The uncertainty of the vorticity field only depended on the uncertainty of the 2D PIV measurement and was not affected by the small relative motion between camera and wing model (the relative motion only introduced a uniform displacement field, and the operation of curl will remove this effect). Collectively, we estimated an uncertainty of 3% for the force measurements and 4% for the measurements of vorticity.

3.4 Results and Discussion

We first analyze the force trace and flow pattern of the flat wing as a reference case. Similar to the flow around a bluff body, the flow around flat wing can be described by a starting vortex shed in the beginning followed by alternative vortices developing and shedding afterward (Dickinson and Gotz 1993). In supplementary material 1, Q method (Jeong and Hussain 1995) was implemented to identify the vortex structure in the flat wing with the contour of Q = 8, indicating the boundary of vortices (different Q values were tested, and it was found that the result with Q = 8 can best present the flow feature in flat wing). In the supplementary material 1, the green loop indicates the boundary of leading-edge vortex (LEV) and its corresponding free vortex; the red loop presents the boundary of trailing-edge vortex (TEV) and its corresponding starting vortex (SV). The circulation magnitude was calculated on the red and green loops accordingly by integrating the vorticity inside the loops. Fig.3.2 gives the plots of circulation magnitude on the vortices. Before the shedding of the vortex (TEV or LEV), vorticity is continuously generated and accumulating, leading to a continuous increase in circulation magnitude. After the shedding, the circulation magnitude of vortex stops growing. Notably, the circulation magnitude of TEV/SV stops growing at t = 0.5 s, and then its value stays at around $0.002m^2/s$. The circulation magnitude of LEV, however, presents a more complex behavior with its value that stops growing at t = 1.1 s and then followed by a significant fluctuation. According to supplementary material 1, the LEV starts to shed at 1.1 s and the just shed free vortex reconnects to the leading edge at 1.4 s and finally shed completely at 1.5 s, leading to the fluctuation on the circulation magnitude of LEV. Consequently, by studying the development of circulation magnitude of vortices, we found that the TEV began to shed at t = 0.5 s and forming a SV, while the first LEV began to shed at t = 1.1 s.

As will be shown later, the effect of active flexion depends strongly on its timing relative to SV and LEV shedding in flat wing. Hence, we chose the timing of the

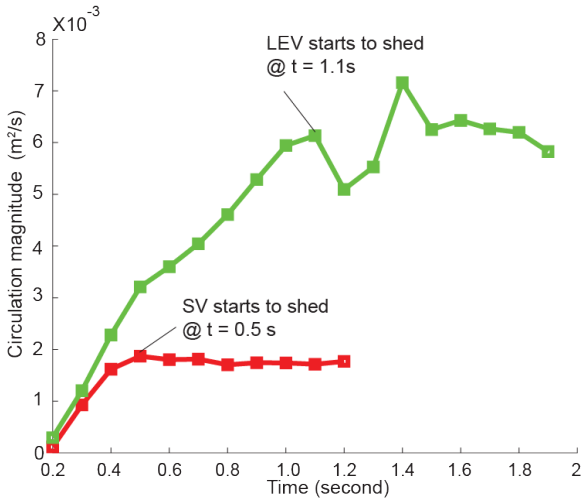

Figure 3.2: Circulation magnitude of leading edge vortex and its corresponding free vortex as well as the trailing edge vortex and its corresponding stating vortex during the onset of wing translation. Trailing edge vortex stops growing and begins to shed at t= 0.5 s (red curve); Leading edge vortex stops growing and starts to shed at t 1.1 s (green curve).

SV shedding (T = 0.5 s) as the characteristic time length to normalize t_{delay}. The variables t and t_{span} were also normalized by T = 0.5 s which is the time for the wing to travel one chord length at the final velocity of 0.1 m/s. These three normalized variables were denoted by superscript * (Eqn 5.1). As a result, ${t_{delay}}^* = 1$ indicates that wing starts to deflect at the moment of SV shedding; and ${t_{delay}}^*= 2.2$ indicates that wing starts to deflect at the moment of the first LEV shedding. It is also worth noting that, because the deflection angle is fixed, ${t_{span}}^*$ actually represents the ratio between the wing translation velocity (0.1m/s) and the trailing edge velocity due to flexion. In addition, the aerodynamic forces were normalized by using the final velocity of wing translation(U_o=0.1 m/s) and chord length on the flat wing (C_o=50 mm) as the characteristic velocity and length (Eqn 5.2).

$$ {t,_{span,delay}}^* = \frac{t,_{span,delay}}{T} \tag{3.1} $$

$$C_{l,d} = \frac{L, D}{\frac{1}{2}\rho {U_o}^2 C_o} \tag{3.2}$$

3.4.1 Instantaneous Force

The instantaneous lift and drag forces for 15 different flexion timings are shown in Figs.3.3 and 4, respectively. The black solid curves represent the force on the flat wing, whereas the colored curves represent the force on the flexed wing with varying flexion speeds (speed increases as ${t_{span}}^*$ decreases).As expected, before the wing flexion (timing of the flexion is indicated by upward black arrow in Figs.3.3,4), all the colored curves overlap with the black ones of the flat wing. However, after the wing flexion, the force evolution is sensitive to both flexion timing and speed.

When ${t_{delay}}^*$ is negative ($-0.8 < {t_{delay}}^* < -0.2$, Fig.3.3a-c), the wing flexes before the onset of translation. Compared with the flat wing, the advanced flexion does not have a significant effect on the time course of the lift except at the initial transients (flexion causing a force oscillation before onset of the wing translation). Note that, the slowest flexion causes a slight increase in lift at onset of wing translation, but the subsequent lift course is mostly unaffected by the flexion speed. There is, however, a significant increase in drag after flexion(Fig.3.4a-c), compared to the flat wing, as the drag peak rises from 2.9 to 5.2 (${t_{delay}}^*$ = - 0.8); and the overall drag on the deflected wing is substantially higher than that of the flat wing in the range of $3 < t* < 8$.

While the wing flexes between the onset of wing translation and the SV shedding ($0 < {t_{delay}}^* < 1.0$, Fig.3.3d-g; Fig.3. 4d-g); active wing flexion lead to significant augmentations on both lift and drag at t*=0.8. In particular, when wing flexes with the highest speed slightly prior to SV shedding (${t_{delay}}^* = 0.4$; ${t_{span}}^* = 0.4$), the lift and drag coefficients reach the maximum value observed in all trails. Compared to the case when the wing flexes before it starts (${t_{delay}}^*$ = - 0.8), both the lift and drag peaks increase by about 54% when ${t_{delay}}^* = 0.4$; ${t_{span}}^* = 0.4$. For the cases of high flexion speeds (${t_{span}}^*$= 0.4, 0.6, 1.0, 1.4), the lift traces after the peak are mostly

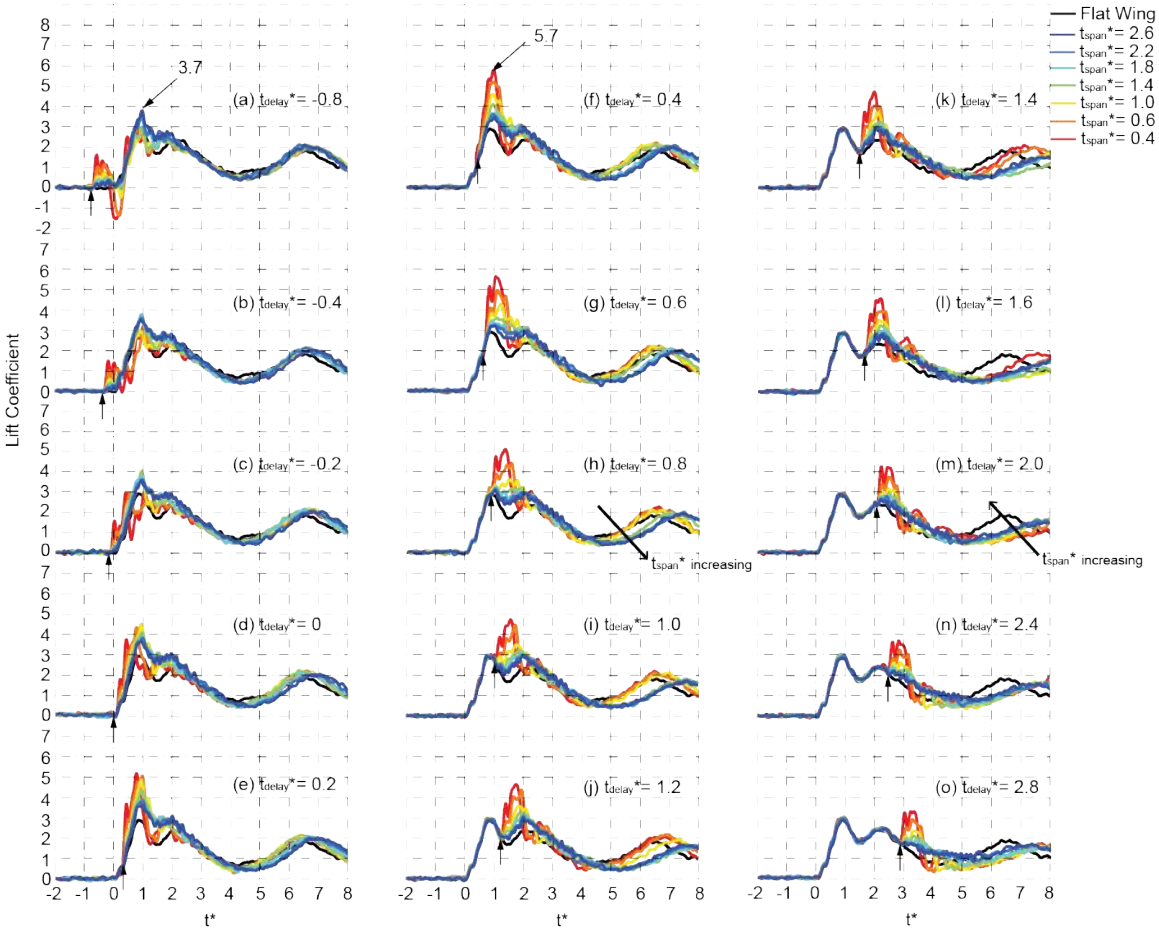

Figure 3.3: Instantaneous lift coefficient versus normalized time; Lift coefficient curves under the same deflection timing are plotted together in the same group (a-o). Black arrows indicate the instant when the wing starts to deflect. Black curves are the lift coefficient on the non-deflected flat wing while the other color coded curves present the lift coefficient on the wing with different deflection speeds.

unaffected and similar to those in Fig.3.3 a-c. As flexion speed decreases (t_{span}*= 1.8, 2.2, 2.6, 3.0), the lift peak in the range of $5 < t* < 8$ is both reduced and delayed.

In Fig.3.3j-m, as the timing of wing flexion approaching the LEV shedding, the force augmentation due to flexion is reduced with the lift courses within $5 < t* < 8$ significantly weakened for the case with high flexion speeds ($t_{span}^* = 0.4, 0.6$) while those with low flexion speed have little changes. Finally, in Fig.3.3n-o, when the wing flexion timing increases and beyond the timing of LEV shedding ($t_{delay}^* > 2.2$), the lift courses within $5 < t* < 8$ start to increase and recover.

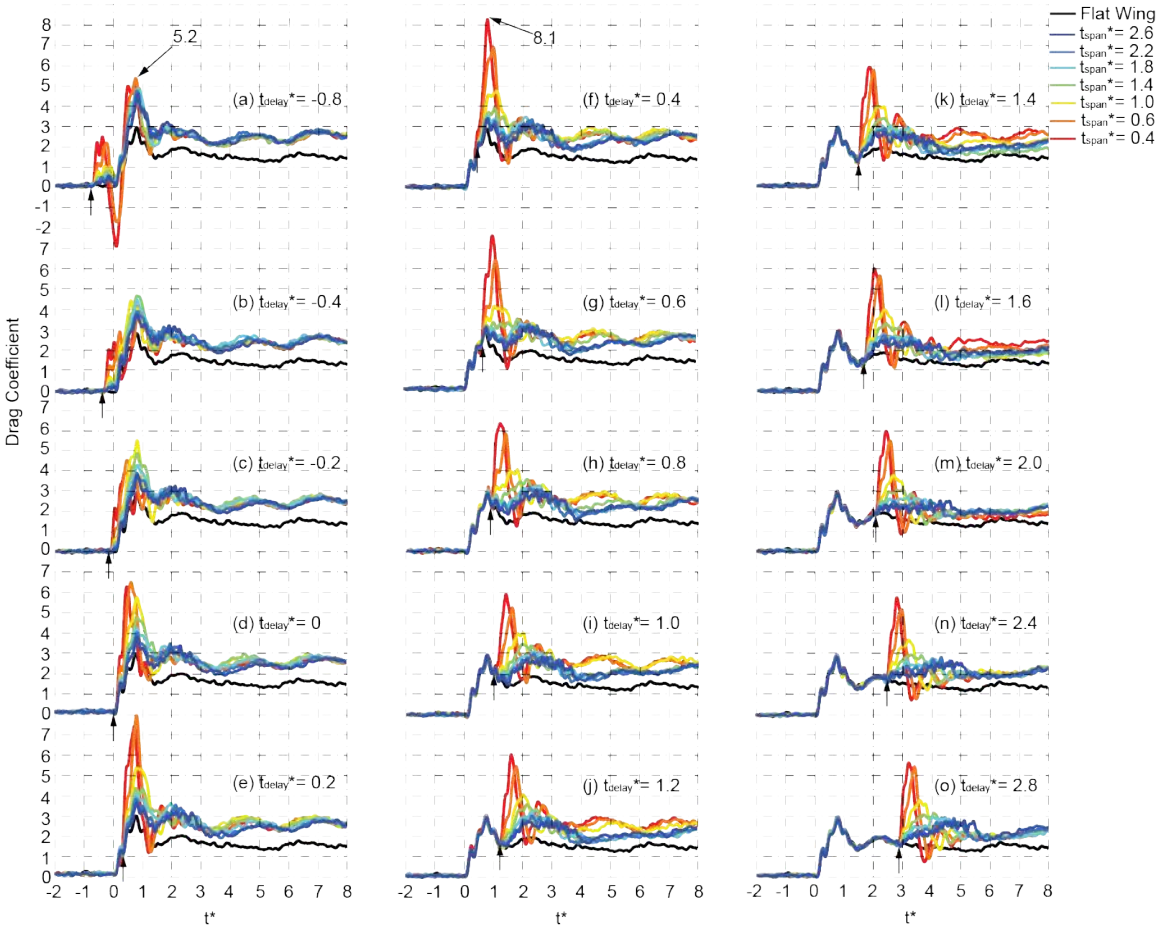

Figure 3.4: Instantaneous drag coefficient versus normalized time.

3.4.2 Average Force

In the last section, we showed how instantaneous force depend on active wing flexion with variable timings and speed. In this section, the effect of active flexion averaged over a specific time interval of interests will be illustrated by looking at the contours of averaged forces as functions of flexion timing ($t_{delay}{}^*$) and speed ($t_{span}{}^*$).

The difference of average forces between flexed and flat wings, over an interval of $\Delta t^* = 3.0$ after onset of wing flexion, is plotted in Fig.3.5 a and b. Note that, $\Delta t^* = 3.0$ corresponds to the maximum value of deflection duration ($t_{span}{}^*$). Conspicuously, lift is significantly increased (over 0.55) when the wing flexes prior to the shedding of SV ($0.2 < t_{delay}{}^* < 1$) with high speed ($0.4 < t_{span}{}^* < 1.4$). However,

early or late flexion ($t_{delay}{}^{*} < 1$or $t_{delay}{}^{*} > 2$ results in limited increase of average lift coefficient (less than 0.2) but considerable increase of averaged drag coefficient (larger than 0.6). Also in these regions, higher flexion speeds lead to a lower averaged lift increase; by contrast, when flexion occurs before the shedding of SV ($0.2 < t_{delay}{}^{*} < 1$), greater speed of flexion leads to higher average lift increase (Fig.3.5 a). On the other hand, drag increases with higher flexion speed for most cases investigated (Fig.3.5 b).

In addition, contour plots of the average lift, drag coefficient (over $-0.8 < t^{*} < 8$) and average lift-drag ratio are shown in Fig.3.5 c- e (In Fig.3.5 c, d, the lift and drag coefficients on flat wing were set as the lowest value in the color bar, and average liftdrag ratio on flat wing was set as the highest value in color bar in Fig.3.5 e, therefore, the average force on flexed wing can be compared with the force on the flat wing quantitatively). Similar to the average lift over $\triangle$t* = 3.0 immediately after the flexion, in the region where the wing flexes prior to the shedding of SV with high speed, the average lift reaches relatively high values (about 1.55). However, the average lift decreases significantly when flexion is delayed (in the region highlighted by the green loop, Fig.3.5c), with a minimum value about 1.28. The results also show that the average drag tends to be high when wing flexes before the shedding of SV, and reaches its maximum around the point $t_{delay}{}^{*} = 0.4$ and $t_{span}{}^{*} = 1.0$ (Fig.3.5d). The average liftdrag ratio almost monotonically increases with increasing $t_{delay}{}^{*}$ and $t_{span}{}^{*}$, where slower and delayed flexion results in higher liftdrag ratio and the value of average liftdrag ratio of flexed wing is always lower than that of the flat wing (Fig.3.5e) regardless of the timing and speed of the flexion applied.

The lift-drag ratio results presented above can be at least partially explained from a geometric point of view (Fig.3.5f). Specifically, for a rigid flat wing translating at a high angle of attack, the net force vector is approximately normal to the wing surface because the viscous force is negligible compared to the pressure force (Sane 2003). Therefore, the liftdrag ratio is simply proportional to cotangent of angle of attack, which decreases with the angle of attack. In the current experiments, the active flexion increased the effective angle of attack, thus resulting in a lower liftdrag ratio

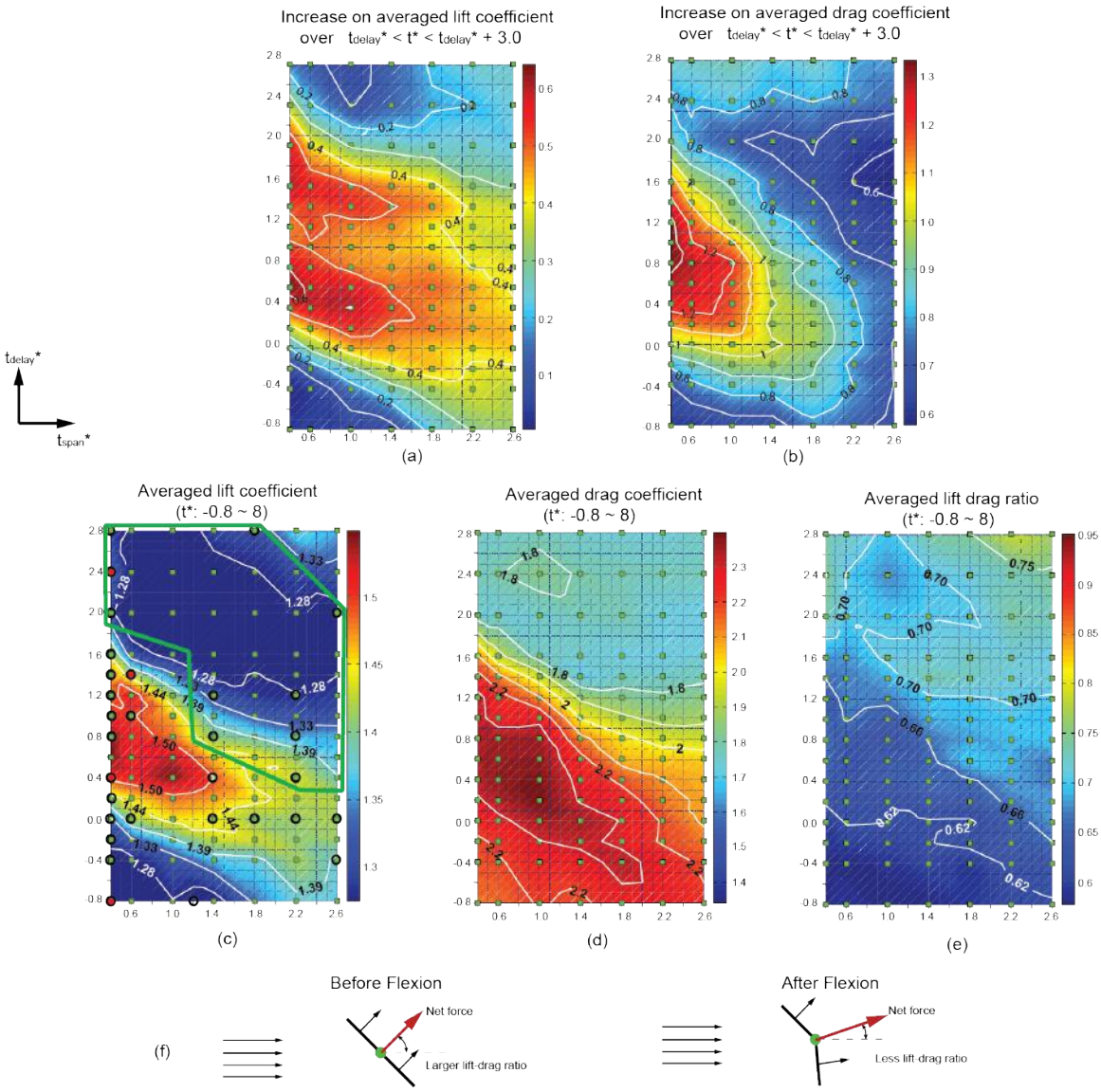

Figure 3.5: Contour plots of average force as functions of $t_{delay}{}^*$ and $t_{span}{}^*$. Green squares present the sampling points for force measurement. (a) Increase on average lift coefficient over $t_{delay}{}^* < t^* < t_{delay}{}^* + 3.0$. (b) Increase on average drag coefficient $t_{delay}{}^* < t^* < t_{delay}{}^* + 3.0$. (c) Average lift coefficient over $-0.8 < t^* < 8$. Black circles present the sampling points for flow measurement. (d) Average drag coefficient over $-0.8 < t^* < 8$. (e) Average lift-drag ratio over $-0.8 < t^* < 8$. (f) Geometry effect of flap deflection on the lift-drag ratio.

if it occurs earlier or faster. Therefore, our results indicate that although active wing flexion is able to substantially improve both transient and averaged lift production, it is undesirable for improving liftdrag ratios due to much higher drag production. In

the next section, we will show that the contour plots of the average lift introduced in this section can be categorized into four different regions that are closely related to the flow patterns captured from PIV experiments.

3.4.3 Flow patterns and Circulation

We conducted flow measurements on selected flexion cases (black circles in Fig.3.5c) and observed four types of flow patterns (all the flow measurement results are shown in supplementary material 2). These flow patterns show strong correlation with four different regions (I, II, III and IV) in the contour plots of average lift.

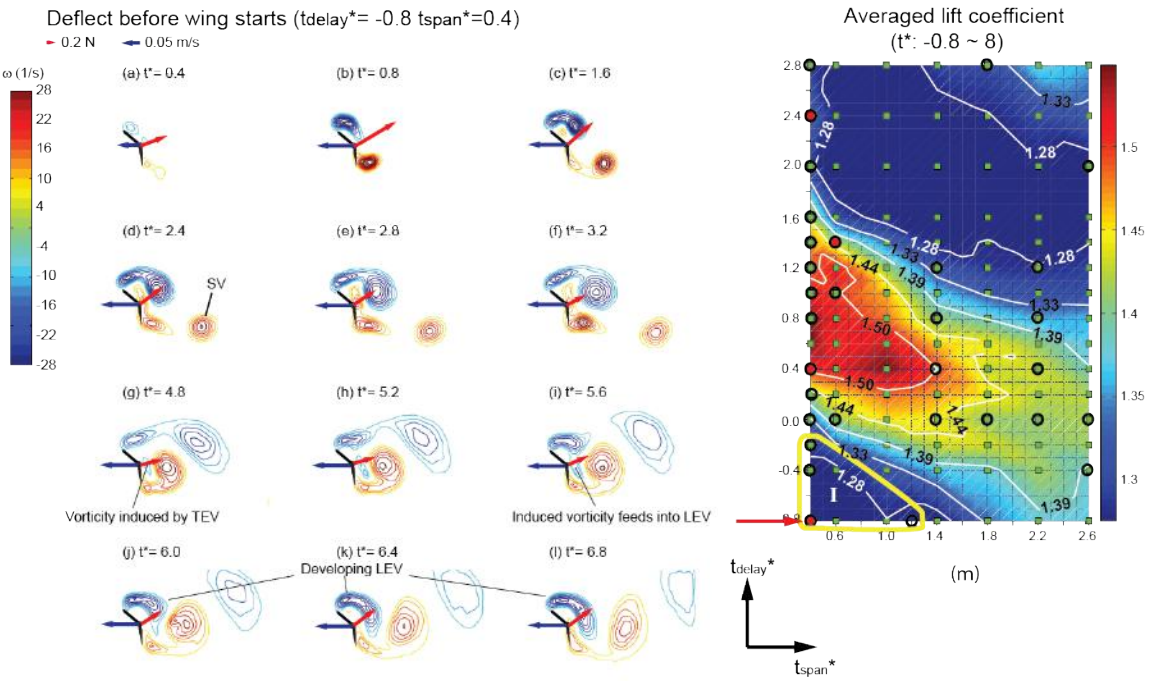

Figure 3.6: A typical flow in region I at $t_{delay}{}^{*} = -0.8$ and $t_{span}{}^{*} = 0.4$ where the wing deflects before the wing starts with a high deflection speed. (a-l) Contour plots of vorticity. Black parts present wings cross section; Red arrows give the instantaneous net forces; Blue arrows show the translational velocity on the wing. (g) Negative vorticity was induced closed to hinge. (i) Induced negative vorticity feeds into LEV. (j-l) LEV is promoted by feeding the induced negative vorticity into LEV. (m) Region I highlighted by yellow loop. Red circle and arrow indicate where current contour plots of vorticity were measured.

Fig.3.6a-l shows the typical flow pattern in the region I (highlighted by the yellow loop, Fig.3.6 m), which corresponds to wing flexion prior to the translation with high flexion speed ${t_{span}}^* < 1.0$), and results in a low averaged lift. In this region, although the fast flexion disturbed the flow, its effect decayed very quickly before the onset of wing translation, and results in a low averaged lift. In this region, although the fast flexion disturbed the flow, its effect decayed very quickly before the onset of wing translation, and hence the wing may be considered to have started with a preset flexion angle (the flow in this case is very similar to the flow on the pre-flexed wing; the similarity can be seen later in the circulation plots in Fig.3.10). It can be seen that SV begins to shed at t* = 1, and then the flow is dominated by the alternate vortex shedding. Interestingly, the trailing-edge vortex with positive vorticity induces a small amount of negative vorticity close to the flexion hinge which then feeds into the leading-edge vortex and enhances its strength in its future development (Fig.3.6 g-l).

Region II (enclosed by a red loop, Fig.3.7 m) corresponds to high average lift coefficients, where the wing flexes after the onset of wing translation but before the SV shedding, a typical flow pattern of which is shown in Fig.3.7 a-l. The result suggests that the trailing-edge vorticity due to wing flexion feeds into the SV and considerably enhances its strength (Fig.3.7b-d, It will also be confirmed later in Fig.3.12 where the circulation of SV was calculated) so as the strength of LEV because the overall circulation should keep zero (Wu 1981). Similarly, the induced negative vorticity next to the hinge also feeds into the LEV in this region.

In the region III (enclosed by blue loop,Fig.3.8 m), the wing flexes after the SV shedding but before the LEV shedding($1.0 < {t_{delay}}^* < 2.0$) with high flexion speed(${t_{span}}^* < 0.8$). In this region, instead of a single trailing-edge vortex (SV) shedding into the wake, an additional trailing-edge vortex was created due to wing flexion, and two distinct vortices were observed(Fig.3.8 f). It is worth noting that this flow pattern depends on both the flexion timing (${t_{delay}}^*$) and flexion speed (${t_{span}}^*$). For example, with a slower flexion speed of ${t_{span}}^* = 1.4$, no secondary trailing-edge vortex can be observed

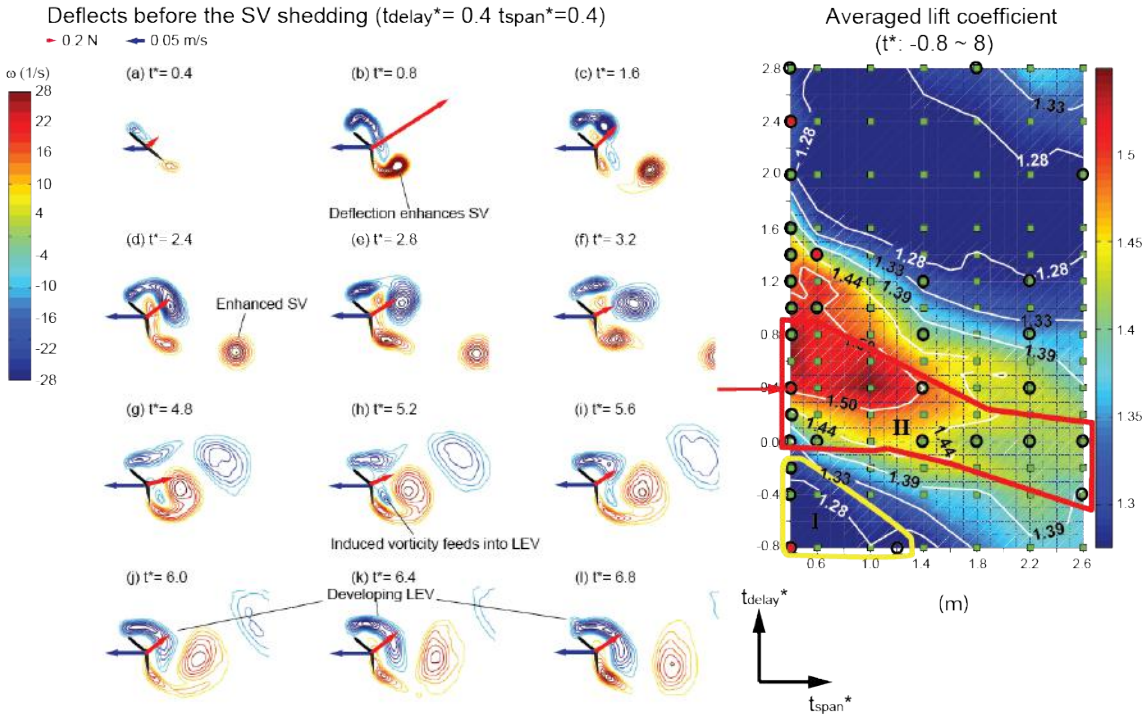

Figure 3.7: A typical flow in region II at $t_{delay}{}^{*} = 0.4$ and $t_{span}{}^{*} = 0.4$ (b) SV was enhanced by flap deflection and the net force had a significant increase. (h) Induced negative vorticity was feed into the LEV. (m) Region II with high average lift, highlighted by red loop.

despite that the flexion timing is in an appropriate range ($t_{delay}{}^{*}$=1.2). As a result, the flow pattern with two successive trailing-edge vortices is only restricted in the limited region III inside the blue loop.

Finally, region IV corresponds to the lowest average lift (highlighted by green loop, Fig.3.9 m), and its flow pattern is showed in Fig.3.9a-l. In this region, the flap flexes during or slightly after the LEV shedding, causing simultaneous shedding of the TEV and LEV (Fig.3.9e-h).As a result, these two vortices with negative and positive vorticity undergo strong interaction with each other. The LEV is therefore substantially affected and reduces into a large amount of negative vortical flow connected to the leading edge and unable to shed completely for a long period of time (Fig.3.9i-l; the vortical flow connects to the leading edge until t*=7.2 while in region III the vortical flow connects to the leading edge until t*=4.4). Furthermore, the formation of next

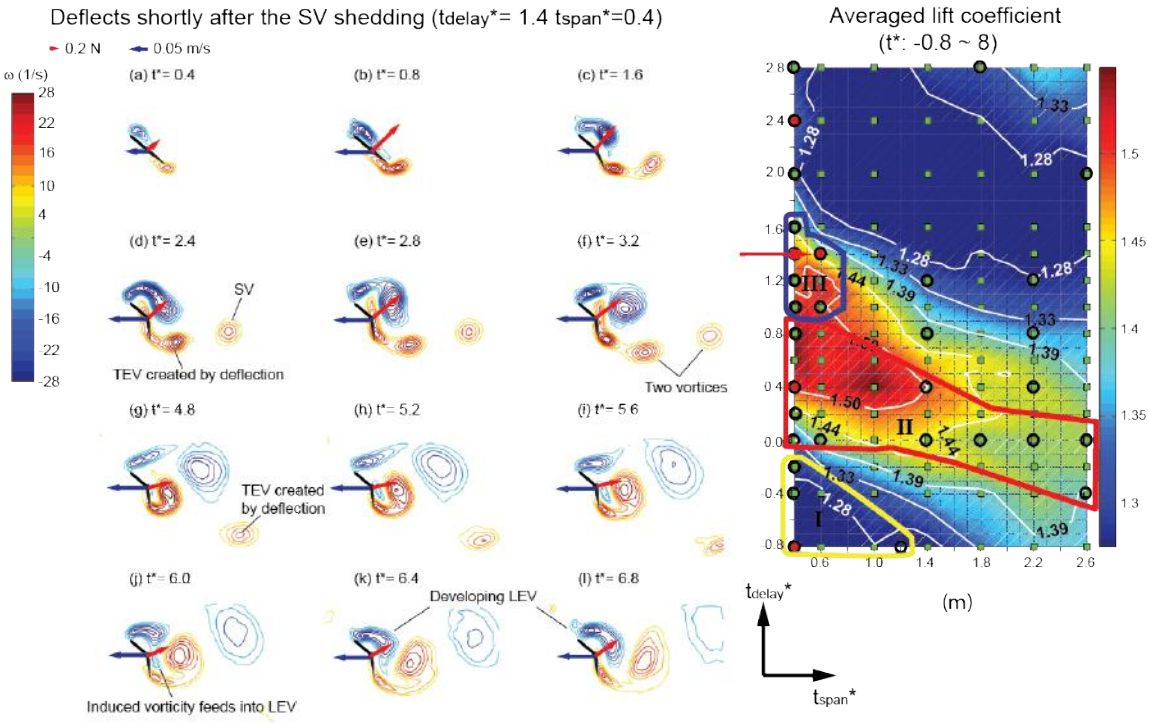

Figure 3.8: A typical flow in region III at $t_{delay}{}^{*} = 1.4$and $t_{delay}{}^{*} = 0.8$ (d) Another TEV was created by deflection beside SV. (j) Induced negative vorticity feeds into LEV.

LEV is significantly affected and no considerable LEV is produced on the wing in a long period of time ($t* = 4.8$ 6.4), possibly leading to the low lift in region IV.

To further demonstrate the differences of the flow patterns in those four regions and confirm the categorized flow patterns, the circulations on all the selected flexion cases were calculated within a rectangular region surrounding the wing ($1.4C \times 1.6C$ in Fig.3.1 (c)) (the calculated region was large enough to cover all the major flow features close to the wing). We also calculated the circulation values of the flat wing and pre-flexed wing as the references. These results are summarized in Fig.3.10

As expected, the circulation plots exhibit four different types of behavior. In region I where the flap flexes before the wing starts with high flexion speed (Fig.3.10a), tthe circulation curves on those four flow measurement points (black circles in yellow loop in Fig.3.9m) show very little difference and overlap with the circulation on the pre-

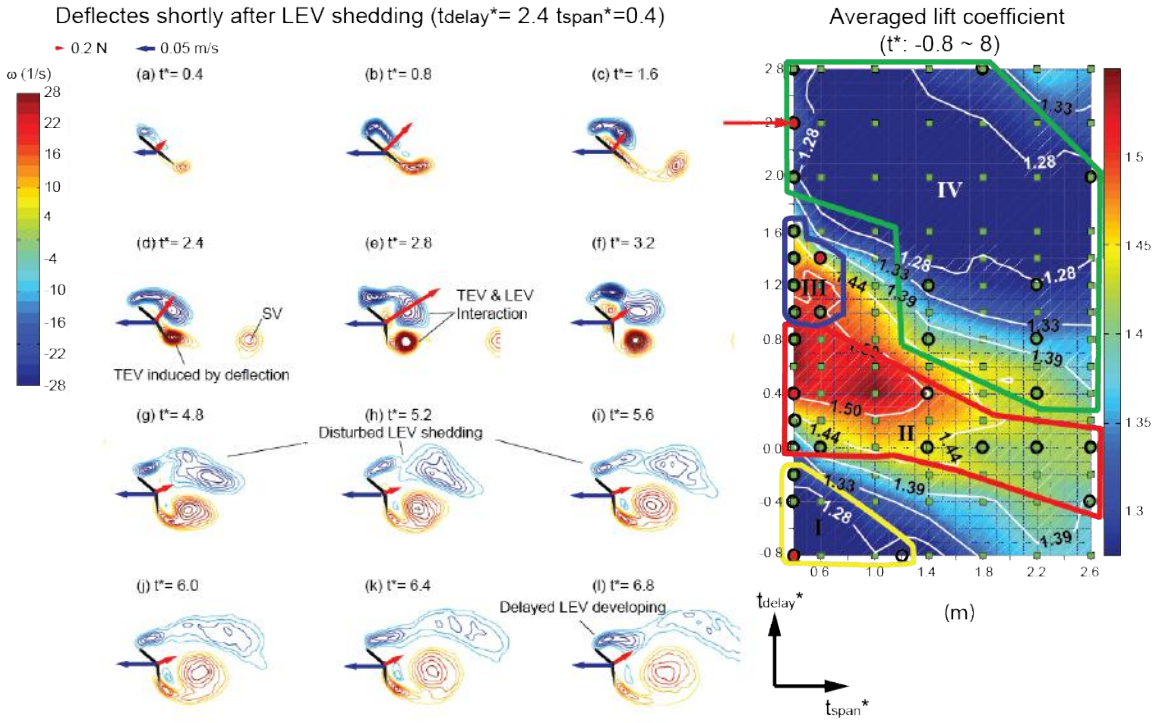

Figure 3.9: A typical flow in region IV at $t_{delay}{}^* = 2.4$ and $t_{span}{}^* = 0.4$ (e) TEV created by deflection interacted with LEV pronouncedly. (g-i) LEV shedding was disturbed, delaying the generation of next LEV. (m) Region IV with significantly reduced averaged lift, highlighted by green loop.

flexed wing. This is also consistent with our previous observation that the flow in region I is similar to the flow on the pre-flexed wing. In Fig.3.10b, the circulations on the measured points in region II are plotted. In the range of $2 < t* < 4$, the flow close to the wing is dominated by intense negative vortical flow which can be inferred to be the strong leading-edge vortex due to the shedding of enhanced SVs in Fig.3.7 (the overall circulation of the entire flow is zero (Wu 1981)). Fig.3.10c shows the circulation curves in region III where the flexion occurs between the SV and LEV shedding. The circulation in this region experiences a secondary drop in the range of $2 < t* < 4$ due to the shedding of second TEV (see Fig.3.8). Finally, Fig.3.10d presents the circulation curves in the region IV. Here, the overlapped region of circulation curves between the flexed and flat wing cases extends, and the secondary

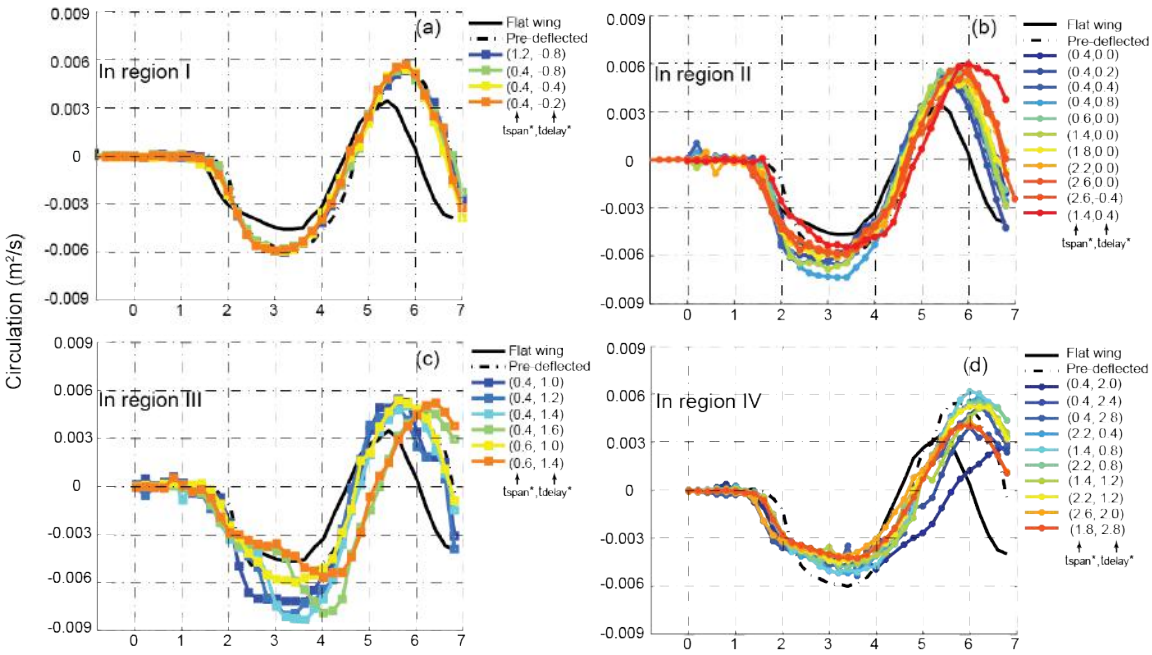

Figure 3.10: Circulation versus normalized time. Circulation curves in the same region have similar behavior. (a) Circulation curves in region I overlap with each other and are closed to the circulation on the pre-deflected wing (black dash curve). (b) Circulation curves in region II have pronounced negative circulation in the range of $2 < t^* < 4$. (c) Circulation curves in region III have abrupt drops in the range of $2 < t^* < 4$. (d) Circulation curves in region IV experience mild increase over $4 < t^* < 6$ and limited decrease over $6 < t^* < 7$.

circulation drop in region III is not observed in region IV. Instead, owing to the strong interaction between the TEV and LEV (Fig.3.9), circulation mildly increases in the range of $4 < t* < 6$ and decreases in the range of $6 < t* < 7$. In particular, for the case of ${t_{delay}}^* = 2.0$ ${t_{span}}^* = 0.4$ (the blue curve in Fig.3.10d) where the flexion occurs close to the LEV shedding, the circulation has the slowest increase with no decrease observed afterward. In summary, the comparison of the circulations from the flow measurement further confirms the categorization of the four types of flow patterns.

3.4.4 Vortex strength and lift peak

In the beginning of this section, the flow on the flat wing was analyzed by calculating the circulation magnitude of LEV and TEV/SV to determine the timing of vortex shedding. Here, to investigate the wing flexion effect on the vortices, the same method of circulation calculation was applied to study the behavior of LEV and TEV/SV under different wing flexion timings. Fig.3.11a and b give the plots of circulation magnitude of the LEV and its corresponding shedded free vortex on the selected cases with the fastest flexion speed but different flexion timings. As compared to the flat wing, wing flexion enhances the LEV if wing flexion happens before the SV shedding (${t_{delay}}^* < 1.0$, Fig.3.11a)However, if the wing flexion happens after the SV shedding or during the LEV shedding (${t_{delay}}^* > 1.0$, Fig.3.11b), the strength of LEV and its corresponding free vortex is greatly disturbed and weakened. The circulation magnitude of the TEV/SV is plotted in Fig.3.11c and d. Compared to the circulation of LEV, the circulation of TEV/SV is more sensitive to the flexion timing change. In general, wing flexion cannot affect SV if SV has already shed from the wing(${t_{delay}}^* > 1.0$, Fig.3.11 d) and the circulation of SV is close to the circulation of SV on the flat wing (black curve). In Fig.3.11 c,when $0 < {t_{delay}}^* < 1.0$, the circulations of the SVs have the largest values. Especially, when ${t_{delay}}^* = 0.4$, the SV strength is maximized as the vorticity due to flexion is able to completely feed into the starting vortex and the highest lift force was observed in the same region. In fact, correlation between the lift production and starting vortex shedding has been previously pointed out by Wagner (1925). Here in Fig.3.12, the relation between the SV strength and lift force is explored by calculating the normalized circulation of SVs and comparing them with the maximum lift coefficient in the range of $-2 < t^* < 1$ (where the SV shedding takes effect) on the selected cases with the maximum flexion speed but varying flexion timings ($-0.8 < {t_{delay}}^* < 2.8$;${t_{span}}^* = 0.4$). The circulation of SVs was calculated at $t^* = 1.8$ where the wing has translated for 1.44 chord length and the SVs have already completely shed from the wing. Finally, the calculated

circulation value is normalized by the circulation of SV on the flat wing at $t^* = 1.8$. The results indicate that the circulation of the starting vortex (black curve) and the maximum lift coefficient (red curve) have strong correlation as they varying with the flexion timing. Both the starting vortex circulation and lift peak reached high values in the range of $0 < {t_{delay}}^* < 0.4$.The lift peak reached its maximum of 5.7 at ${t_{delay}}^* = 0.4$ when the SV is the strongest which is reasonable because a strong SV leads to a strong negative vortical flow around the wing to keep a zero circulation on the entire flow and therefore might introduce a strong circulatory lift force. When ${t_{delay}}^* > 1.0$, the vorticity due to flexion lags behind the SV, and the normalized circulation drops to about 1 (the strength of SV in the flat wing), while the lift peak remains unaffected by the flexion and staying around 2.9 (At ${t_{delay}}^* = 1.0$, the normalized circulation of SV drops sharply to about 0.5. This is because the trailing edge vortex due to wing flexion and SV are so close, thereby introducing a strong interaction between two vortices and finally reducing the strength of SV).

Nonetheless, here we only discussed the lift augmentation due to SV shedding. In fact, in addition to the SV, the added mass effect and other flow feature (like LEV) would also affect the lift generation (Xia and Mohseni 2013). At a low angle of attack of 15^o, Pitt-Ford and Babinsky (2013) studied a translating flat plate which accelerated from the rest by using potential flow theory with the trajectories and strength of vortices measured through PIV as inputs. It was found that the bound circulation derived from Kelvins circulation theorem provides the best match between modeling and flow measurements during the onset of wing translation. The lift force was finally estimated from superimposing Wagner lift and the non-circulatory force and provided a good prediction as comparing with the measured force. However, the same method cannot be applied to current work where re-attached flow assumption already failed at high angle of attack. Therefore, to fully understand and explain the lift generation on the dynamic flexing wings, analysis on the added mass effect as well as the time resolved overall flow features are needed in the future work.

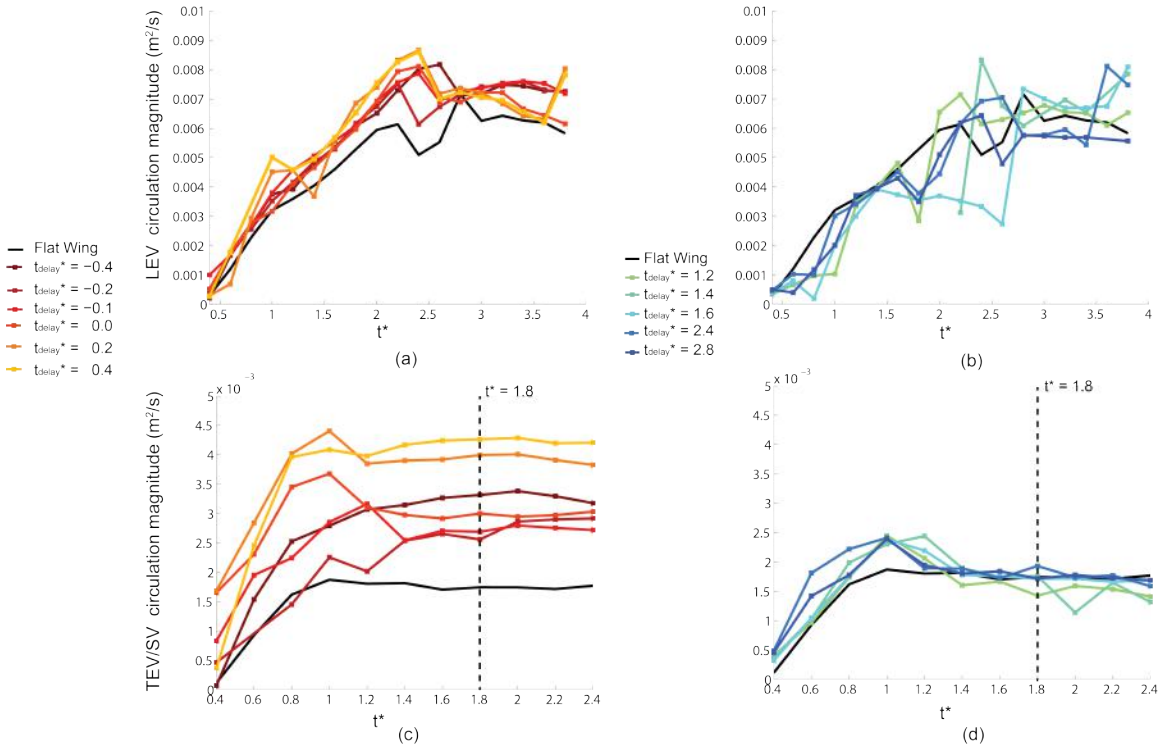

Figure 3.11: Circulation magnitude of vortices on the deflected wings with the highest flexion speed ($t_{span}{}^* = 0.4$) but different flexion timings ($-1 < t_{delay}{}^* < 2.8$)) versus normalized time. (a), (c) Circulation magnitude of LEVs/its corresponding free vortices and TEVs/SVs when wing flexion happens before SV shedding (b), (d) Circulation magnitude of vortices when wing flexion happens after SV shedding

3.5 Concluding remarks

In this paper, the effects of timing and speed of active wing flexion were studied systematically using force and DPIV measurements. The results show that significant improvement on force performance can be achieved by a proper design of wing flexion kinematics relative to the vortex shedding events. In particular, when the wing flexes slightly before the SV shedding with relatively fast speed, the wing produces the maximum lift. However, if the wing flexes during or slightly after the LEV shedding, the lift is substantially reduced and close to that of the flat wing.

It is also shown that by flexing the wing within a certain range of timing at moderate speed, the vortex shedding on the wing changes dramatically and leads to

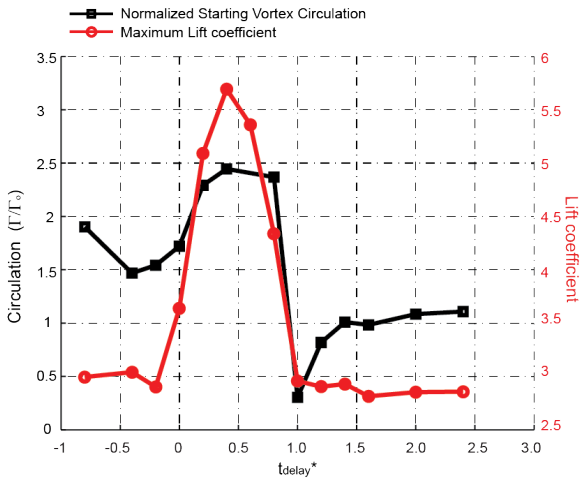

Figure 3.12: Comparison between starting vortex strength (Normalized by circulation of SV in flat wing) and its corresponding maximum lift coefficient (in the range of $-2 < t^* < 1$) for the cases with highest deflection speed (${t_{span}}^* = 0.4$) but different deflection timings ($-1 < {t_{delay}}^* < 2.8$).

four different patterns which can be directly related to four regions in the average lift contour plot (Fig.3.12). First, when the wing flexes before SV shedding, SV is enhanced by the flexion and a large lift force is observed. Especially, the highest instantaneous lift is produced when the strength of SV reaches the highest value. Second, when the wing flexes between the shedding of SV and LEV, a second TEV is shed in addition to the SV and a moderate average lift is observed. Third, when the wing flexes during or slightly after LEV shedding, it affects the shedding of LEV and delays its development, resulting in a low average lift due to the reduced LEV strength. Fourth, when the wing flexes before the onset of translation at a rapid rate, a low average lift is observed as the force and flow structures are similar to those of the pre-flexed wing.Johansson et al. 2008 studied Pallas long-tongued bats in a wind tunnel under different free stream velocities. Strikingly, Johansson observed a distinctive vortex pattern in the wake of Pallas long-tongued bats flying in a wind tunnel, which contained two consecutive TEVs at a low free stream velocity of 2 m/s. In the current study, the same flow phenomenon is found in the region III (Fig.3.13) where both relative high lift (around 1.5) and liftdrag ratio (around 0.7)

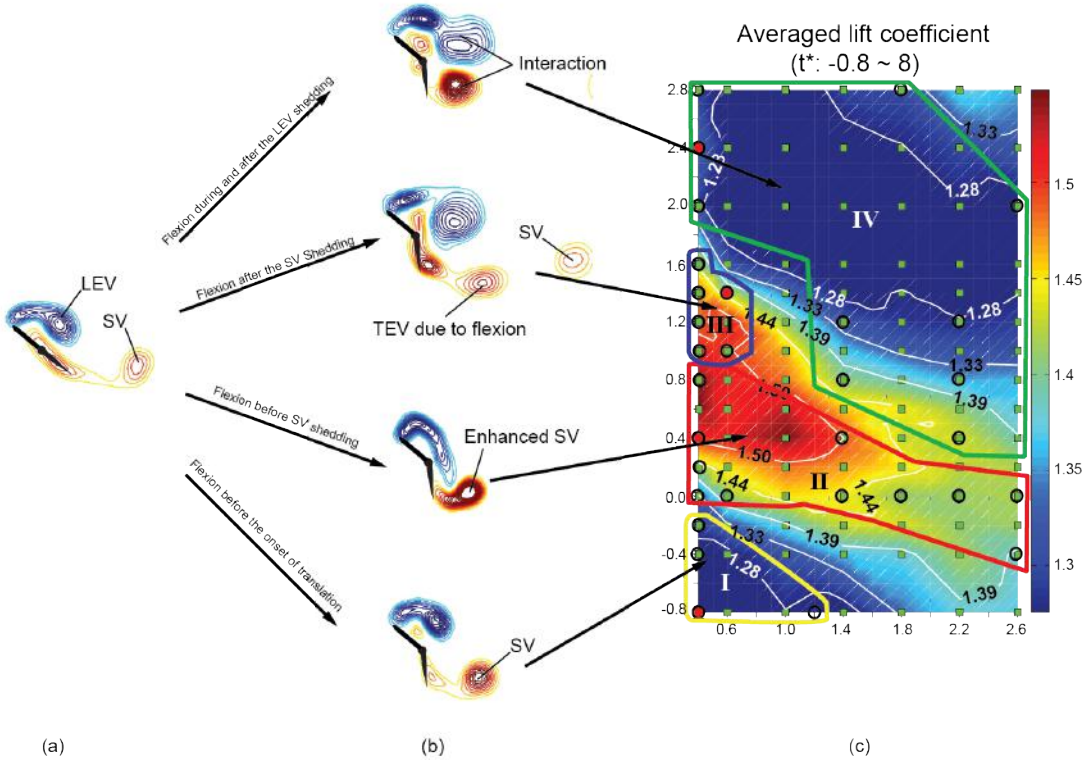

Figure 3.13: A summary of active flexion effects on the flow and lift force. (a) Flow on non-deflected flat wing is simply dominated by a starting vortex in the beginning and alternative vortices shedding afterward. (b) By adjust the active flexion timing respected to the timings of vortices shedding (with moderate flexion speed) four types of flow pattern can be produced (c) Four average lift regions can be closely related to the four different flow patterns.

can be achieved, implying the slow flying bat might have optimized lift performance and efficiency by producing a two consecutive TEVs structure in its wake.

To extend our results to real flapping-wing case, the pronounced wingwake interaction during the stroke reversal (Lua et al. 2011) must be taken into account along with the effect of varying angles of attack throughout the stroke. Furthermore, in 3D flapping wings, because the tip and root vortices may play a critical role in defining the flow structure (Cheng et al 2014; Liu et al 2013), the study of active wing morphing may do well to consider both the 3D and unsteady effects.

4. CONVENTIONAL FLOW VISUALIZATIONS ON MECHANICAL FLAPPERS

4.1 An Application of Smoke Wire Visualization on a Hovering Insect Wing

Published in Journal of Visualization 2013 (First Author: Yun Liu)

4.1.1 Introduction

Insects are able to achieve a highly stable but maneuverable flight due to their distinct form of locomotion (Fry et al. 2003; Hedrick et al. 2009). They flap their wings back and forth at large angle of attack and create augmented lift. In recent decades, the smoke wire visualization was wildly used in studying the aerodynamics of insect flight (Ellington et al 1996; Willmott et al. 1997; Nguyen et al. 2009), as it provides direct and qualitative flow information around the insects and flapper models. Conventionally, the smoke wire visualization is used in wind tunnels which provide uniform and low turbulent free streams. Under this restriction, all the previous experiments of smoke wire visualization on flapping wings were performed in wind tunnels with nonzero free stream velocity which however could not provide an ideal hovering flight condition. In this paper we introduce and experiment a new smoke visualization technique on hovering insect wings.

4.1.2 Experimental Method

Hovering insects and hummingbirds create significant downwash flow (Rayner 1979); therefore, by placing the smoke wire close to the leading edge of the wing, we expect the downwash to drag the smoke particles into the wake and then visualize the flow. Based on this method, we tested a pair of Cicada wings driven by a robotic

insect model using four-bar mechanism (Fig. 1) (details see Hu et al. 2011). In the experiment, the smoke was generated using paraffin oil heated along a stainless steel wire with 0.25 mm diameter. The steel wire was installed parallel to and 5 mm away from the vertical stroke plane of the flapping wing (Fig. 2). Both the steel wire and the robotic model were installed on an aluminum alloy frame contained in a clear plexglass box, which prevented any air disturbances from the environment. A high-speed camera (Fastec Trouble Shooter, FASTEC IMAGING CORPORATION, San Diego, CA, USA) was used to record the smoke pattern at 1,000 frame/s, which was illuminated using a LED work Lamp. To increase the image resolution, the smoke pattern of a single wing (instead of the wing pair) was recorded. The experiments were performed at three different flapping frequencies: 5 Hz, 10 Hz, and 16 Hz.

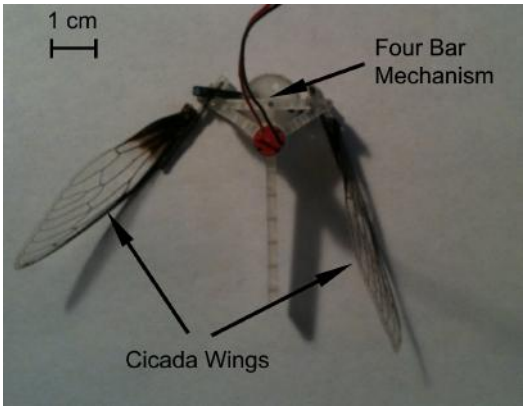

Figure 4.1: Flapper with cicada wings

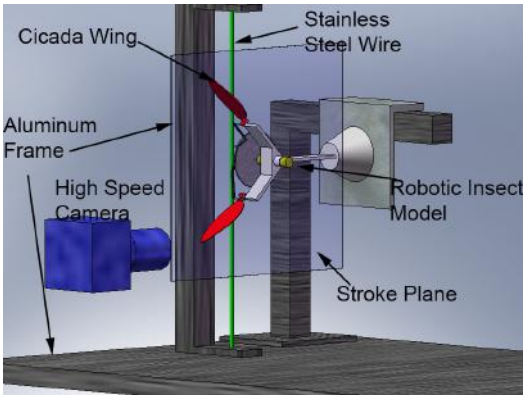

Figure 4.2: The experimental setup

4.1.3 Results and Discussion

Fig.4.3 shows the smoke visualization results for the flapping frequency at 5Hz, and results for other frequencies are shown in the supplementary materials. In Fig.4.3a, six frames for an upstroke (0-100ms) are shown, and three frames at 0, 40 and 100ms are shown in Fig.4.3b-d with more details. During the down-stroke, a large downwash accompanied by a strong vortex at wing tip and a minor vortex at wing base were observed (Fig.4.3b). At the beginning of the upstroke, after the wing quickly rotating,

the wing interacted with the wake of the down-stroke and two spiral rotational flow structures were observed (Fig4.3c). At the end of the upstroke, a large downwash with a strong vortex pair at wing tip and base were observed (Fig. 4.3d). For the cicada wing flapping at 10 and 16 Hz, similar flow patterns were captured as those at 5Hz (videos in supporting material). Notably, the minor feature of the rotational flow at beginning of upstroke could still be observed, but became less distinct. Comparing our visualization results with previous simulation results, the visualization results shows reasonable agreement with the simulation results in terms of the vortex structure (Aono et al 2008).

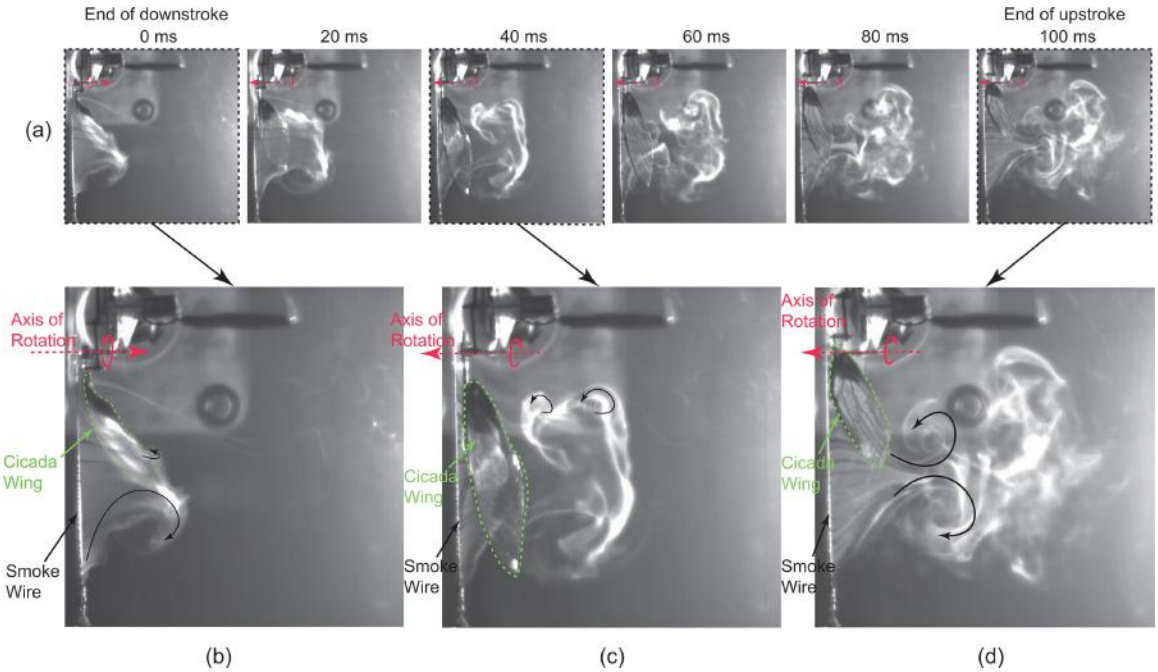

Figure 4.3: Smoke patterns showing the evolution of the flow structure in an upstroke (5 Hz), for more details refer to the video in the supplementary material.

In this paper, a new flow visualization method to study the flow on a hovering wing is introduced. By placing the smoke wire close to the wing stroke plane, we successfully visualized the flow on an insect wing without introducing free stream air flow. Therefore, this method allows us to study the flow on a flapping wing under an ideal hovering flight condition and can be used to study the flow on real hovering

animals. However, this method of flow visualization can only capture the flow passed around the smoke wire not the entire three-dimensional flow. In the next section, dye visualization method will be explored to test its capacity in the study of the entire complex flow in flapping wings.

4.2 Dye Visualization on a Mechanical Flapping Wing

4.2.1 Introduction

The flow pattern from smoke visualization actually presents the streak-lines which are quite different from the stream-lines in a highly unsteady flow (Smits and Lim 2000). Additionally, the smoke visualizations can only visualize the flow passed around the smoke wires or the places where the smoke was released. Therefore, the smoke visualization, as a common and conventional method in studying insect flight, is very restricted and can only capture and present limited flow information about the flapping wings. On the other hand, dye visualization, another common flow visualization method, is capable of visualizing the overall unsteady three-dimensional flow and has been succesfully demonstrated in several cases. For example, the dye visualization was successfully implemented on a pitching plate, visualizing a well linked three-dimensional vortex skeleton(Buchholz et al 2008). The fluorescent dye was also applied on a falling disk with the three-dimensional structures of tip vortices nicely visualized and captured (Lee et al 2013).

4.2.2 Experimental Method

A dynamic scaled flapper was designed to flap back and forth with two degrees of freedom (rotation and stroke) in a water tank at a frequency of 1/4 Hz. Wing kinematics was accurately controlled using a PID feedback control loop in simulink MATLAB with wing rotation and stroke angle in two sinusoidal functions. Before putting the wing into the tank, fluorescence dye was brushed on the wing surfaces. Once the wing was emerged in the water, the flapper started to flap. The wing platform is based on the fruit fly wing with a length of 40 mm. To let the fluorescent dye well attached to the wing surfaces, the wing was made from a plate of wooden balsa so that the fluorescence dye can soaked into the material. Finally the evolution

of flow structure was recorded by using a digital camera (Nikon) at a frame rate of 60 fps.

4.2.3 Results and Discussion

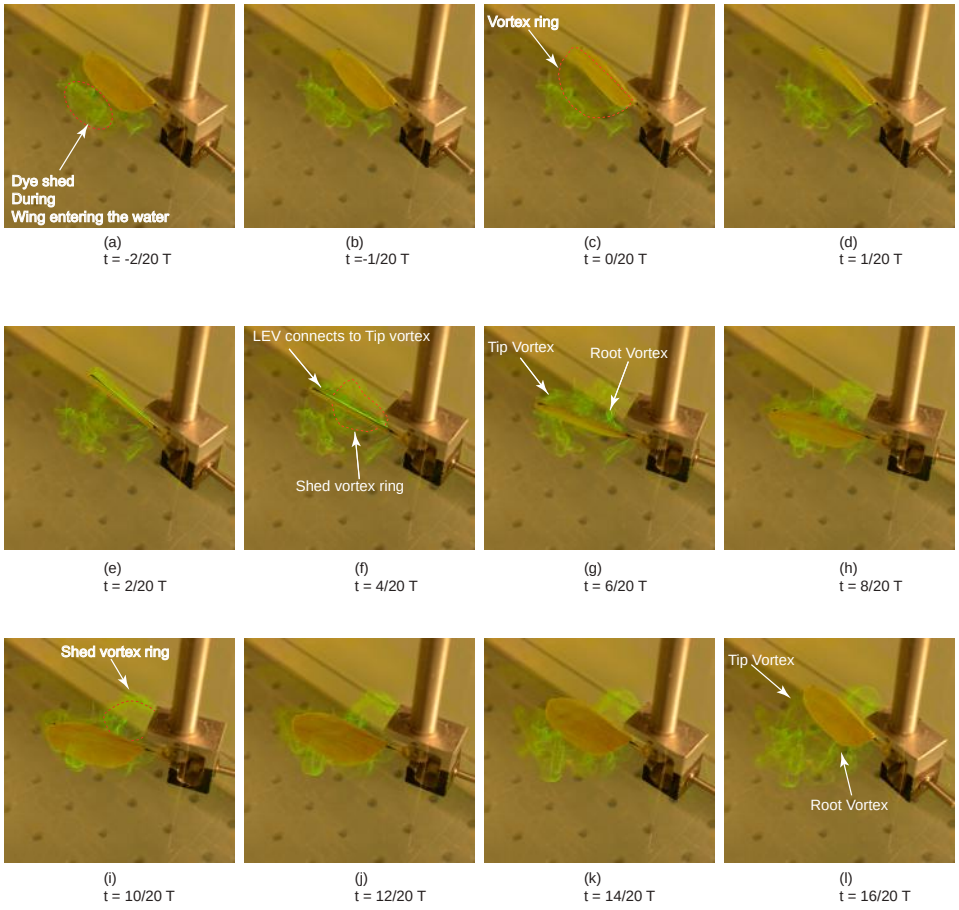

Figure 4.4: Dye visualizaiton results on a mechanical flapper.

Fig.4.4, shows a sequence of dye visualization results on the balsa wood wing in the very first stroke. Fig.4.4a-c present the vortical flow created during the onset of wing flapping. A clear vortex loop was created with part of it attached onto the wing surface as a leading edge vortex. In Fig.4.4d-h, the vortial flow in the first half stroke

is presented. During this half stroke, the vortex loop produced during onset was no longer attached onto the wing and shed into the wake while significant root and tip vortices were created with their ends connecting to the shed vortex loop. The leading edge vortex, growing from the root to tip, tilted significant near the tip and connected to the tip vortex. Fig.4.4i-l, present vortical flow in the second half stroke. During the stroke reversal, no vortex loop can be observed. Instead, strong tip and root vortices were created in the wake. Notably, the tip and root vortices move toward each other as they convecting downward which has been also observed in the Chapter 2, showing the tip and root vortices are converging in the two-layer structure.

Here, in this section, dye visualization was implemented on a mechanical flapping wing. The dye brushed on the wing surfaces can nicely track the major flow feature like leading edge vortex, tip vortex and root vortex. Under current experimental setup and experimental conditions, the visualization result indicates the wake flow in the flapping wing is dominated by the tip and root vortices with leading edge vortex attached on the wing surface though out the flapping cycles except the stroke reversals. Compared to the volumetric flow measurement in the Chapter 2,however,vortex ring structure is not captured in this dye visualization study which might be casused by the difference of the wing kinematics.

Although the V3V flow measurement and dye visualization in Chapter 2 and 4 depict detialed vortical flow structures on flapping wings, it is clearly questionable to refer our results to real flying insects, considering their complex wing morphologies. In next chapter, a substantial new study will be carried out on a freely flying insect to study the authentic complex flow in flapping wings.

5. INSECTS FLY ON LADDERS OF VORTICES

Submitted (First Author: Yun Liu)

5.1 Chapter Abstract

To date, a comprehensive understanding of the complex flow topology generated by freely flying insects has eluded the scientific community due in part to the inability to adequately study the unsteady three-dimensional flow structure in a natural setting (Srygley et al 2002,Henningsson et al 2015, Johansson et al 2013). In the absence, researchers have primarily relied upon either two-dimensional conventional flow visualizations/measurements on tethered insects or dynamically scaled experiments utilizing robotic flappers fitted with scaled insect wings undergoing simplified flapping motion (Ellington et al 1996,Birch and Dickinson 2003, Bomphrey 2006,Pick and Lehmann 2009, Mountcastle and Daniel 2009,Lua et al 2010). To overcome the limitations of these studies, a new method of flow visualization is developed and successfully implemented on freely flying hawkmoth Manduca sexta. We discovered a linked ladder like vortex structure under each wing on freely flying Manduca. This linked ladder structure of vortices is formed by the vortex loop produced in the downstroke joined by the tip and root vortices in the upstroke. After every stroke reversal, the newly formed vortex structure is linked to the previous vortex structure created in the last half stroke, thus forming a ladder of vortices under each wing. Previous experimental flow observations on fish and pitching plates have also revealed similar linked chains of vortices (Drucker and Lauder 1999, Flammang et al 2011, Buchholz et al 2008), suggesting a commonality of linked vortex structure among different forms of animal locomotion.

5.2 Results and Discussion

The complex flow topology of flapping wings, revealed through smoke visualization techniques conducted on insects and robotic flappers, established the prominence of a stably attached LEV responsible for lift augmentation in flapping wings (Van den berg and Ellington 1997, Ellington et al 1996), differentiating this unique form of animal locomotion from conventional fixed wing aerodynamics. Further characterized by scaled tank experiments with robotic flappers, quantitative force data was correlated to models of the quasi-steady aerodynamic mechanisms formulated from detailed experimental observations(Dickinson et al 1999). Computational Fluid Dynamics (CFD) simulations using simplified flapping wing motion, on the other hand, have provided an abundance of flow and force data, supporting empirical results and providing further intuition (Liu et al 1998). The results of these fundamental studies, in addition to several others (Weis-Fogh 1973,Maxworthy 1979, Dudley and Ellington 1990, Fry et al 2003, Sun and Tang 2002, Lentink and Dickinson 2009, Wang 2005), form the foundation of our current understandings on the aerodynamics of insect flight.

In the establishment of these findings, however, researchers have relied primarily upon experiments on either tethered insects or robotic flappers but rarely on freely flying insects. Moreover, experimental observations of the local and extended flow field on flying animals have been limited by the applications of traditional flow visualization/measurement techniques. For instance, smoke wire visualization techniques used on tethered or freely flying insects in wind tunnels necessitate a non-negligible relative flow velocity (larger than 0.4m/s) (Srygley et al 2002, Ellington et al 1996, Bomphrey et al 2009, Thomas et al 2004), thus precluding the study of hovering flight. Smoke plume visualization on a hovering hummingbird was used to reconstruct portions of three-dimensional structure in the downwash without continuously capturing the details of vortices (Pournazeri et al 2012). These visualization methods, after all, depict patterns of streaklines leaving the vortical structures to be later

interpreted from these patterns (Smits and Lim 2000). Particle image velocimetry (PIV), on the other hand, has been used extensively in the study of insect flight (Johansson et al 2013,Birch and Dickinson 2001, Bomphrey 2006, Pick and Lehmann 2009, Mountcastle and Daniel 2009), with recent applications of tomographic PIV providing measurements of the three-dimensional flow structure in the far field wake of a tethered locust (Henningsson et al 2015). However, these quantitative studies have either focused on the near-field flow features on two-dimensional planes or far field three-dimensional flow features in the wake region away from the wings. Thus a detailed overview of three-dimensional vortex structure, in both near- and far field, has never been fully captured on a freely flying insect.

The present work overcomes the limitations associated with these traditional flow visualization/measurement methods through the use of a density gradient medium (isopropyl alcohol) applied to the surfaces of insect wings and the use of high speed Schlieren photography. For the first time, the overall vortex structure and its development on freely flying hawkmoth Manduca sexta is directly visualized experimentally, revealing a linked ladder structure of vortices under each wing.

Utilizing this new method, images of distinct vortex structures were obtained on a near hovering Manduca and an ascending Manduca. Fig 5.1 and 5.2 present the flow structure on a near hovering Manduca with an average flying speed of 0.3 m/s. Fig. 1 shows the images of vortex structure in the down-stroke. A combined structure of starting vortex and stopping vortex was observed on each wing in the beginning of down-stroke right after wing pronation (Fig 5.1 a). Then very quickly, on each wing, distinct tip vortices were generated by both the fore- and hind-wing (Fig 5.1 a). Meanwhile, a stable leading edge vortex was created with one end connecting to the fore-wing tip vortex. However, we found no evidence of a continuous leading edge vortex crossing over the thorax which was observed in the previous flow visualization/measurement studies on tethered Manduca in the wind tunnel6; instead, a cone shaped leading edge vortex was observed (Fig 5.1 c) on each wing. As a result, an open vortex loop (or horseshoe-shaped vortex (Liu et al 1998, Zheng et al 2013) is cre-

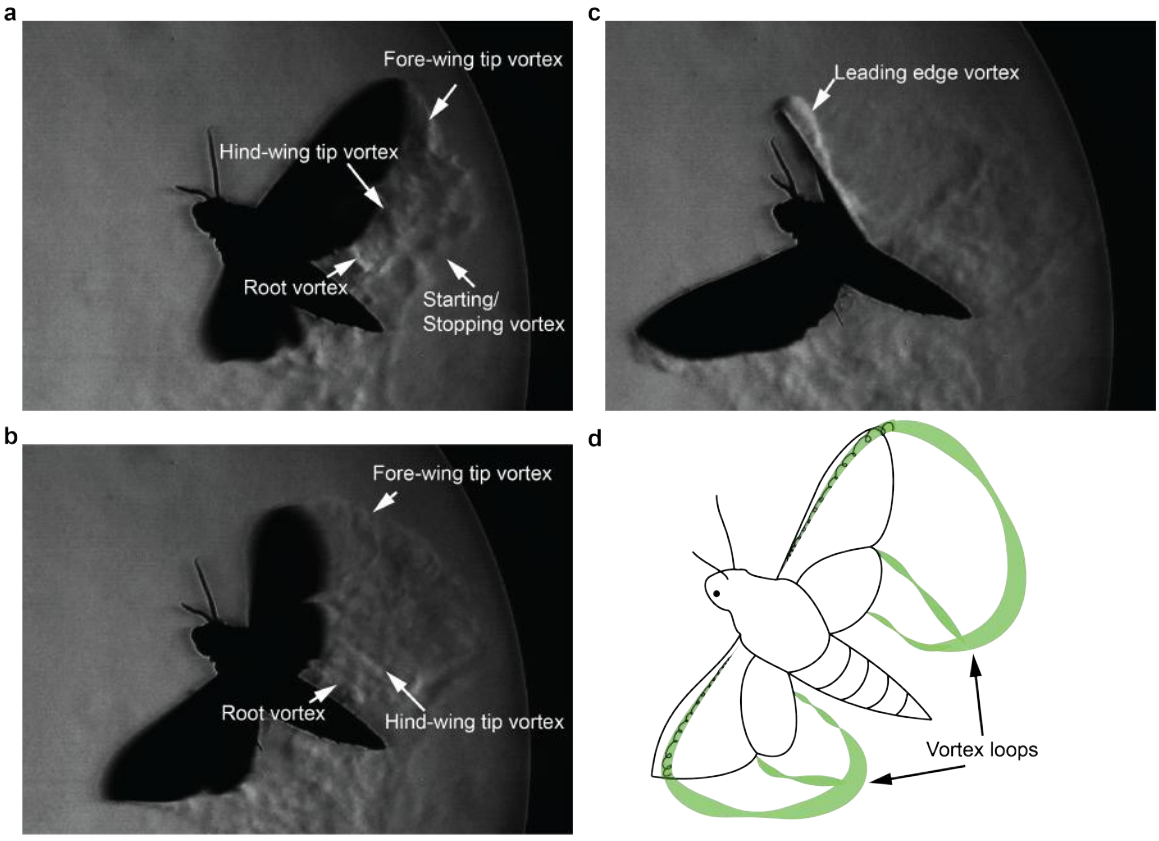

Figure 5.1: Vortex structures captured in the down-stroke on a near-hovering male hawkmoth (mass 1.26 g) with an average flying speed of 0.3 m/s (See Supplementary Video 1). a. A combined structure of starting/stopping vortex after wing pronation. b. Tip vortices are created from not only tips of fore-wings but also tips of hind-wings. c. An attached cone shaped leading edge vortex before wing supination. d. Eventually, the down-stroke of each wing creates an open vortex loop (horseshoe vortex loop), connecting the leading edge vortex, tip vortex, starting/stopping vortex, and root vortex.

ated on each wing, connecting the leading edge vortex, tip vortex, starting/stopping vortex, and root vortex (Fig 5.1 d). Video of the vortex structure in down-stroke can be found in the supplementary video file Fig.1.avi. This open vortex loop structure on Manduca has been previously observed in experimental and numerical studies on Manduca models (Van den berg and Ellington 1997, Liu et al 1998,Zheng et al 2013). Having never been observed on freely flying Manduca directly, the observance of the open vortex structure presented in this work thus serves as the first confirmation of

these studies. Furthermore, unique to previous experimental and numerical studies on Manduca, the existence of a secondary hind-wing tip vortex as revealed by this technique presents a more complete depiction of the open vortex loop structure generated by flapping wings. At the end of the down-stroke, during the supination (Fig 5.1c), the cone shaped leading edge vortex, under a significant deformation due to the rapid wing twisting, can be clearly seen. Subsequently, the leading edge vortex is then shed into the wake along with the other vortices created during the down-stroke, forming a closed vortex loop.

The vortex structure during the upstroke is shown in Fig 5.2. After wing supination, a closed vortex loop was shed into the wake from each wing while two strong tip vortices were created from the tips of fore- and hind-wings with ends connecting to the previously shed vortex loop (Fig 5.2 c). Concurrently, a root vortex was created, also connecting to the shed vortex loop. However, unlike the flow structure captured in the down-stroke, we found no evidence of a strong attached leading edge vortex during the up-stroke. This is consistent with results from smoke visualization studies and CFD simulations on a hovering Manduca model (Van den berg and Ellington 1997, Zheng et al 2013), and is indicative of a lack of vortex loop formation during the up-stroke. Therefore, after one complete wing beat cycle, the resulting vortex structure created under each wing consists of a vortex loop in the far wake, two tip vortices and a root vortex in the near field.

Fig.5.3a-b show the vortex structure on an ascending Manduca with an average speed of 0.7 m/s. Similar to vortex structures in Fig.5.1 and 5.2, an open vortex loop is first created on each wing during the down-stroke and shed after supination (Fig.5.3a). In the up-stroke, two strong tip vortices were created from the tips of fore- and hind-wings and linked to the previously shed vortex loop (Fig.5.3b). Interestingly, vortex structure visualized on the ascending Manduca illustrated a more pronounced linked ladder like structure which not only connects the vortex structures between down- and up-stroke but also connects the vortex structures between each wing beat cycle. In the near hovering flight case, evidence of the linked structure can be also

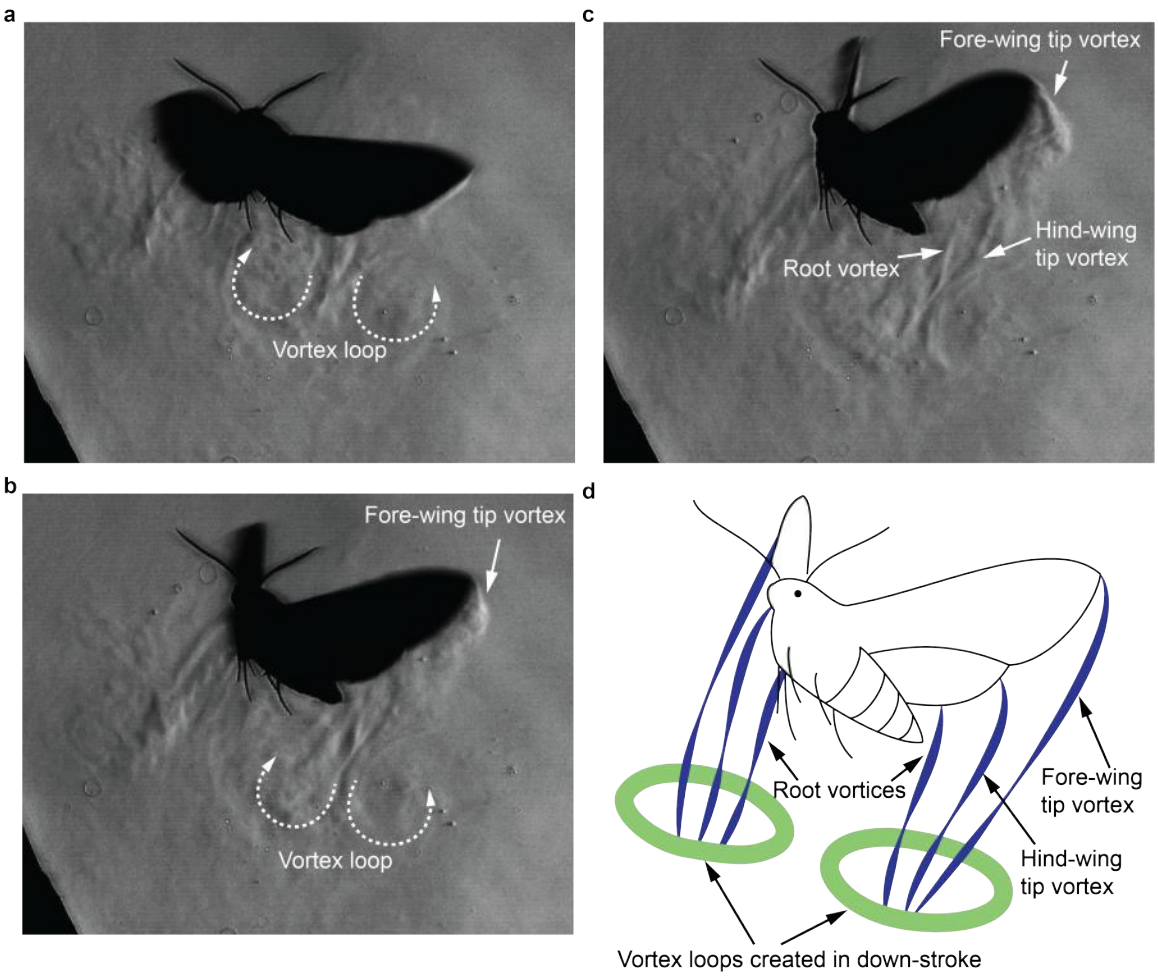

Figure 5.2: Vortex structures captured in the up-stroke on the near hovering hawk-moth (See Supplementary Video 2). a. The vortex loop created in down-stroke sheds into the wake. b-c Long, stretched tip vortices from the tips of fore-wings and hind-wings are created and connected to the just shed vortex loops. d. Finally, the up-stroke of each wing creates long, stretched tip and root vortices, connecting the shed vortex loop to the wing.

found. Fig.5.3c depicts the linkage formation between the vortex structure in a wing beat (up-stroke) to the vortex structure in the next wing beat (down-stroke) in the near hovering case. During wing pronation, the tip/root vortices from the up-stroke shed from the wings and then connect to the stopping/starting vortices, formed in the beginning of the down-stroke, thereby connecting the vortex structures between each wing beat. Consequently, our direct flow visualization results reveal a well

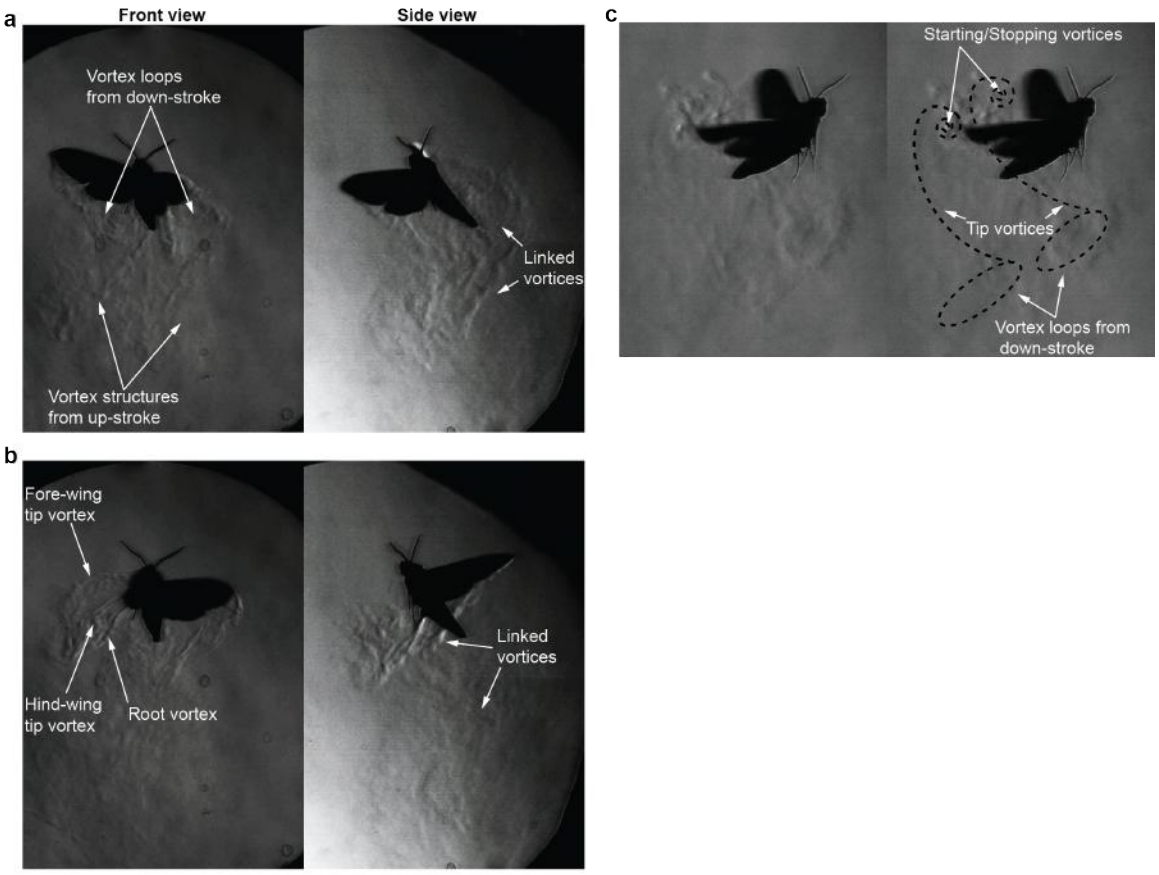

Figure 5.3: Vortex structures from consecutive wing beat cycles are well linked. a-b. The vortex structure capured on an ascending male hawkmoth(mass 0.93 g) with an average flying speed of 0.7m/s (left and right columns show the flow structure filmed from front and side views). a. On the ascending hawkmoth, a vortex loop is created on each wing in the down-stroke and the vortex loop is connected to the vortex structure creaed from the last up-stroke.b.In the up-stroke, stretched hind-and fore-wing tip vortices as well as root vortex are created on each wing,connecting to the vortex loop from the down-stroke.c.Between consecutive wing beat cycles, a linked structure is also observed on the near hovering hawkmoth. Tip vortices from the up-stroke shed from the wings and connect to the starting/stopping vortices, thereby connecitng the vortex structures between each wing beat cycle. Left image shows the original image of the strucutre and right image shows notated vortex structure.

linked vortex structure on freely flying Manduca. Especially in the ascending case, the Manduca creates a ladder of vortices under each wing. However, due to flow dissipation and instabilities, the entirety of the ladder-like structure underneath the wing could not be seen. Instead, only the linked structure within two wing beats is

visible, with the remaining structure dissipated into the wake. Ignoring these effects and hind-wing tip vortex, a simplified linked vortex model is presented in Fig.5. 4.

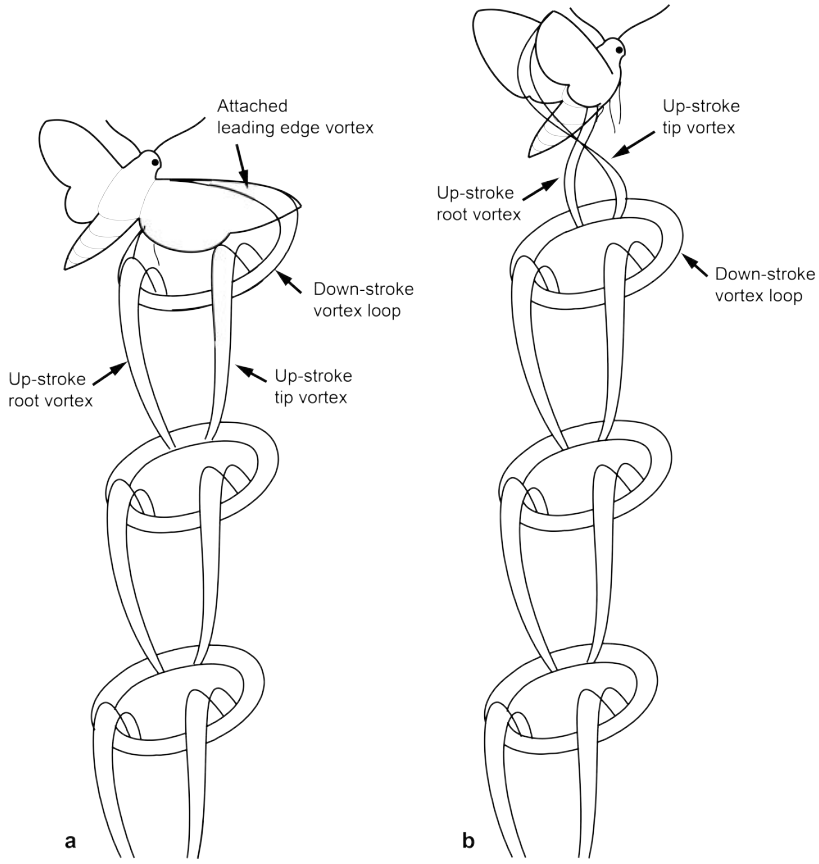

Figure 5.4: Vortex ladder under an ascending hawkmoth. a. In the down-stroke, a vortex loop is created and linked to the other vortex loops through tip and root vortices formed from up-strokes, forming a ladder of vortices under each wing. b. In the up-stroke, stretched tip and root vortices are created on each wing connecting the just shed vortex loop to the wing.

The linked ladder structure of vortices presented may not be unique to Manduca, but rather may be a common feature of multiple forms of animal locomotion. Both two-dimensional PIV measurements and volumetric flow measurements have revealed linked vortex rings or chains of vortex rings on freely swimming fish (Drucker and Lauder 1999, Flammang et al 2011). Smoke visualization on hovering hummingbirds illustrated a bilateral vertically connected vortex ladder structure under the pair wings (Pournazeri et al 2013). Utilizing a state of the art flow visualization method, a chain

of linked vortex rings was also found to form the wake of a pitching plate undergoing periodic motion similar to that of flying and swimming animal locomotion (Buchholz et al 2008); The formation of this chain of linked vortex rings was associated with the pitching plate at the highest thrust efficiency, while the wake divides into two separate trains of vortical structure at low thrust efficiency. Similarities between the linked vortex structure found on pitching plate and the vortex ladder observed on each Manduca wing suggests a possible connection between the formation of single chain vortex ladder structures and optimal thrust efficiency in freely flying Manduca. Clearly, the mechanics of unsteady force generation and unsteady three-dimensional wake structure must be correlated. Therefore, from a more complete depiction of the wake topology on freely flying insects and its evolution, the complexities of flying insect aerodynamics and associated performance metrics (like efficiency) can be more accurately modeled and assessed.

The flow topology of flying Manduca has served as a classic study case for flapping wing locomotion, having been the subject of scientific research for over two decades. However, due to the limitations of traditional flow visualization techniques, the overall vortex structure on a freely flying Manduca has never been fully captured until now. Utilizing a new method of flow visualization on flying insects, this work reveals a linked ladder structure of vortices on each wing of the freely flying Manduca, resulting from the formation of a vortex loop created during the down-stroke (see Fig.4a) and long, stretched tip and root vortices created during the up-stroke connecting the shed vortex loop to the wing (see Fig.4b). During wing pronation, the tip and root vortices in up-stroke shed from the wing and connect to the stopping/starting vortices in the down-stroke, thereby forming a ladder of vortices. In addition to this topological depiction of the wake, several clarifying remarks about the observed vortical structure of freely flying Manduca can be made. First, the wing pair of flying Manduca clearly create a bilateral vortex structure without formation of a single vortex ring in the down-stroke where by the LEV is continuous over the thorax6. Second, in the up-stroke, no evidence of a strong attached LEV was found, suggesting

the existence of a weak or even no formation of a LEV on freely flying Manduca in up-stroke27 . Lastly, applications of this new method of flow visualization are not limited to the current study and could also be used in the study of other flying animals ranging from hummingbirds (Trochilidae) and butterflies (Lepidoptera) to smaller insects such as flies (Diptera). By providing sufficient time resolved three-dimensional information about the complex flow structure, results from this technique could be used as validation for existing flow measurements and CFD simulation results.

5.3 Method

Male Manduca sexta adults were obtained from the Purdue University Entomology department. A high speed Schlieren photography system was implemented to visualize the unsteady three-dimensional vortical flow on freely flying Manduca. This system consists of two single mirror, double-pass, Schlieren setups with two high speed cameras (Mini UX100, Photron), filming from two orthogonal views. In each Schlieren system, a white LED light was projected through a 1 mm pin hole onto a 10-inch diameter optical spherical mirror (Edmond optics). A portion of the reflected light was then redirected towards the high speed camera using a 50/50 (reflection/transmission ratio, Edmond optics) beam-splitter for capture. At the focal point of the reflected light, a razor blade was used as the knife-edge producing the Schlieren images (See Fig.5.5).

To trace the vortical flow produced by the flapping Manduca wings, warm isopropyl alcohol (91% Isopropyl Alcohol heated to 38oC) was brushed onto the surface of both wings in the beginning of each test. The Manduca was then released to fly freely in the flow observation region. Upon wing acceleration and rotation, airflow over the wing surface increases vaporization of the alcohol, drawing it into the vortex sheet/vortices created from the wing surface. The Schmidt number of vaporized median is estimated to be on the order of one, taking the diffusion coefficient of isopropyl alcohol in air to be 0.1011 cm2/s. Since the diffusion rates of vorticity and

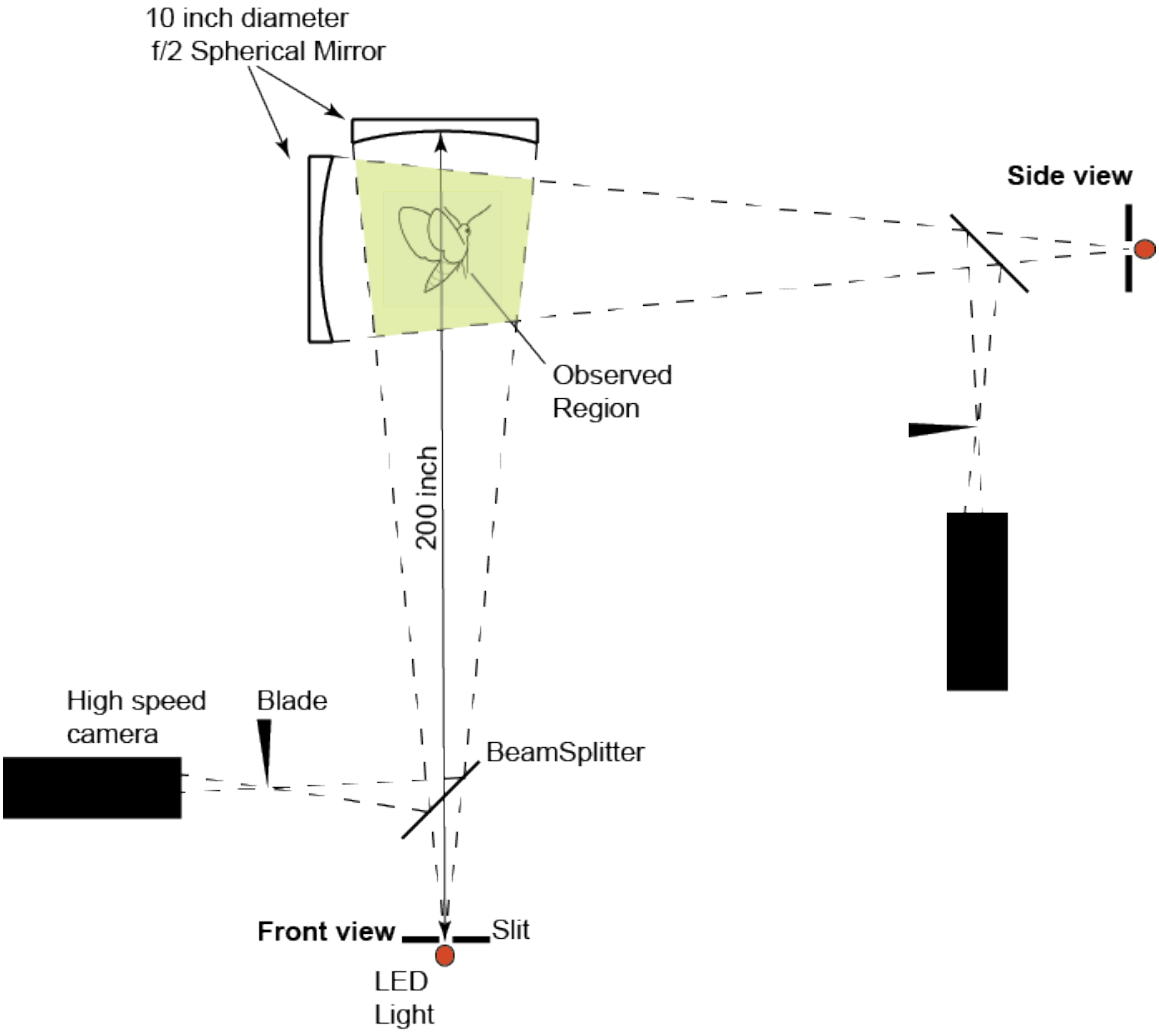

Figure 5.5: Experimental Setup

the visualization median are comparable, formations depicted by the alcohol vapor will accurately capture the vortical flow structures in the absence of strong vortex stretching.26 Through our high speed Schlieren photography system, the unsteady three-dimensional vortex structure was visualized and recorded by two high speed cameras at 1000 frames per second from two orthogonal views. Similar methods of flow visualization have also been used to study the vortical flow development around moving objects (Veldhuis et al 2005, Pierce 1961). In total, thirty tests were conducted and results from the two most illustrative tests were presented in this paper.

To enhance images of the complex vortex structure on the Manduca, the brightness and contrast of the images were adjusted accordingly using Adobe Photoshop CS6. The moths average translating speed was extracted by tracking an eye of the Manduca using DLTdv5 (Hedrick 2008) .

6. SUMMARY

Insect flight is essentially a complex system that requires multidisciplinary efforts from different perspectives. This thesis focuses on the aerodynamics of insect flight from a fluid mechanics point of view, studying three highly coupled features in the aerodynamics of insect flight: unsteadiness, three-dimensional effect and wing morphing.

The V3V system (or Defocusing-DPIV method) lends us a great opportunity to study the coupling between unsteadiness and three-dimensional effect. Its ability of measuring instantaneous three-dimensional velocity field in a volumetric space makes this method unprecedented in studying complex flow on mechanical flappers, compared with other conventional flow visualization/measurement methods. Utilizing the V3V system, the entire unsteady three-dimensional flow field on a mechanical flapper was quantified and visualized, depicting a linked vortex rings structure in the near-field and two layers of vortical flow in the far-field. Yet, due to the limitations of the laser and other related equipment, a time resolved flow measurement could not be achieved. As the resulting aerodynamic force on the flapping wing depends on the time derivative of the vorticity field(Wu 1981), it is impossible to build a direct correlation between the flow field and the resulting aerodynamic force without time resolved flow data. Moreover, regardless the aero-elastic issue, the actual flapping wing motion of flying insect is hard to be mimicked on the small one degree of freedom mechanical flapper only which can fit into the small measurement space (10cm×14cm×14cm). This issue was later overcome by using a larger two degrees of freedom mechanical flapper with several measured flow regions patching around the flapper to obtain the entire flow field (Cheng et al 2014). However, with a much larger measured space, the time spent on data processing is significantly increased.

In the absence of three-dimensional effect, the coupling between unsteadiness and active wing morphing is investigated on a large aspect-ratio translating wing. Interestingly, similar flow phenomenon from previous wind tunnel experiments on bats was also observed in our study, indicating the effectiveness of our simplified model in representing the active morphing wing. Our study also reveals the dominate role of wing deformation timing in the flow and aerodynamic force characteristics. Although a primary correlation between the flow and aerodynamic force characteristics have been presented, a deeper investigation on the added mass effect and vortex force should be conducted to determine the role of wing acceleration. Therefore, if possible, it is necessary to study the active wing morphing effect under different wing acceleration durations (acceleration duration is fixed at 0.4 second in our study) to have a better understanding on the coupling of unsteadiness and wing morphing.

Yet, on flying animals, the aerodynamics is essentially the outcome of the complex coupling and interaction of all those three factors. As there is no mechanical flapper can perfectly simulate the flying animals with all these factors considered, thus, the optimal way of studying flapping wing aerodynamics is study the flow on real flying animals. In the meanwhile, considering the limitations of traditional flow visualization/measurement methods, a new method to of capturing and presenting the complex flow topology on freely flying animals is in a great demand.

In the beginning, I explored two very typical and traditional flow visualization methods: smoke and dye visualizations. Particularly, the smoke wire visualization was implemented by placing the smoke wire close to the flapper to visualize the downwash flow on a *'hovering* wing without introducing any free stream velocity. Dye visualization was also implemented on a mechanical flapper in a water tank. Because the dye, released from the wing surface, actually presents the passive scalar which can depict and follow the formation of vortex structure,it provids a complete picture about the three-dimensional vortical flow on the flapper. Based on the dye visualization study and Pierce*s* pioneering flow visualization work with shadowgraph (Pierce 1961), I proposed and implemented a new method of flow visualization on

flying insects,by introducing alcohol vapor on the insect wings to track the formation and development of three-dimensional vortical flow which can be later seen through a high speed Schlieren photography system.

Our new method with isopropyl alcohol is able to directly visualize and present the vortical flow. The diffusion coefficient of isopropyl alcohol in the air is $0.1011 cm^2/s$, making its Schmidt number on the order of 1 which is the most desired number for the media to track the vortical flow in the absence of strong vortex stretching (the Schmidt number for smoke and dye visualization is around 1000. So dye or smoke can only track the vortex formation in the near wake flow region (Buchholz et al 2008). This advantage can be explained in the following.

$$\frac{\partial \omega}{\partial t} = -(V \cdot \nabla)\omega + (\omega \cdot \nabla)V + \nu \nabla^2 \omega \tag{6.1}$$

$$\frac{\partial S}{\partial t} = -(V \cdot \nabla)S + D \nabla^2 S \tag{6.2}$$

Equation 6.1 is the vorticity transport equation and Equation 6.2 is the passive scalar transport equation. ν in equation 6.1 is the kinematic viscosity, presenting the speed of momentum diffusivity and D in equation 6.2 is the diffusion coefficient, presenting the speed of mass diffusivity. Schmidt number is defined as the ratio of ν to D. With Schmidt number in the order of 1, it means the value of ν is close to the value of D. Then the equation 6.1 and 6.2 are almost identical expect the vortex stretching term $(\omega \cdot \nabla)V$. Therefore, in the absence of strong vortex stretching and with isopropyl alcohol released from the wing surfaces (the origion of vorticity), the alcohol can nicely track the formation and evolution of the vortical flow in both near- and far- field(Smits and Lim 2000). In addition, comparing with the tomographic PIV, this method has a great advantage of efficiency and simplicity. For example, to resolve the volumetric flow velocity field in the wake region of a tethered locust, nearly 100 days were taken to process all the images captured from eight high speed cameras (Henningsson et al 2015).

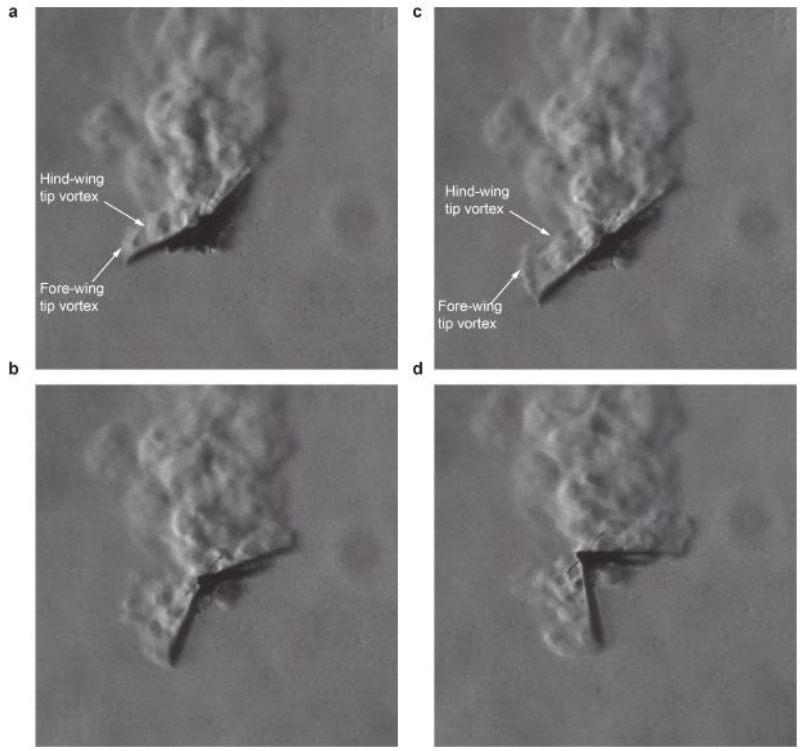

Figure 6.1: Secondary hind-wing tip vortex on a butterfly(images were shot in a sequence from a to d)

Clearly, our method of flow visualization has a great potential in studying the complex flow of flying animals and it was already tested on different insects. For example, Fig.6.1 shows the visualization results on a flying butterfly. Instead of introducing isopropyl alcohol on the wing surfaces of the butterfly, the butterfly wings are hold and warmed by electromagnetic holder and the warm air closed to the wings is served as the passive scalar to track the vortical flow. Once the butterfly was released from the electromagnetic holder(not showned in the images), it flapped its wings and the vortical wake was visualized. Especially, similar to the flow on the flying hawkmoth, a clear indication of secondary hind-wing tip vortex was observed ,suggesting the commonality of secondary hind-wing tip vortex amongst different insect speicies. The formation of this secondary tip vortex can be explained based on Helmholtz's theorem which suggests the vortex filament cannot end in fluids and should be in a closed form.

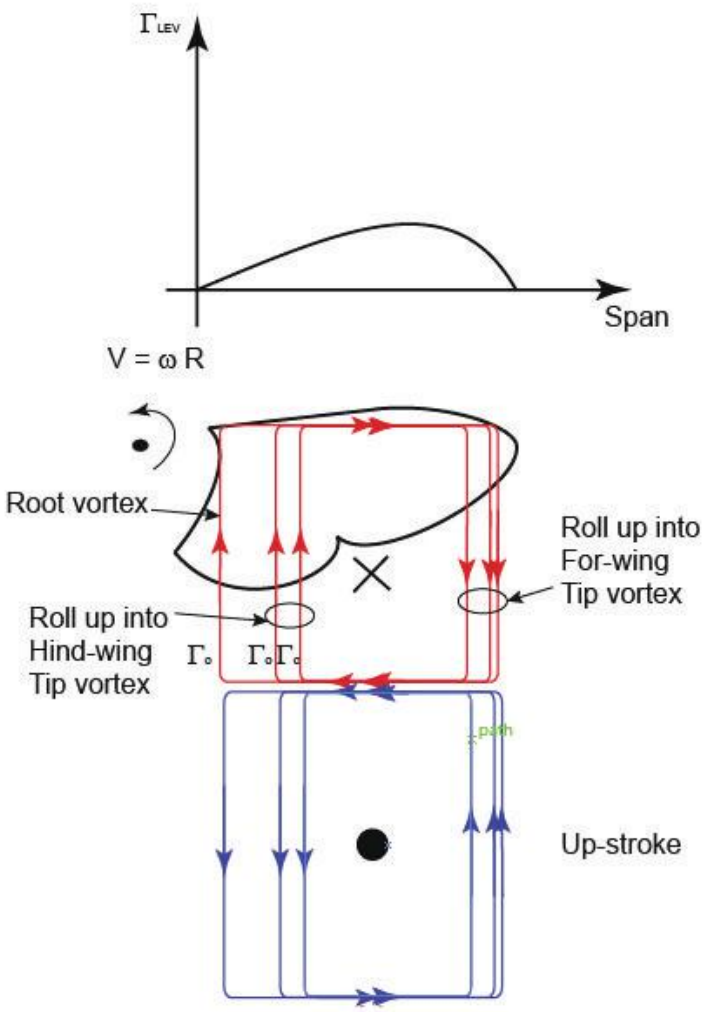

Figure 6.2: An explaination of the Secondary Tip vortex. Leading edge vortex strength is not evenly distributed with vortex filaments shed not evenly, creating a secondary vortex somewhere from wing root to tip. The red loops indicate the vortex structures created in down-stroke and vortex structure created in up-stroke is in blue

In Fig.6.2, on a flapping wing, the velocity along the the wing span is continuously growing from wing root to tip, due to the wing rotation. Therefore, the strength of leading edge vortex should be growing along the wing span in the beginning and quickly drop to zero at wing tip. Assuming the leading edge vortex is the dominant spanwise vortical flow (Ellington et al 1996), then to creat a high strength LEV close to wing tip and low strength LEV close to wing root, mutiple closed vortex loops(with

the same strength) should be superimposed unevenly. Thus more vortex filaments will shed from the wing tip and finally roll up into a strong tip vortex. At wing root fewer filament will shed and form the root vortex with the strength much less than the one of tip vortex. The rest vortex filaments, with the same rotating direction of root vortex but opposite rotating direction of tip vortex, will shed somewhere between wing root and tip, forming a secondary vortex. On flying hawkmoth and butterfly, the secondary vortices are all created closed to the tips of hind-wing with the reason not well understood yet.

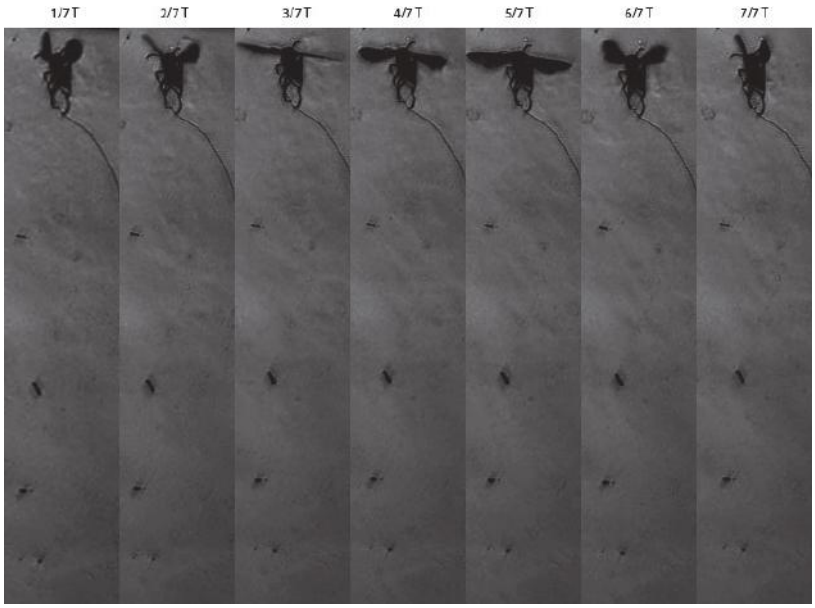

Figure 6.3: High speed Schlieren photography on a tethered Wasps

The main difficulty of this flow visualization method, however, is the treatment to live animals: how to apply the tracking media to their wing membranes and how to make them to freely fly in the designed region. Espeically, it is even more challenging to utilize this method on some small insects. Fig.6.3 shows a test of this flow visualization method on a tethered wasps(The alcohol was only applied on the right wing). With images enhanced already, it is still hard to see the flow structure created on the wasps wing. There are basically three reasons that the flow was not well visualzied. First, small insects like wasps have very high flapping frequency. The

alcohol will vaporize very quickly under high flapping frequncy after applying it onto the wing surfaces. Second, since the insect is quite small, it is very difficult to apply alcohol to the tiny wing memberane and hard to ensure enough alcohol was applied on all the wing sufaces. Third, a powerful camera lense is needed for small insects. In our tests, we used a 50-200 mm zoom lense, clearly not enough for resolving the flow image on a small insect like wasps. Therefore, to study the flow on small insects, this method of flow visualization has to be improved and modified accordingly.

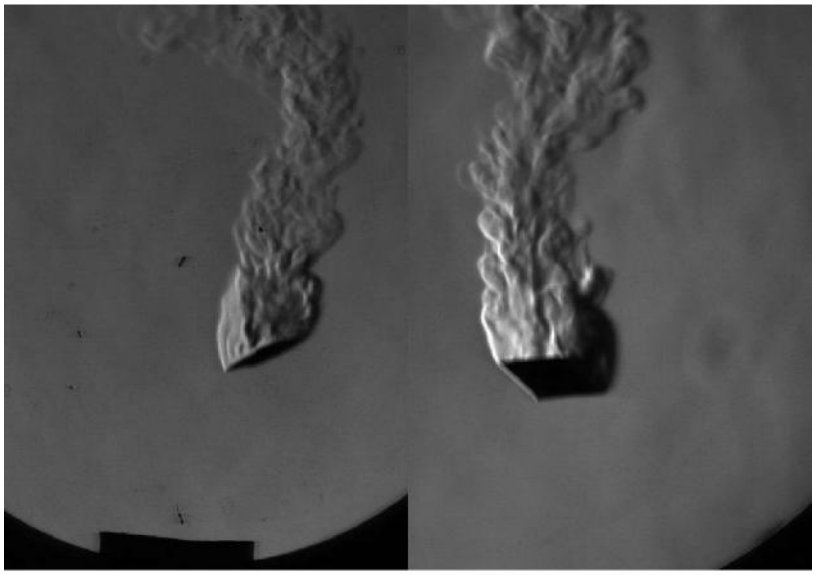

Figure 6.4: High speed Schlieren photography on a falling plate

Regardless the limitations of this method of flow visualization on small insects, this method is indeed a powerful tool in studying the three-dimensional unsteady flow and can be extended to other contex of studies. Fig.6.4 presents the flow visualization results on a falling plate. However, this method is qualitative after all and the corresponding results are hard to be quantitatively evaluated and processed. In the light of advancement on cameras (For example light field camera) and imaging techniques (holographic imaging), it is possible to improve and upgrade this method to a quantitative measurement tool in the future.

APPENDIX

A. APPENDIX

A.1 Flow Uncertainty

The uncertainty analysis of flow measurement and force measurement in Chapter 3 are addressed here. MATLAB function $'curl'$ was used to calculate the vorticity. In $'curl'$, the vorticity was calculated using central finite difference:

$$\omega_{i,j} = (\frac{u_{i,j+1} - u_{i,j-1}}{y_{i,j+1} - y_{i,j-1}} - \frac{v_{i+1,j} - v_{i-1,j}}{x_{i+1,j} - x_{i-1,j}})_{physicalspace} \tag{A.1}$$

In Equantion A.1 the velocity(u,v) in physical space is actually the velocity on the image times the calibration factor K and will eventually cancel out in the equation. Thus, the uncertainty in calibration will not affect the uncertainty on the vorticity measurement.

$$\begin{aligned} \omega_{i,j} &= \frac{K(u_{i,j+1} - u_{i,j-1})_{image}}{K(y_{i,j+1} - y_{i,j-1})_{image}} - \frac{K(v_{i+1,j} - v_{i-1,j})_{image}}{K(x_{i+1,j} - x_{i-1,j})_{image}} \\ &= (\frac{u_{i,j+1} - u_{i,j-1}}{y_{i,j+1} - y_{i,j-1}} - \frac{v_{i+1,j} - v_{i-1,j}}{x_{i+1,j} - x_{i-1,j}})_{image} \end{aligned} \tag{A.2}$$

Since the size of interrogation window is 32 X 32 pixels then $y_{i,j+1} - y_{i,j-1} = x_{i+1,j} - x_{i-1,j} = 32$ pixels So the uncertainty of vorticity:

$$\delta\omega_{i,j} = \frac{1}{32}\delta(u_{i,j+1} - u_{i,j-1} - v_{i+1,j} + v_{i-1,j})_{image} \tag{A.3}$$

Because the temporal uncertainty is negligible,

$$\begin{aligned} \delta\omega_{i,j} &= \frac{1}{32\Delta t}\delta(dx_{i,j+1} - dx_{i,j-1} - dy_{i+1,j} + dy_{i-1,j})_{image} \\ &= \frac{1}{32\Delta t}\sqrt{(2\delta(dx)^2 + 2\delta(dx)^2)_{image}} \end{aligned} \tag{A.4}$$

The spatial displacement accuracy for 32X32 interrogation window is $\pm$ 0.06 pixels. So δ(dx)=δ(dy)=0.06 pixels. Thus, $\delta\omega_{i,j}$=0.625 $1/s$(in the measurement Δt=6 ms). In addition, there was nuance of the relative motion between the camera and wing model during the accelerating phase. This relative motion would cause variation in velocity measurement but will not affect the vorticity measurement because the small relative motion only introduces a uniform displacement field and calculation of vorticity will remove this effect. Thus the relative linear translation between camera and wing model will not introduce any uncertainty on vorticity measurement. Since the maximum measured vorticity is about 25 /s thus the relative uncertainty of measured vorticity is around 4% .

A.2 Force Uncertainty

The uncertainty of force measurement is derived here and estimated at about 3 %. The aerodynamic drag force was calculated from subtracting the measured force on drag component $F_{D,measure}$ by the inertia force due to translation $F_{D,T}$ as well as the inertia force due to deflection on drag direction $F_{D,D}$.

$$F_{D,Aero} = F_{D,Measure} - F_{D,T} - F_{D,D} \tag{A.5}$$

Therefore, the uncertainty of aerodynamic drag force can be calculated by:

$$\delta F_{D,Aero} = \sqrt{\delta F_{D,measure}^2 + \delta F_{D,T}^2 + \delta F_{D,T}^2} \tag{A.6}$$

Here in this study, $F_{D,measure}$=$F_Y \cdot sin(\alpha)$-$F_X \cdot cos(\alpha)$ Then

$$\begin{aligned}\delta F_{D,measure} &= \sqrt{(\frac{\partial F_{D,measure}}{\partial F_Y}\delta F_Y)^2 + (\frac{\partial F_{D,measure}}{\partial F_X}\delta F_X)^2 + (\frac{\partial F_{D,measure}}{\partial \alpha}\delta\alpha)^2} \\ &= \sqrt{(\delta F_Y \cdot sin(\alpha))^2 + (\delta F_X \cdot -cos(\alpha))^2 + (F_Y \cdot cos(\alpha) + F_X \cdot sin(\alpha))^2 \cdot \delta\alpha^2}\end{aligned} \tag{A.7}$$

Current sensor has an uncertainty of δF_X=δF_Y=0.01 N (retrived from TSI documents). F_X=0.1N; F_Y=1.0 N(the highest measured force).In our measurement, $\delta\alpha$ =1^o=0.0175 rad (Protractor was used to measure the AOA). Therefore, $\delta F_{D,measure}$=0.0178. To calculate $\delta F_{D,D}$,

$$\delta F_{D,D} = \sqrt{(\delta F_Y \cdot sin(\alpha))^2 + (\delta F_X \cdot -cos(\alpha))^2 + (F_{Y,D} \cdot cos(\alpha) + F_{X,D} \cdot sin(\alpha))^2 \cdot \delta\alpha^2} \tag{A.8}$$

$F_{X,D}$ is measured in the air, the magnitude of $F_{X,D}$ is about 0.06 N (maximum value) therefore,$\delta F_{D,D}$ =0.010 N. $\delta F_{D,T}$, the uncertainty of measured inertia force, is caused by the uncertainty of image calibration and kinematics of wing translation is very repeatable. We used a 2 cm wide target(L_m=20mm;δL_m=1mm) to calibrate the image and on the image the target is 83 pixels wide (L_p=83pixels;δL_p=5 pixels). Consequently, the uncertainty of the calibration coeffcient can be calculated as:

$$\delta K = \sqrt{(\frac{\delta L_m}{L_P})^2 + (\frac{L_m}{L_P^2} \cdot \delta L_P)^2} = 0.0187 mm/pixel \tag{A.9}$$

Because the measured hightest wing acceleration on the camera is $2450 pixels/s^2$. Therefore, $\delta a = \delta K \cdot L$=45.8 mm/s^2. Then with $\delta a = 45.8 mm/s^2$ and $\delta m = 0.01g$

$$\delta F_{D,T} = \sqrt{(\delta m \cdot \alpha)^2 + (\delta\alpha \cdot m)^2} = 0.006N \tag{A.10}$$

Because the kinematics of wing translation has very good repeatability and the uncertainty of measured acceleration only come from the image calibration. Therefore, the actual aerodynamic force on the wing will not be affected by the uncertainty on measured acceleration. Eventually, the overall uncertainty on aerodynamic drag force is

$$\delta F_{D,Aero} = \sqrt{\delta F_{D,measure}^2 + \delta F_{D,T}^2 + \delta F_{D,D}^2} = 0.0213N \tag{A.11}$$

Following the same procedure we have $\delta F_{L,Aero}$=0.0178 N. With maximum force: $F_{D,Aero}$=0.86 N and $F_{L,Aero}$=0.63 N , The uncertainty on force measurement is only about 3% .

LIST OF REFERENCES

LIST OF REFERENCES

[1] Altshuler, D., Princevac, M., Pan, H. and Lozano, J. Wake patterns of the wings and tail of hovering hummingbirds. *Exp.Fluids*, 46, 835-846, 2009

[2] Anderson, J.D. A History of Aerodynamics. *Cambridge University Press.*, 1999

[3] Ansari, S. A., Zbikowski,R. and Knowles,K. Non-linear unsteady aerodynamic model for insect-like flapping wings in the hover. Part2: implementation and validation. *J. Aerospace Engineering*, 220(3), 169-186, 2006

[4] Aono,H., Liang, F. and Liu, H. Near- and far-field aerodynamics in insect hovering flight: an integrated computational study. *J. Exp. Biol.*, 211, 239-257, 2008

[5] Batchelor,G.K. An introduction to fluid dynamics. *Cambridge University Press.*, 1967

[6] Beal,D.N., Hover,F.S., Triantafyllou,M.S., Liao,J.C. and Lauder,G.V. Passive propulsion in vortex wakes *J.Fluid.Mech.*, 549, 385-402, 2006

[7] Birch,J.M. and Dickinson,M.H. Spanwise flow and the attachment of the leading-edge vortex on insect wings. *Nature*, 412(6848), 729-733, 2001

[8] Birch,J.M. and Dickinson,M.H. The influence of wing-wake interactions on the production of aerodynamic forces in flapping flight. *J. Exp. Biol.*, 206(13), 2257-2272, 2003

[9] Bilgen,O., Kochersberger, K.B. and Inman,D.J. Novel, Bidirectional, Variable-Camber Airfoil via Macro-Fiber Composite Actuators. *J.Aircraft*,47(1),303-314,2010

[10] Bomphrey, R. J., Talor, G.K. and Thomas, A.L.R. Smoke visualization of freely-flying bumblebees indicates independent leading-edge vortices on each wing pair. *Exp. Fluids*, 46, 811-821, 2009

[11] Bomphrey, R. J., Lawson, N.J., Taylor, G. K. and Thomas, A.L.R. Application of particle image velocimetry to insect aerodynamics: measurement of the leading-edge vortex and near wake of a Hawkmoth. *Exp. Fluids*, 40,546-554, 2006

[12] Buchholz, J.H.J. and Smits, A.J. The wake structure and thrust performance of a rigid low-aspect-ratio pitching panel. *J. Fluid Mech.*, 603, 331-365, 2008

[13] Chen, K., Colonius, T., and Taira, K. The leading-edge vortex and quasi-steady vortex shedding on an accelerated plate. *Phys. Fluids*, 603, 331-365, 2010

[14] Cheng, B., S. Sane, G. Barbera, D. Troolin, T. Strand and X. Deng. Three-dimensional flow visualization and vorticity dynamics in revolving wings. *Exp. Fluids.*, 54, 2013

[15] Cheng,B.,Roll,J.,Liu,Y.,Troolin,D.R. and Deng,X. Three-dimensional vortex wake structure of flapping wings in hovering flight. *J. R. Soc. Interface*, 11, 1742-5662, 2014

[16] David,L.,Jardin,T.,Braud,P. and Farcy, A. Time-resolved scanning tomorgraphy PIV measurements around a flapping wing. *J. R. Soc. Interface*, 11, 1742-5662, 2012

[17] Deng,X., Schenatp,L.,Wu, W.C.,and Sastry,S.S. Flapping flight for biomimetic robotic insects: Part I system modeling. *IEEE Transactions on Robotics*,22(4),776-788, 2014

[18] Dickinson, M.H., Lehmann, F.-O., and Sane, S. Wing rotation and the aerodynamic basis of insect flight. *Science*, 284, 1954-1960, 1999

[19] Dickinson,M.H.and Gotz,K.G. Unsteady aerodynamics performance of model wings at low Reynolds Numbers. *J. Exp. Biol.*, 174, 56-64, 1993

[20] Drucker, E.G. and Lauder, G.V. Locomotor forces on a swimming fish: three-dimensional vortex wake dynamics quantified using digital particle image velocimetry. *J. Exp. Biol.*, 202, 2393-2412, 1999

[21] Dudley, R. and Ellington, C.P. Mechanics of forward flight in bumblebees. ii. Quasi-steady lift and power requirements. *J. Exp. Biol.*, 148, 53-88, 1990

[22] Dudley, R. The biomechanics of insect flight *Princeton University Press.*, 2000

[23] Ellington, C. P. The aerodynamics of normal hovering flight: three approaches. In Comparative Physiology - Water, Ions and Fluid Mechanics. *Cambridge University Press.*, 1978

[24] Ellington, C. P. The Aerodynamics of Hovering Insect Flight .III. Kinematics. . *Phil. Trans. R. Soc. Lond. B.* , 305(1122), 41-78, 1984

[25] Ellington, C. P. The Aerodynamics of Hovering Insect Flight .V. Vortex Theory. . *Phil. Trans. R. Soc. Lond. B.*, 305(1122), 41-78, 1984

[26] Ellington, C.P., Berg, C.V.D., Willmott, A.P. and Thomas, A.L.R. Leading-edge vortices in insect flight. *Nature* 384,626-630, 1996

[27] Ennos, A. R. The importance of torsion in the design of insect wings. *J.Exp.Biol.*, 140: 137-160, 1987

[28] Flammang, B.E., Lauder, G. V., Troolin, D.R. and Strand, T.E. Volumetric imaging of fish locomotion. *Biol. Lett.* 7, 695-698, 2011

[29] Fry, S. N., Sayaman,R. and Dickinson,M. H. The aerodynamics of hovering flight in Drosophila. *J. Exp. Biol.*, 208, 2303-2318, 2005

[30] Fry, S. N., Sayaman,R. and Dickinson,M. H. The aerodynamics of free-flight maneuvers in Drosophila. *Science*, 300(5618), 495-498., 2003

[31] Gupta,V. and Ippolito, C. Use of Discretization Approach in Autonomous Control of an Active Extrados/Intrados Camber Morphing Wing. *AIAA paper 2012-2603*, 2012

[32] Harbig, R. R., Sheridan, R. R. and Thompson M. C. Relationship between aerodynamic forces, flow structures and wing camber for rotating insect wing planforms. *J. Fluid Mech.*, 730, 52-75, 2013

[33] Hedrick,T.L., Cheng,B.and Deng, X. Wingbeat Time and the Scaling of Passive Rotational Damping in Flapping Flight. *Science*, 324(5924), 252-255. 2009

[34] Hedrick, T.L. Software techniques for two- and three- dimensional kinematic measurements of biological and biomimetic systems. *Bioinspir.Biomim.*, 3, 034001, 2008

[35] Henningsson,P. Michaelis,D., Nakata,T., Schaz,D., Geisler, R., Schroder, A., and Bomphrey,J. The complex aerodynamic footprint of desert locusts revealed by large-volume tomographic particle image velocitmetry. *J.R.Soc.Interface*, 12:20150119, 2015

[36] Hu,Z., Cheng, B. and Deng, X. Lift Generation and Flow Measurements of a Robotic Insect. *49th AIAA Aerospace Science Meeting including the New Horizons Forum and Aerospace Exposition.* 2011 Orlando , Florida

[37] Jeong,J.H. and Hussain, F. On the identification of a vortex. *J.Fluid Mech.*, 285,69-94, 1995

[38] Johansson,L.C. and Hedenstrm,A. The vortex wake of blackcaps (Sylvia atricapilla L.) measured using high-speed digital particle image velocimetry (DPIV). *J.Exp. Biol.*, 212, 3365-3376, 2009

[39] Johansson,L.C., Wolf, M., Busse, R.V., Winter, Y., Spedding, G.R. and Hedenstrm,A. The near and far wake of Pallas long tonged bat. *J.Exp.Biol.*, 211,2909-2918, 2008

[40] Johansson, L. C., Engel, S., Kelbert, A., Heerenbrink, M.K. and Hedenstrm,A. Multiple leading edge vortices of unexpected strength in freely flying hawkmoth. *Scientific Reports*, 3, 3264, 2013

[41] Kim, D. and Gharib, M. Experimental study of three-dimensional vortex structures in translating and rotating plates. *Exp. Fluids*, 49,329-339, 2010

[42] Leishman, J. G. Principles of Helicopter Aerodynamics, *Cambridge Aerospace Series*, 2006

[43] Lentink, D. and Dickinson, M.H. Rotational accelerations stabilize leading edge vortices on revolving fly wings. *J.Exp.Biol.*, 212,2705-2719, 2009

[44] Li, G.and Lu, X. Force and Power of flapping plates in a fluid *J.Fluid Mech.*, 712,598-613, 2012

[45] Liao, J.C., Beal, D.N., Lauder,G.V. and Triantafyllou, M.S. Fish exploiting vortices decrease muscle activity *Science*, 302,1566-1569, 2003

[46] Liu,H., Ellington, C.P., Kawachi,K., Den Berg, C.V.and Willmott, A.P. A computational Fluid Dynamic Study of Hawkmoth hovering. *J.Exp.Biol.*, 201, 461-477, 1998

[47] Liu, Y., Cheng, B., Barbera,G., Troolin, D.and Deng,X. Volumetric visualization of the near- and far-field wake in flapping wings. *Bioinspir.Biomim*, 8,(2013), 2013

[48] Lua,K.B., Lim,T.T and Yeo, K.S. Aerodynamic forces and flow fields of a two-dimensional hovering wing. *Exp.Fluids*, 45,1047-1065, 2008

[49] Lua,K.B., Lim,T.T and Yeo, K.S. A rotating elliptic airfoil in fluid at rest and in a parallel freestream. *Exp.Fluids*, 49,1065-1084, 2010

[50] Lua,K.B., Lim,T.T and Yeo, K.S. On the aerodynamic characteristics of hovering rigid and flexible hawkmoth-like wings. *Exp.Fluids*, 49,1263-1291, 2010

[51] Lua,K.B., Lim,T.T and Yeo, K.S. Effect of wing-wake interaction on aerodynamic force generation on a 2D flapping wing. *Exp.Fluids*, 51,177-195, 2011

[52] Ma,K.,Chirarattanon,P., Fuller, S. and Wood, R.J. Controlled Flight of a Biologically inspired, Insect - Scale Robot. *Science*, 340(6132):603-607, 2013

[53] Nabawy, M.R.A. and Crowther. W.J On the quasi-steady aerodynamics of normal hovering flight partII: model implementation and evaluation. *J. R. Soc. Interface*, 11:20131197, 2014

[54] Maxworthy, T. Experiments on Weis-Fogh mechanism of lift generation by insects in hovering flight. Part 1. Dynamics of the fling. *J. Fluid Mech.*, 93, 47-63, 1979

[55] Mittal, R., H. Dong, M. Bozkurttas, A. von Loebbecke, and. Najjar Analysis of Flying and Swimming in Nature Using an Immersed Boundary Method. *AIAA paper 2006-2867*Proceeding of 36th AIAA Fluid Dynamics Conference and Exhibit,

[56] Mountcastle, A. M. and Daniel, T.L. Aerodynamic and functional consequence of wing compliance. *Exp Fluids*, 46, 873-882, 2009

[57] Muijres, F. T., L. C. Johansson, R. Barfield, M. Wolf, G. R. Spedding and A. Hedenstrm. Leading-Edge Vortex Improves Lift in Slow-Flying Bats. *Science*, 319(5867), 1250-1253, 2008

[58] Nguyen, Q. Park,H.C., GOO,N.S. Byun,D. Aerodynamic force generation of an insect-inspired flapper actuated by a compressed unimorph actuator *Chinese Science Bulletin*54(16), 2872-2879, 2009

[59] Norberg,U.M. Aerodynamics, kinematics and energetic of horizontal flapping flight in the long eared bat. *J.Exp.Biol.*, 65,179-212, 1976

[60] Panah A.E and Buchholz J.H.J Parameter dependence of vortex interactions on a two-dimensional plunging plate. *Exp.Fluids*, 55(3) 1-19, 2014

[61] Pereira, F., Gharib, M., Dabiri, D. and Modarress, D. Defocusing digital particle image velocimetry: a 3-component 3-dimensional DPIV measurement technique. Application to bubbly flows. *Exp.Fluids*, 29(suppl 1),S78S84, 2000

[62] Pereira,F. and Gharib,M. Defocusing digital particle image velocimetry and the three-dimensional characterization of two-phase flows. *Measurement Science and Technology*, 13, 683-694, 2002

[63] Perry,M.L.,and Mueller, T.J. Leading- and Trailing- edge flaps on a low Reynolds Number Airfoil. *Journal of Aircraft*, 24 (9): 653-659, 1987

[64] Pick, S. and Lehmann,F-O. Stereoscopic PIV on multiple color-coded light sheets and its application to axial flow in flapping robotic insect wings. *Exp.Fluids*, 47, 1009-1023 , 2009

[65] Pierce, D. Photographic evidence of the formation and growth of vorticity behind plates accelerated from rest in still air. *J. Fluid Mech.*, 11, 460-464, 1961

[66] Pitt-Ford C.W. and Babinsky H. Lift and the leading edge vortex. *J. Fluid Mech.*, 720: 280-313, 2013

[67] Poelma C., Dickson W. B.and Dickinson, M. H. Time-resolved reconstruction of the full velocity field around a dynamically-scaled flapping wing. *Exp.Fluids*, 41, 213-225. 2006

[68] Pournazeri, S., Segre, P.S., Princevac, M., and Altshuler, D. L. Hummingbirds generate bilateral vortex loops during hovering: evidence from flow visualization. *Exp.Fluids*, 41, 213-225. 2012

[69] Pullin, D.I, and Wang, Z. J. Unsteady forces on an accelerating plate and application to hovering insect flight. *J. Fluid Mech.*, 509, 1-21, 2004

[70] Rayner,J.M.V. A vortex theory of animal flight. Part 1. The vortex wake of a hovering animal. *J. Fluid Mech.*, 91(4), 697-730, 1978

[71] Sane, S. P. The aerodynamics of insect flight. *J. Exp. Biol.* , 206(23), 4191-4208, 2003

[72] Sane, S. P. The Aerodynamics of Flapping wings Integrative Biology *PhD Thesis*, 2001

[73] Sane, S. P. Steady or Unsteady? Uncovering the Aerodynamic Mechanisms of Insect Flight. *J. Exp. Biol.*, 214, 349-351, 2011

[74] Sane, S. P. Self-generated airflow in flying insects I. Theoretical modeling of induced airflow. *J. Exp. Biol.* , 209, 32-42, 2006

[75] Sane, S. P. Jacobson,N.P. Self-generated airflow in flying insects II. Measurement of induced flow. *J. Exp. Biol.* , 209, 43- 56, 2006

[76] Santhanakrishnan,A., Pern,N.J. and Jacob,J.D. Optimization and Validation of a Variable Camber Airfoil. *AIAA Paper 2005-1956* 46th AIAA/ASME/ASCE/AHS/ASC Structures, 2005

[77] Smits, A.J.and Lim, T.T. Flow visualization: Techniques and Examples. *Imperial College Press* . 2000

[78] Song, J., Luo, H. and Hedrick, T. Three-dimensional flow and lift characteristics of a hovering ruby-throated hummingbird. *J. R. Soc. Interface* , 11, 20140541, 2014

[79] Spedding, G. R., M. Rosn and A. Hedenstrm. A family of vortex wakes generated by a thrush nightingale in free flight in a wind tunnel over its entire natural range of flight speeds. *J. Exp. Biol.*, 206(14), 2313-2344, 2003

[80] Srygley, R.B. and Thomas, A.L.R. Unconventional lift-generating mechanisms in free-flying butterflies. *Nature*, 206(14), 420, 660-664, 2002

[81] Su, J.-Y., Ting,S.-C., Chang,Y.-H.,and Yang, J.-T. A passerine spreads its tail to facilitate a rapid recovery of its body posture during hovering. *J. R. Soc. Interface*, 9(72), 1674-1684, 2012

[82] Sun, M. and Tang,H. Unsteady aerodynamic force generation by a model fruit fly wing in flapping motion. *J. Exp. Biol.*, 205(1), 55-70, 2002

[83] Thomas, A.L.R., Taylor, G. K., Srygley, R.B., Nudds, R. L., and Bomphrey, R. J. Dragonfly flight: free flight and tethered flow visualizations reveal a diverse array of unsteady lift-generating mechanisms, controlled primarily via angle of attack. *J. Exp. Biol.*, 207, 4299-4323, 2004

[84] Troolin D.R,and Longmire E.K. Volumetric velocity measurements of vortex rings from inclined exits. *Exp.Fluids*, 48 (3), 409-420, 2010

[85] Van den Berg, C. and Ellington, C.P. The vortex wake of a hovering model hawkmoth. *Phil. Trans. R. Soc. Lond. B.*, 352, 317-328, 1997

[86] Valasek J Morphing Aerospace Vehicles and Structures. *John Wiley and Sons*, 2012

[87] Veldhuis, C., Biesheuvel, A., Wijingaarden, L.and Lohse, D. Motion and wake structure of spherical particels. *Nonlinearity*, 18, C1, 2005

[88] Wagner H ber die Entstehung des dynamischen Auftriebes von Tragflgeln, Zeitschrift fr angewandte *Mathematik und Mechanik*, 5,17-35, 1925

[89] Walker,S.M., Thomas, A.L.R. and Taylor,G.K. Operation of the alula as an indicator of gear change in hoverflies. *J.R.Soc.Interface*, 9,1194-1207, 2012

[90] Walker,S.M., Thomas, A.L.R. and Taylor,G.K. Deformable wing kinematics in free-flying hoverflies. *J.R.Soc.Interface*, 7,131-142, 2010

[91] Wan, H., Dong, H, and Gai, K computational investigation of cicada aerodynamics in forward flight. *J.R.Soc.Interface*, 12, 2015

[92] Wang, X.X.and Wu, Z.N. Lift force reduction due to body image of vortex for a hovering flight model. *J. Fluid Mech.*, 709(4), 648-658, 2012

[93] Wang, Z.J. Dissecting Insect Flight. *Annu. Rev. Fluid Mech.*, 37. 183-210, 2005

[94] Warrick, D. R., B. W. Tobalske and D. R. Powers. Aerodynamics of the hovering hummingbird. *Nature*, 435(7045), 1094-1097, 2005

[95] Weis-Fogh,T. Quick estimates of flight fitness in hovering animals, including novel mechanisms for lift production. *J. Exp. Biol.*, 59,169-230, 1973

[96] Willmott, A. P., Ellington, C. P. and Thomas A. L. R. Flow visualization and unsteady aerodynamics in the flight of hawkmoth, Manduca sexta. *J.R.Soc.Interface*, 352, 303-316, 1997

[97] Wolf M, L. Johansson LC, Busse RV, Winter Y, Hedenstrom A Kinematics of flight and the relationship to the vortex wake of a Pallas long tongued bat. *J. Exp. Biol.*, 213,2142-2153, 2010

[98] Wu, J.C. Theory for aerodynamic force and moment in viscous flows. *J. AIAA*, 19,432-441, 1981

[99] Wu, J.Z., LU, X.Y. and Zhuang, L.X. Integral force acting on a body due to local flow structures. *J. Fluid Mech.*, 76,265-286, 2007

[100] Xia X, Mohseni K Lift Evaluation of a 2D Pitching Flat Plate. *Phys.Fluids*, 25(091901), 2013

[101] Young, J. Walker, S. M., Bomphrey, R. J., Taylor, G. K., and Thomas, A. L. R Details of Insect Wing Design and Deformation Enhance Aerodynamic Function and Flight Efficiency. *Science*, 325,1549-1552, 2009

[102] Yu X and Sun M A computational study of wing wing and wing-body interaction of a model insect. *Acta Mech. Sina*, 25, 421-31, 2009

[103] Zhang J, Childress S, Libchaber A, and Shelley M Flexible filaments in a flowing soap film as a model for one-dimensional flags in a two-dimensional wind. *Nature*, 408,835-839, 2000

[104] Zhao L, Huang Q, Deng X, and Sane S P Aerodynamics effects of flexibility in flapping wings. *J.R.Soc.Interface.*, 7,485-497, 2009

[105] Zhao, L., Sane, S. P., and Deng,X Modulation of leading edge vorticity on the aerodynamic forces in flexible flapping wings. *Bioinspir.Biomim.*, 6 (036007), 2011

[106] Zheng, L., Hedrick, T.L. and Mittal, R. A multi-fidelity modelling approach for evaluation and optimization of wing stroke aerodynamics in flapping flight. *J. Fluid Mech.*, 721, 118-154, 2013

VITA

VITA

Yun Liu obtained his Master degree and Bachelor degree respectively in 2011 and 2008 from University of Science and Technology of China in Mechanical Engineering. His previous Master research is focusing on low speed wind tunnel experiments of an oblique wing model. His PhD work at Purdue advised by Prof. Xinyan Deng focues on studying the complex flow of flapping wings. His research interests include three-dimensional flow visualization and measurement, Optical flow diagnostics, Bio-fluid mechanics and Renewable energy.